UNIVERSITY OF SOUTHAMPTON

POWER FLOW ANALYSIS OF ENGINEERING STRUCTURES USING SUBSTRUCTURE TECHNIQUES

By

Zhenhong WANG

Thesis submitted for

the degree of Ph. D.

School of Engineering Sciences, Ship Science

FACULTY OF ENGINEERING AND APPLIED SCIENCE

October 2002

UNIVERSITY OF SOUTHAMPTON

ABSTRACT

FACULTY OF ENGINEERING AND APPLIED SCIENCE
SCHOOL OF ENGINEERING SCIENCES, SHIP SCIENCE

Doctor of Philosophy

POWER FLOW ANALYSIS OF ENGINEERING STRUCTURES USING SUBSTRUCTURE TECHNIQUES

By Zhenhong WANG

This thesis discusses and develops the theory of power flow analysis to assess the dynamic characteristics of engineering structures adopting a substructure approach.

The general substructure receptance approach is extended and used to investigate the power flow characteristics applicable to engineering structures. This is achieved by complementing the normal dynamic equations with geometrical compatibility conditions allowing the assessment of dynamic characteristics of power flow excited and transmitted within the system. Each substructure is modelled analytically or numerically and its receptance function is formulated by modal analysis. The method may be classified as a form of substructuring analysis using a free-free interface condition. The displacement components induced by external forces and the interface coupling forces are deduced, permitting determination of the coupling forces and power flow between the interface of substructures. A power flow density vector is defined. The numerical examples demonstrate the applicability of the method and the detailed configurations display the power flow characteristics associated with beam frames, L-shaped plates, corner plates, beam-stiffened plates and coupled plate-cylindrical shell systems.

KEY WORDS: power flow, substructure approach, beam, plate, modal synthesis, receptance function.

LIST OF CONTENTS

LIST OF FIGURES

ACKNOWLEDGEMENTS

Firstly I wish to express my sincere gratitude to my supervisors, Professor W.G. Price and Professor Jing Tang Xing for their academic supervision, support and kind encouragement in accomplishing every aspect of this work over the last three years.

Secondly I would like to express my sincere gratitude to my colleagues in the China Ship Scientific Research Centre, for their help, support and kind encouragement.

I also thank Dr. Weibo Wang, Dr. Yeping Xiong and Dr. Shuangxing Du for discussions of some questions of mechanics, Dr. Mingyi Tan and Professor P. A. Wilson for helping in solving computer problems, as well as all of the members of the School of Engineering Sciences, Ship Science, for helping me over the years.

Last, but not least, I wish to thank my parents, my wife and my son for their never ending support in my life.

NOTATIONS

a	the length of a rectangular plate
A	section area of beam
b	the width of a rectangular plate
B	a continuum system
B_1,B_2,B_3,B_4	coefficients in modal shape function
C	the connected joint of beam frame
C_{ijkl}	the elastic properties of solid
C_L	the longitudinal wave speed
C_T	the transverse (in-plane) shear wave speed
D	flexural rigidity of plate or shell
$\dot{D}$	the rate of change of energy dissipation
E	Young's modulus
$\dot{E}$	rate of change of mechanical energy (chapter 2)
$\tilde{e}_{ij}$	general expression of strain tensor
E_{ij}	amplitude of $\tilde{e}_{ij}$
$\tilde{f}(t)$	general expression of force
$\tilde{f}_i(x_e, y_e, t)$	force at position (x_e, y_e) along direction i
F	amplitude of $\tilde{f}(t)$
G	shear modulus
h, h_p	the thickness of a plate
h_s	the thickness of a shell
i	$=\sqrt{-1}$
I	moment of inertia
J	polar second moment
l	the length of a beam
L	the length of a cylindrical shell
k	wave number
$\dot{K}$	the rate of change of kinetic energy
$[K]$	structure stiffness matrix

m, n	the mode number used in modal analysis
$\tilde{M}$	general expression of bending moment and twist moment
$\tilde{M}_{xx}, \tilde{M}_{yy}, \tilde{M}_{\theta}$	bending moment per unit length
$\tilde{M}_{xy}, \tilde{M}_{x\theta}$	twisting moment per unit length
$[M]$	structure mass matrix
m_r, m_{rs}	generalized modal mass
$\tilde{N}$	general expression of axial or in-plane force
$\tilde{N}_{xx}, \tilde{N}_{yy}, \tilde{N}_{\theta}$	extension force per unit length
$\tilde{N}_{xy}, \tilde{N}_{x\theta}$	in-plane shear force per unit length
$\tilde{p}_r(t)$, $P_{rs}(t)$	principal co-ordinate
q	general expression for power flow
$\langle q \rangle$	general expression for time averaged power flow
q^{υ}	the power flow across the interface with the normal υ_i
$\hat{q}_f$	the rate of energy input
$\tilde{Q}$	general expression for shear force
$\tilde{Q}_x, \tilde{Q}_y, \tilde{Q}_{\theta}$	transverse shearing forces per unit length
R	radius of cylindrical shell
R_e	interface receptance function under external excitations
R_s	interface receptance function under internal coupling forces
$s^{(IJ)}$	interface between substructures I and J
S	the surface of a domain
T	period of excitation
T_i	internal traction force in i direction
$[tr]$	the orthogonal co-ordinate transformation matrix between global and local co-ordinate systems
$\tilde{u}(t)$	general expression for displacement

$\dot{\tilde{u}}(t)$	general expression for velocity
$\dot{U}$	the rate of change of potential energy
U_x, U_y, U_z	the amplitude of displacement at x, y and z direction respectively
$\tilde{v}(t)$	general expression for velocity
$x,y,z\ or\ \theta$	spatial co-ordinates
x_1, x_2, x_3	spatial co-ordinates for a continuum
x_e, y_e	excitation position
α	the angle between global and local coordinate systems
β_r, γ_r	plate solution parameter (defined in chapter 5)
$\delta(x)$	*Dirac* delta function
η	damping loss factor
λ_r	$=\omega_r a^2\sqrt{\rho / D}$, eigenvalue of plate
φ	general expression for phase angle
φ_r	principal mode shape of beam/rod
φ_{rs}	principal mode shape of plate or shell
ϕ	plate aspect ratio
μ	Poisson's ratio
$\tilde{\theta}$	general expression for slope angle
$\dot{\tilde{\theta}}$	general expression of angular velocity
θ_b	angle at the coupling edges in the cylindrical co-ordinate system
ρ	mass density
σ_{ij}	stress tensor
υ_j	unit normal
ω	exciting frequency
ω_r	the *r*th natural frequency
Ω	the domain of a continuum
$[\ ]$	a matrix
$[\ ]^T$	transpose of a matrix
$[\ ]^{-1}$	inverse of a matrix

$(\dot{\ })$	time derivative
$\left(\tilde{\ }\right)$	a complex quantity
$\left(\hat{\ }\right)$	a prescribed quantity

Subscript

i, j, k, l	tensor subscript, can independently be 1, 2 or 3 in a three-dimensional case (chapter 2,3)
$M \times N$	rows×columns of a matrix in chapter 3
r, s	the rth or sth principal mode shape
x, y, z *or* θ	the variables in x, y, z direction or in rotation direction in a cylindrical co-ordinate system

Superscripts

$*$	complex conjugate
I, J	subsystem number

1. INTRODUCTION

1.1. Brief Review

The dynamic behaviour of engineering structures is a very important aspect of assessing the whole performance of a structural system, but analysis of dynamic characteristics is a difficult task. If the structure system to be analysed is simple and idealised (e.g., uniform beams and rectangular plates with special boundary conditions), classical techniques may be used to give exact results. Unfortunately for most real engineering structures, the application of classical theory is never simple or wholly satisfying. Most engineering problems could not be fully solved until the science of computers and the techniques of finite element analysis (FEA) were well developed. Finite element analysis (see, for example, Zienkiewicz 1971) is a powerful numerical method to provide detailed modal characteristics of complex structures.

FEA may be divided into two categories. One approach involves directly solving the system's dynamic equations to derive modal parameters. Another approach to determine natural frequencies and mode shapes associated with a structural analysis is to adopt a component modal synthesis technique or alternatively called a substructure approach. This approach utilises eigensolutions of each substructure, together with geometric compatibility conditions and force equilibrium equations on interfaces of substructures to synthesise the dynamic characteristics of the global structure (see Hurty 1965, Hou 1969, Craig & Change 1976 and Hale & Meirovitch 1982). However, classical vibration theories tell us that all structures, even the simplest structure, have an infinite variety of natural modes, with corresponding natural frequencies covering the entire frequency range. This leads to the conclusion that FEA, a discretization procedure, is best suited to the low frequency range.

For most complex engineering structures, the results derived by prediction of frequency response based on modal analysis using FEA become more and more unreliable and tedious as the frequencies increase. The fundamental reason is that the sensitivity of modal resonance frequencies and relative modal phase response to small changes in structural details, especially boundary conditions, increases with mode order.

The distribution of higher order modes begin to overlap (Manohar & Keane 1994), indicating that there is increasing uncertainty in the results derived by a frequency response analysis.

There is also unavoidable uncertainty concerning structural detail and material properties associated with manufacturing tolerances and fabrication imperfections. This is especially true for the high frequency dynamic properties of joints between components. As a result, high frequency vibration responses of individual examples of nominally identical structures are observed to differ, some times greatly (Komella & Bernhard, 1993).

The theoretical basis of Statistical Energy Analysis (SEA) or Power Flow Analysis (PFA) has developed because of such deficiencies incorporated into finite element methods to analyse accurately the structural dynamic responses of a system excited at high frequencies. SEA, which is based on the concept of an ensemble-averaged behaviour together with statistical measures of the distribution of responses about this average, is a possible approach to generate an estimation of frequency response in the higher frequency range. The development of SEA arose from a need by aeronautical and aerospace engineers in the early 1960s to predict the vibrational response of flight vehicles. It has also been applied to predict structure borne noise in ship structures (Cabos 1999) and buildings (Gibbs & Gilford 1976 and Luzzato & Ortola 1988).

Fahy (1994) presents a comprehensive critical review of SEA theory highlighting its origin, development and future possible directions and applications. One of the earliest applications of SEA to describe and analyse simple vibrating systems was presented by Lyon & Maidanik (1962) who formulated a mathematical method based on modal theory. Lyon (1975) further developed their ideas with applications to more complex vibrating systems. Langley (1992) described a wave theory approach and a predictive approach was proposed by Heron (1999) based on the wave approach. Manning (1994) developed the concept of a mobility model which was incorporated into a statistical energy analysis. Keane & Price (1997) and Fahy & Price (1999) present recent developments and advances in SEA theory and its mathematical modelling with applications to complex, coupled vibrating systems.

The application of SEA to a vibrating system aims to determine the spatial, time and frequency statistical averages of energy flowing through each subsystem within the overall dynamic performance using the quantities known as coupling loss factors (Lyon 1975). Therefore a SEA approach provides only the space averaged information of the field variables with the loss of detailed knowledge of the local distribution of the variables. Because coupling loss factors are usually determined under the assumption of semi-infinite structural domain theory (see, for example, Langley 1990 and Cremer *et al* 1988), SEA is suitable for application in the high frequency range. In contrast, the power flow approach is not necessarily restricted to the high frequency range and the parameters of power flow and mobility may be expressed as a modal function aggregate to retain the resonant behaviour of the individual and global structures at low modal density. If it is assumed that all phase effects may be neglected at high modal density, which implies that various mode components may be considered to be uncorrelated, the mobilities can be expressed in a similar form to those obtained by SEA (Langley 1990, Manning 1994).

1.2. Background of Engineering Application to a Power Flow Analysis

Power flow analysis is usually applied in three aspects: in calculation and control in engine isolation system, in calculation and comparison of energy transmission factors or coupling loss factors used in SEA as well as determination of the dominant propagating paths of vibration energy and structure borne noise.

1.2.1. Application to Engine Isolation Systems

The general interest focused on dynamic structural analyses demonstrates the necessity for vibration control, the common objective being to minimise vibration levels. For engine isolation systems, the amount of power flowing from the machine is dependent on the characteristics of the source, the isolator system and the support structure. The use of power flow in problems of this type is very valuable because it combines both forces and velocities as a single concept. An attempt to decrease their radiation or vibration in a structure by reducing only the force or velocity amplitude and not considering the relative phase angle relation may not necessarily be successful. However, improvements may result by decreasing the power flow applied to a structure (see, for example, Goyder & White 1980). Many other researches, for example, Pinnington & White (1981), Pinnington (1987), Pan *et al* (1992), Gardonio *et al* (1997a,b), Li & Lavrich (1999), Xiong *et al* (2000), also focus their studies on application and control of power flow to engine isolation systems.

1.2.2. Application to Calculate Coupling Loss Factors of SEA

Statistical energy analysis is a feasible way to solve averaged energy flow problems in the high frequency domain. The basis of this technique lies in the fact that the energy flow within a system can be related to the difference in vibrational energy between parts of the system. This allows simple formulation of dynamic quantities, i.e. coupling loss factors (Lyon 1975), to describe the energy flow of the dynamic system based on linear differential equations. However, a strict experimental determination of these factors can be difficult, because they relate to systems of infinite size according to their definitions. Therefore, alternative approaches for use in the low to middle frequency domain are of interest to solve energy flow problems and to estimate coupling loss factors for simple applications of SEA. Simmons (1991), Steel & Craik (1993), Fredo (1997) and Shankar & Keane (1997) developed FEA models to calculate the energy flow around systems and to estimate the coupling loss factors or energy flow factors between substructures. This improves SEA predictions in the low to middle frequency range.

1.2.3. Application to Determine Power Flow Paths

The identification of power flow paths in dynamically loaded structures is also important. Structure-borne sound is the vibrational energy which travels through dynamically loaded mechanical systems. This vibrational energy is radiated eventually into an acoustic medium as noise. An example cited by Wohlever & Bernhard (1988) is an aeroplane wing loaded by engine vibrations. The vibrational energy travels along the wing to the fuselage and is radiated as sound into the cabin. Luzzato & Ortola (1988) addressed the problem of structure-borne sound in hotels and apartment buildings, where vibrational energy flows through walls and floors and is radiated as sound into other rooms. The calculation of a power flow density vector is a way of quantifying the propagation of vibration energy and structure-borne sound. This method identifies the magnitude and direction of power at any location in a structure and helps analysts to find the dominant paths of energy flow, the energy sinks and the propagation of structure-borne sound in a given problem. Understanding the paths of energy which flow from a vibration source to other parts of the structure helps an engineer pinpoint and control vibration problems. Examples may be cited for a wide range of applications, such as damping materials inserted into dominant paths of energy flows and mechanical equipment arranged near the energy sinks for a passive vibration control measure.

1.3. Development and Current State of Power Flow Analysis

The fundamental concepts of power flow analysis, as discussed and described by Goyder & White (1980), use the rate of energy flow to characterise the dynamic response of vibrating systems. This was found to be a more meaningful parameter in assessing the dynamic properties of isolator-engine systems as confirmed by Pinnington & White (1981).

1.3.1. Theoretical Model of Power Flow Analysis

Several PFA approaches have been presented which combine the analytical solution of individual structural elements in finite sized structures. These include:

<u>The mobility approach</u>

The global structure in a mobility approach is modelled by a set of coupled substructures with forces or moments introduced at the joints (or line) between the substructures. The power flow into a source substructure and between the substructures is expressed in terms of input and transfer structural mobility functions. Structural mobility is defined as the ratio of the rate of change of displacement with time per unit input load. For input mobilities the response and load are considered at the same location, whereas for transfer mobilities the response and load are defined at separate locations. It is a kind of progressive approach and can be conveniently applied at a joint as discussed by Pinnington & White (1981) and Cuschieri (1990a). Cuschieri (1990b) also applied the approach to solve the dynamics of L-shaped plates.

Xiong, Xing & Price (2001) developed two progressive approaches to analyse the power flow into and transmission between substructures in a complex coupled system consisting of any number of subsystems. Generalised mobility/impedance matrix formulations of each substructure are first derived allowing the construction of equivalent mobility and equivalent impedance matrices to describe the dynamic behaviour of a substructure assembled from several inter-connected substructures within the overall system.

The direct dynamic stiffness method

The direct dynamic stiffness method presented by Langley (1989) focuses on the study of the transverse response of a row of coupled plates subject to an acoustic pressure field. The solution is restricted to the case when two opposing edges are simply supported so that the two coupled variables in the dynamic equation of each uncoupled plate can be reduced independently. The dynamic stiffness matrix of each uncoupled plate can then be derived analytically and using standard techniques, the dynamic stiffness matrix for the whole system produced. The degrees of freedom in this method are the deflections at the joints. This approach was also used by Bercin & Langley (1996) to calculate the in-plane vibrations of similar plate frames.

The travelling wave and scattering approach

In this approach, exact wave mode expressions are used to represent the solution of each substructure, then continuity and equilibrium of substructure displacements and forces and satisfaction of displacement boundary conditions at the junction are used to calculate the junction scattering and generation matrices. This approach was applied to two and three-dimensional beam frames by Miller & Flotow (1989), Horner & White (1991), Beale & Accorsi (1995).

The receptance approach

This approach is similar to the dynamic stiffness method in that it also finds the solution in terms of the characteristics of uncoupled substructures. However, the degrees of freedom in this approach are the coupling forces at the interface rather than the displacements used in the dynamic stiffness method. These unknown coupling forces are calculated by utilising the compatibility conditions at the interface. The receptance approach was applied in an indeterminate beam system by Wang, Xing & Price (2002a), and in two coupled rectangular plates by Dimitriadis & Pierce (1988), Farag & Pan (1998), Beshara & Keane (1998) and Wang, Xing & Price (2002b).

The general objective of these analytical exact approaches is to assess the averaged power flow across the coupling edges and joints of the subsystems. Beshara & Keane (1997, 1998) determined the power flow at a compliant and dissipative joint and edge using a receptance approach. Investigations using a power flow analysis mainly focus on coupled beams or plate-like structures because solutions adopted in these exact approaches are restricted to cases in which the dynamic distortions of subsystems can be determined theoretically. For example, substructures consisting of uniform beams with any standard boundary conditions or uniform rectangular plates with two opposing edges simply supported.

1.3.2. Power Flow Analysis by FEA Model

Applications of FEA to energy flow modelling are not new. Lyon (1975) suggested the use of FEA to predict SEA coupling loss factors during the early development of SEA theory. A power flow finite element method was proposed by Nefske & Sung (1987) and investigated by Wohlever & Bernhard (1992). They postulated that if the mechanical energy of a vibrating structure is governed by a heat conduction equation, then this should simplify the computational requirements for a power flow analysis in the mid-frequency range. For a simple beam, Nefske & Sung compared the results derived by a conventional structural FEA and SEA with FE predictions based on a heat conduction analogy approach and an exact solution for the system. For the same number of elements, the heat conduction FE approach yields better results at higher frequencies than the conventional FEA and gives better spatial resolution than SEA. Wohlever & Bernhard (1992) showed that the heat conduction analogy for mechanical energy is only approximately true for rods and beams.

Various studies investigating vibrational energy by FEA models are described by Simmons (1991), Stimpson & Lalor (1992), Steel & Craik (1993), Fredo (1997) and Mace & Shorter (2000). These authors expressed the response of a finite element model in terms of an energy flow through a global FEA performed on a global system. The natural frequencies and mode shapes are calculated first and velocity at the nodes determined by modal analysis. The use of a lumped mass formulation is implicitly assumed and the kinetic energy is evaluated adopting a single summation involving the nodal mass and nodal velocity of responding nodes.

Shankar & Keane (1995,1997) developed an alternative local FEA method using a receptance approach in which the response of each subsystem is described by a Green function to analyse energy flow for both simple and complex models. It is the same as the receptance approach discussed in 1.3.1 but the receptance function of substructures is obtained by FEA.

Finite element analysis has also been used to calculate structural intensity. For example, the structural intensities of a rectangular stiffened plate and a uniform rectangular plate are analysed by Hambric (1990) and Gavric & Pavic (1993) respectively. It is advantageous to use FEA models in a power flow analysis and in structural intensity calculations because they can be conveniently applied to complex structures subject to boundary conditions. However, in general, because the structure intensity prediction requires an accurate description of various spatial derivatives, it is necessary to admit a large number of modes into the analysis to ensure convergence of solution. Numerical approaches adopting modal superposition encounter difficulties due to the computational effort required. Furthermore, since the intensity is sensitive to the relative phases of these modes, predictions are potentially very sensitive to the accuracy of the data used to describe the system and to FEA discretization error.

1.3.3. Definition of Power Flow Density Vector in a Continuum

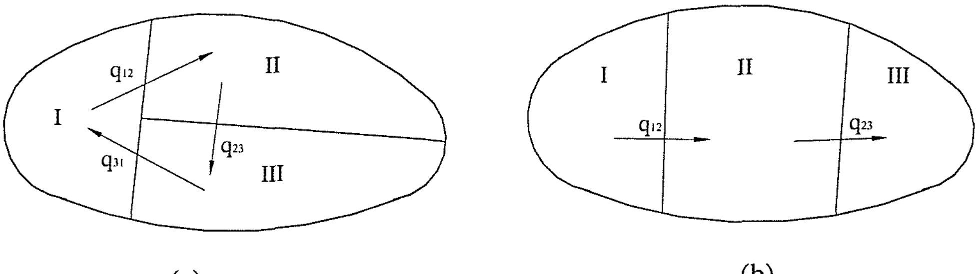

(a) (b)

Figure 1.1 Schematic illustration of a system with three subsystems I, II, III. The arrows indicate energy flow from one subsystem to another. In the indeterminate system of (a), a delta energy flow pattern occurs and three energy flow quantities are required to analyse the energy flow in the system. In contrast, the sequential energy flow pattern observed in (b) requires only two energy flows to analyse the system.

Xing & Price (1999) developed the concept of an energy flow density vector which uniquely defines the energy transmission between one part of a system and another. The analysis of structural intensity or energy flow density vector identifies the magnitude and direction of the power at any location in a structure and allows determination of dominant paths of energy flow. To understand the mechanisms and paths of energy transmission flowing from a vibration source to other parts of a structure has been recognised as an important tool for control vibration (Pan & Hansen, 1991).

To study the energy flow in a vibrating system or continuum adopting either a statistical energy analysis or a power flow analysis it is necessary to divide the continuum domain or system into a number of subsystems. For illustrative purposes, figure 1.1 schematically shows a continuum divided into three sub-domains (I, II, III), but with different configurations. For figure 1.1a, Xing & Price (1999) showed that three energy flows q_{ij}, forming a *delta flow pattern*, are required in a PFA, whereas only two energy flows, forming a *sequential flow pattern*, are required to analyse the subsystem configuration in figure 1.1b. They also demonstrated that because the number of independent energy flow equations for three sub-domains is two, the delta flow pattern cannot be determined solely from an energy flow balance analysis. In fact, the energy flow lines in figure 1.1a form a closed curve, i.e., a conceptual delta shape, so that any quantity of energy flow added will not affect the energy flow balance, further confirming that the subdivided system of figure 1.1a cannot be determined only by examination of the equation of energy flow balance. To overcome such deficiencies, Wang, Xing & Price (2002b) proposed a substructure method to analyse the power flows in L-shaped plates.

Most power flow analyses adopt a substructure approach because

(1) Long computer runs are avoided for large, complex structures.

(2) It is more efficient to confirm a large quantity of input data via subsets.

(3) The input data for each substructure can be prepared almost independently by separate analysts.

(4) Numerous restart points are automatically provided.

(5) For some special components of structures, for example, a wing of an aeroplane, experiments can also be adopted to determine the dynamic and damping characteristics of these components.

The different theoretical models of power flow analysis presented in 1.3.1 are all based on substructure approaches but use different analytical models to describe the dynamic characteristics of each substructure.

Besides the advantages of adopting a general substructure approach, this technique has the ability to calculate directly substructure energy transmissions, since it deals with both interface forces and displacements at interfaces. It also allows inclusion of substructure specific damping.

1.4. Objectives of the Research

The objective of this thesis is to investigate the power flow characteristics of engineering structures. A general substructure receptance approach for a continuum with free-free interface condition is formulated by complementing the normal dynamic equations with geometrical compatibility equations allowing assessment of power flow dynamic characteristics applied to and excited within the system. Each substructure is modelled analytically or numerically and its receptance function is formulated by modal analysis. The displacement components induced by the external and the interface coupling forces are deduced, permitting determination of the coupling forces and power flow between the interface of substructures. A power flow density vector is defined. Engineering numerical examples demonstrate the applicability of the method and their detailed configurations display the power flow characteristics associated with indeterminate beam systems, L-shaped plates, corner plates, beam-stiffened plates and coupled plate-cylindrical shell systems.

The main advantage of using a theoretical model in a power flow analysis allows calculation of high-frequency components easily and efficiently, so it is suitable to calculate the detailed distribution of the power flow density vector in a structure. Convergence problems do not arise because dynamic displacements and internal forces have formulated expressions in the proposed theoretical models. The limitation of all theoretical models, including mobility approach, dynamic approach and wave-guide approach is obvious, because the displacements or internal forces of each substructure need to be solved analytically. Therefore, theoretical models can only be applied to relatively simple structures, for example, a beam frame or a uniform plate system with two opposite edges simply supported. The substructure approach presented herein uses substructure results analysed by analytical methods, numerical approaches, measurement results or their combinations. When a substructure is readily defined by an analytical solution, a theoretical substructural model is adopted, otherwise, a FEA model is adopted to analyse more complex systems. It is also much easier to derive FEA results for a substructure than those for a global model although there may exist difficulties in deriving convergent solutions at high modal density.

1.5. Outline of Thesis

In Chapter 2, the fundamentals of power flow are described. Three approaches of power flow analysis, that is, mobility approach, direct dynamic stiffness approach and travelling scattering wave approaches are presented briefly. The concept of an energy flow density vector is introduced and equations of energy flow balance are derived to describe the basic characteristics of energy flow in a continuum.

In Chapter 3, a general substructure approach with free-free interface condition applied to a continuum is presented. The force balance and geometric compatibility conditions of an interface are introduced to form the synthesis process.

In Chapter 4, a power flow analysis applied to an indeterminate rod/beam system is presented. Two calculation examples show the power flow characteristics of beam systems.

In Chapter 5, a power flow analysis applied to coupled plate systems is presented. The power flow characteristics in L-shaped plates and in corner plates are calculated and discussed. Power flow lines are illustrated within the plate system and they show how the power flows at any instant and in a period of excitation.

In Chapter 6, the power flow characteristics of a beam-stiffened plate are calculated and discussed.

In Chapter 7, a power flow analysis applied to a coupled plate-cylindrical shell system is presented. The power flow characteristics of the system are calculated and discussed for both conservative and dissipative couplings. Power flow lines are adopted to illustrate how the power flows in the plate and shell.

Chapter 8 summaries the main conclusions and achievements of the research study. Further work and possible engineering applications of a power flow analysis are also discussed.

2. REVIEW OF ANALYTICAL POWER FLOW APPROACHES

The general power flow approaches presented herein adopt substructure techniques because it is impossible to determine the response of a complex structure analytically other than by a FEA or a numerical method. Therefore, force balance conditions and geometrical compatibility equations supplement the various power flow approaches. The main difference between these approaches is the analysis methods of the responses of substructures. These power flow approaches reviewed here are the mobility progressive approach, wave scattering approach and dynamic stiffness method. A general receptance approach is presented in chapter 3.

2.1. Basic Concept of Power Flow Analysis

The fundamental concepts of power flow analysis, as discussed and described by Goyder & White (1980a,b,c), use the rate of energy flow to characterise the dynamic response of vibrating systems. The use of power flow is valuable in vibration control because it combines both forces and velocities together. An attempt to decrease the radiation or vibration in a structure by reducing only the force or velocity amplitude and not considering their relative phase angle may not necessarily be successful. However, an improvement may be ensured by decreasing the net vibrational power (time averaged power) applied to a structure.

The basic definition of power is the rate at which work is done and given by

$$q(t) = f(t)v(t) \tag{2.1}$$

where $f(t)$ and $v(t)$ are the instantaneous values of physical force and velocity at a point.

In a dynamic analysis, harmonic quantities are often represented mathematically by harmonic functions. In complex mathematical forms, a harmonic force $\tilde{f}(t)$ with amplitude F and frequency ω, or a velocity $\tilde{v}(t)$ with amplitude V, frequency ω and relative phase angle φ, can be expressed as

$$\tilde{f}(t) = Fe^{i\omega t}, \tag{2.2}$$

$$\tilde{v}(t) = Ve^{\mathrm{i}(\omega t+\varphi)} = \tilde{V}e^{\mathrm{i}\omega t}, \tag{2.3}$$

where $\mathrm{i} = \sqrt{-1}$ and, in general, $\tilde{V} = Ve^{\mathrm{i}\varphi}$ and $\tilde{F} = F$ are treated as complex quantities.

In a PFA, the real power at time t is given by

$$\begin{aligned} q(t) &= \mathrm{Re}\{\tilde{f}(t)\}\mathrm{Re}\{\tilde{v}(t)\} = \frac{1}{4}\left(\tilde{f} + \tilde{f}^*\right)\left(\tilde{v} + \tilde{v}^*\right) \\ &= \frac{1}{2}\mathrm{Re}\left\{\tilde{f}\,\tilde{v} + \tilde{f}^*\,\tilde{v}^*\right\}. \end{aligned} \tag{2.4}$$

The time averaged of this real power over a period of vibration $2\pi/\omega$, i.e. the mean power, is given by

$$\begin{aligned} \langle q(t)\rangle &= \frac{\omega}{2\pi}\int_0^{2\pi/\omega}\mathrm{Re}\{\tilde{f}\}\mathrm{Re}\{\tilde{v}\}dt = \frac{1}{2}|\tilde{F}||\tilde{v}|\cos\varphi \\ &= \frac{1}{2}\mathrm{Re}\{\tilde{F}\tilde{V}^*\} = \frac{1}{2}\mathrm{Re}\{\tilde{F}^*\tilde{V}\} = \frac{1}{2}\left(\mathrm{Re}\{\tilde{F}\}\mathrm{Re}\{\tilde{V}\} + \mathrm{Im}\{\tilde{F}\}\mathrm{Im}\{\tilde{V}\}\right). \end{aligned} \tag{2.5}$$

Mathematically, an instantaneous complex power may be defined as

$$\tilde{q}(t) = \tilde{f}(t)\tilde{v}(t) = \tilde{F}\tilde{V}e^{\mathrm{i}\omega t}, \tag{2.6}$$

with corresponding time averaged quantity

$$\langle\tilde{q}(t)\rangle = 0. \tag{2.7}$$

This result clearly conveys the essential difference between a physical power and a complex power. Therefore, real power is the primary quantity considered.

Goyder & White (1980a,b,c) analysed a number of typical foundations constructed from beams, plates and beam-stiffened plates using a wave propagation approach. Each structural component was treated as if it was infinite in dimension.

2.2. Mobility Approach

The basic concepts of a mobility approach (see, for example, Cuschieri 1990b and Xiong, Xing & Price 2001) to determine the transmitted vibrational power between a point-coupled substructure. The mobility function is defined as

$$Y^{jk} = \frac{v_j}{f_k}, \tag{2.8}$$

and defines the velocity response at position *j* under a unit exciting force at position *k*. If *j=k*, Y^{jj} is called a point mobility and if $j \neq k$, Y^{jk} denotes the transfer mobility between position *j* and *k*.

Figure 2.1 illustrates schematically a coupled system with *n* series connected subsystems S_k ($k=1,2,\ldots,n$), where each substructure represents either a rigid or flexible component of the global system. A representative substructure S_k may have r_k inputs and r_{k+1} outputs within the global system.

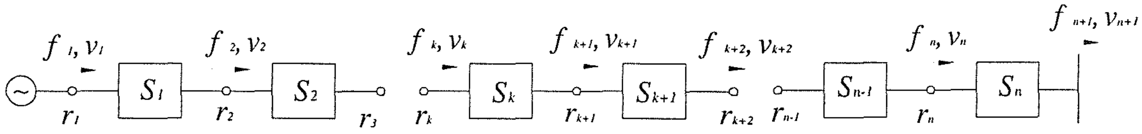

Figure 2.1. Schematic illustration of general mobility model with *n* substructures.

While boundary conditions $f_1 = \hat{f}_1$, $v_{n+1} = \hat{v}_{n+1}$ are prescribed, the progressive approach allows determination of internal forces and response velocities on interfaces between the substructures. The dynamic equations (see, for example, Xiong, Xing & Price 2001) describing the dynamical characteristics of all substructures S_k ($k=1,2,\ldots,n$) can be represented by the generalised mobility matrix expressions

$$\begin{Bmatrix} v_1 \\ v_2 \end{Bmatrix} = \begin{bmatrix} Y_{(1)}^{11} & Y_{(1)}^{12} \\ Y_{(1)}^{21} & Y_{(1)}^{22} \end{bmatrix} \begin{Bmatrix} f_1 \\ f_2 \end{Bmatrix}, \tag{2.9}$$

$$\begin{Bmatrix} v_{k-1} \\ v_k \end{Bmatrix} = \begin{bmatrix} Y_{(k-1)}^{11} & Y_{(k-1)}^{12} \\ Y_{(k-1)}^{21} & Y_{(k-1)}^{22} \end{bmatrix} \begin{Bmatrix} f_{k-1} \\ f_k \end{Bmatrix}, \tag{2.10}$$

$$\begin{Bmatrix} v_k \\ v_{k+1} \end{Bmatrix} = \begin{bmatrix} Y_{(k)}^{11} & Y_{(k)}^{12} \\ Y_{(k)}^{21} & Y_{(k)}^{22} \end{bmatrix} \begin{Bmatrix} f_k \\ f_{k+1} \end{Bmatrix}, \tag{2.11}$$

$$\begin{Bmatrix} v_n \\ v_{n+1} \end{Bmatrix} = \begin{bmatrix} Y_{(n)}^{11} & Y_{(n)}^{12} \\ Y_{(n)}^{21} & Y_{(n)}^{22} \end{bmatrix} \begin{Bmatrix} f_n \\ f_{n+1} \end{Bmatrix}. \tag{2.12}$$

Equation (2.11) is for substructure S_k $(k=1,2,\ldots,n)$. It follows that

$$f_{k+1} = \left[Y_{(k)}^{22}\right]^{-1} v_{k+1} - \left[Y_{(k)}^{22}\right]^{-1} Y_{(k)}^{21} f_k, \tag{2.13}$$

$$\begin{aligned} v_k &= \left\{Y_{(k)}^{11} - Y_{(k)}^{12}\left[Y_{(k)}^{22}\right]^{-1} Y_{(k)}^{21}\right\} f_k + Y_{(k)}^{12}\left[Y_{(k)}^{22}\right]^{-1} v_{k+1}, \\ &= Y_{ke} f_k + Y_{kv} v_{k+1} \end{aligned} \tag{2.14}$$

where $$Y_{ke} = \left\{Y_{(k)}^{11} - Y_{(k)}^{12}\left[Y_{(k)}^{22}\right]^{-1} Y_{(k)}^{21}\right\}, \quad Y_{kv} = Y_{(k)}^{12}\left[Y_{(k)}^{22}\right]^{-1}. \tag{2.15}$$

Substituting equation (2.14) into equation (2.10) for substructure S_{k-1} we derive the following equations describing the coupling characteristics of two adjacent substructures S_k and S_{k-1}:

$$f_k = \left[Y_{(k-1)}^{22} - Y_{ke}\right]^{-1} \cdot \left[Y_{kv} v_{k+1} - Y_{(k-1)}^{21} f_{k-1}\right], \tag{2.16}$$

$$\begin{aligned} v_{k-1} &= \left\{Y_{(k-1)}^{11} - Y_{(k-1)}^{12}\left[Y_{(k-1)}^{22} - Y_{ke}\right]^{-1} Y_{(k-1)}^{21}\right\} f_{k-1} + Y_{(k-1)}^{12}\left[Y_{(k-1)}^{22} - Y_{ke}\right]^{-1} Y_{kv} v_{k+1}, \\ &= Y_{(k-1)e} \cdot f_{k-1} + Y_{(k-1)v} \cdot Y_{kv} v_{k+1} \end{aligned} \tag{2.17}$$

where $$Y_{(k-1)e} = \left\{Y_{(k-1)}^{11} - Y_{(k-1)}^{12}\left[Y_{(k-1)}^{22} - Y_{ke}\right]^{-1} Y_{(k-1)}^{21}\right\}, \tag{2.18}$$

$$Y_{(k-1)v} = Y_{(k-1)}^{12}\left[Y_{(k-1)}^{22} - Y_{ke}\right]^{-1}. \tag{2.19}$$

The continuation of this procedure leads to the following progressive formulation characterising a coupled global system consisting of substructures $S_1, S_2,\ldots,S_k,\ldots,S_n$. Namely,

$$v_k = Y_{ke} f_k + N_{kv} \hat{v}_{n+1}, \tag{2.20}$$

$$f_{k+1} = \left[Y_{(k+1)e} - Y_{(k)}^{22}\right]^{-1} Y_{(k)}^{21} f_k + \left[Y_{(k)}^{22} - Y_{(k+1)e}\right]^{-1} N_{(k+1)v} \hat{v}_{n+1}, \tag{2.21}$$

for $k=1,2,\ldots,n$,

where $$N_{kv} = Y_{kv} \cdot Y_{(k+1)v} \cdots Y_{nv}, \tag{2.22}$$

$$Y_{(n+1)e} = 0. \tag{2.23}$$

According to the basic definition of time averaged power flow in equation (2.5), the power flow through of the *k*th substructure is given by

$$\langle q(t)\rangle = \frac{1}{2}\mathrm{Re}\left\{f_k^* v_k\right\} = \frac{1}{2}\mathrm{Re}\left\{f_k\, v_k^*\right\},\quad k=1,2,\ldots n. \tag{2.24}$$

This mobility progressive approach is applied conveniently in series connected systems, for example, a coupled isolator-engine system after all mobility functions of each substructure are defined. However, it cannot be applied to a more complex system, for example, a system represented a delta energy flow pattern as shown in figure 1.1a.

2.3. Dynamic Stiffness Approach

Langley (1989) presented the dynamic stiffness method to investigate the forced vibration of a row of rectangular panels which are stiffened transversely and simply supported along the longitudinal edges.

The differential equation governing the panel vibration shown in figure 2.2 may be written as (Leissa 1993)

$$\rho h\ddot{\tilde{u}}_z(x,y,t) + D\nabla^4\tilde{u}_z(x,y,t) = \tilde{f}(x,y,t), \tag{2.25}$$

with stress-displacement relations

$$\tilde{M}_{xx} = -D\left(\frac{\partial^2\tilde{u}_z}{\partial x^2} + \mu\frac{\partial^2\tilde{u}_z}{\partial y^2}\right),\quad \tilde{M}_{yy} = -D\left(\frac{\partial^2\tilde{u}_z}{\partial y^2} + \mu\frac{\partial^2\tilde{u}_z}{\partial x^2}\right),$$

$$\tilde{M}_{xy} = \tilde{M}_{yx} = -D(1-\mu)\frac{\partial^2\tilde{u}_z}{\partial x\partial y}, \tag{2.26}$$

$$\tilde{Q}_x = -D\left(\frac{\partial^3\tilde{u}_z}{\partial x^3} + \frac{\partial^3\tilde{u}_z}{\partial x\partial y^2}\right),\quad \tilde{Q}_y = -D\left(\frac{\partial^3\tilde{u}_z}{\partial y^3} + \frac{\partial^3\tilde{u}_z}{\partial x^2\partial y}\right). \tag{2.27}$$

Here $\tilde{f}(x,y,t)$ denotes the distribution of exciting force which includes the external transverse force and internal coupling force, ∇^4 represents the bi-harmonic operator, $\tilde{Q}_x, \tilde{Q}_y$ the transverse shear forces per unit length and $\tilde{M}_{xx}, \tilde{M}_{yy}, \tilde{M}_{xy}$ the internal bending moments and twisting moment per unit length. The plate flexural rigidity D is given by

$$D = \frac{Eh^3}{12(1-\mu^2)} \,. \tag{2.28}$$

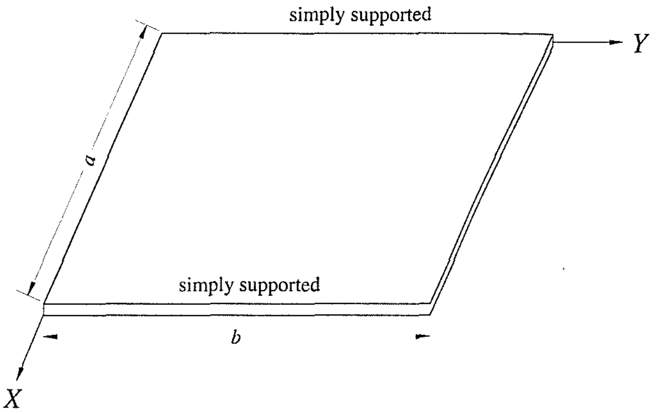

Figure 2.2. A uniform rectangular panel and its coordinate axis system.

If the panel is simply supported along the edges $x=0$ and $x=a$ then the deflection under harmonic excitation may be expanded in the form

$$\tilde{u}_z(x,y,t) = \sum_r Y_r(y)\sin(r\pi x/a) e^{i\omega t}. \tag{2.29}$$

Inserting equation (2.29) into equation (2.25), multiplying by $\sin(r\pi x/a)$, and integrating over x leads to the result

$$\left[D\frac{d^4Y_r}{dy^4} - 2Dk_r^2\frac{d^2Y_r}{dy^2} + Dk_r^4Y_r - \rho\omega^2Y_r \right] e^{i\omega t} = \frac{2}{a}\int_0^a \tilde{f} \cdot \sin k_r x \cdot dx, \tag{2.30}$$

where $k_r = r\pi/a$. If the excitation takes the form of a plane acoustic wave with

$$\tilde{f}(x,y,t) = \exp(-i\mu_1 x - i\mu_2 y + i\omega t), \tag{2.31}$$

then equation (2.30) may be rewritten as

$$\begin{aligned} D\frac{d^4Y_r}{dy^4} - 2Dk_r^2\frac{d^2Y_r}{dy^2} + Dk_r^4Y_r - \rho\omega^2Y_r &= \frac{2}{a}e^{-i\mu_2 y}\int_0^a e^{-i\mu_1 x} \cdot \sin k_r x \cdot dx \\ &= H_r(\mu_1)e^{-i\mu_2 y} \end{aligned} \,. \tag{2.32}$$

The solution of equation (2.32) consists of the sum of a complementary function and a particular integral in the form

$$Y_r(y)=\sum_{s=1}^{4} A_{rs}e^{k_{rs}y}+Y_{rp}(y)H_r(\mu_1), \tag{2.33}$$

where the A_{rs} terms are integration constants and k_{rs} are the four roots of the following equation in k:

$$Dk^4-2Dk_r^2k^2+(Dk_r^4-\rho\omega^2)=0. \tag{2.34}$$

The particular integral $Y_{rp}(y)$ appearing in equation (2.33) takes a number of different forms. A convenient form is given by the response of an infinite panel:

$$Y_{rp}(y)=e^{-\mathrm{i}\mu_2 y}\Big/\left[D\mu_2^4+2Dk_r^2\mu_2^2+Dk_r^4-\rho\omega^2\right]. \tag{2.35}$$

Using equations (2.26), (2.27) we find that the longitudinal effective shear force $Q_r(y)$ and bending moment $M_r(y)$ corresponding to the deflection $Y_r(y)$ are given respectively as

$$Q_r(y)=-D\left[\frac{d^3Y_r}{dy^3}-(2-\mu)k_r^2\frac{dY_r}{dy}\right], \tag{2.36}$$

$$M_r(y)=-D\left[\frac{d^2Y_r}{dy^2}-\mu k_r^2 Y_r\right]. \tag{2.37}$$

Equations (2.33), (2.36) and (2.37) imply that the relation between deflection vector $\{u_r\}^T=(Y_r(0),Y_r'(0),Y_r(b),Y_r'(b))$ and force vector $\{f_r\}^T=(Q_r(0),M_r(0),Q_r(b),M_r(b))$ is expressible as

$$\{f_r\}=[D_r]\{u_r\}+\{d_r\}H_r(\mu_1), \tag{2.38}$$

where $[D_r]$ denotes the dynamic stiffness matrix and $\{d_r\}$ the panel force vector (see, Langley 1989). Equation (2.38) gives the dynamic properties of a single panel element in a form which allows the behaviour of a complete panel row to be analysed by using the force balance conditions and geometrical compatibility equations at the coupling edges of each panel. If panel *j* and *j+1* are coupled at their edges in the same co-ordinate system, the force balance conditions and geometrical compatibility equations are given by

$$Q_r^{(j)}(b^{(j)})+Q_r^{(j+1)}(0)=0,\quad M_r^{(j)}(b^{(j)})+M_r^{(j+1)}(0)=0, \tag{2.39}$$

$$Y_r^{(j)}(b^{(j)}) = Y_r^{(j+1)}(0), \qquad Y_r'^{(j)}(b^{(j)}) = Y_r'^{(j+1)}(0), \tag{2.40}$$

where $b^{(j)}$ is the length of panel *j*. The information contained through assembly of all panels of the system and equation (2.38) allows the deflection vector $\{u_r\}$ to be determined.

2.4. Travelling Wave and Scattering Approach

Miller & Flotow (1989), Horner & White (1991), Beale & Accorsi (1995) presented the travelling wave and scattering approach and its application to a beam frame system.

In this approach, each structural member is treated as a waveguide which transmits axial, torsional and flexural wave modes. The waveguide equations relate a member's state vector to wave mode amplitudes expressed as

$$\begin{Bmatrix} u \\ f \end{Bmatrix} = \begin{bmatrix} Z_{uL} & Z_{uR} \\ Z_{fL} & Z_{fR} \end{bmatrix} \begin{Bmatrix} w_L \\ w_R \end{Bmatrix}. \tag{2.41}$$

Here *u* and *f* are the generalised displacement and force vectors at one end of the beam and w_L and w_R are the wave mode amplitude coefficients.

The waveguide equations for axial modes are found by solving the following equations for harmonic vibration of a rod

$$E\frac{\partial^2 u_x}{\partial x^2} + \rho\omega^2 u_x = 0, \tag{2.42}$$

$$N = EA\frac{\partial u_x}{\partial x}, \tag{2.43}$$

where u_x and N are the axial displacement and force, respectively.

The solution of equation (2.42) may be written as

$$u_x(x) = u_L e^{ik_A x} + u_R e^{-ik_A x}, \tag{2.44}$$

where u_L and u_R denote wave mode amplitude coefficients, $k_A = \sqrt{\rho\omega^2/E}$. The substitution equations of (2.43) and (2.44) into equation (2.41) yields the following waveguide equations for axial modes at both left and right ends of the beam:

$$\begin{Bmatrix} u_x \\ N \end{Bmatrix}_L = \begin{bmatrix} 1 & 1 \\ \mathrm{i}k_A EA & -\mathrm{i}k_A EA \end{bmatrix} \begin{Bmatrix} u_L \\ u_R \end{Bmatrix}. \tag{2.45}$$

$$\begin{Bmatrix} u_x \\ N \end{Bmatrix}_R = \begin{bmatrix} e^{\mathrm{i}k_A L} & e^{-\mathrm{i}k_A L} \\ \mathrm{i}k_A EAe^{\mathrm{i}k_A L} & -\mathrm{i}k_A EAe^{-\mathrm{i}k_A L} \end{bmatrix} \begin{Bmatrix} u_L \\ u_R \end{Bmatrix}. \tag{2.46}$$

Similarly, the twist angle θ_{xy} and torque M_{xy} for harmonic torsional vibration at the left end of a uniform beam are given by

$$\begin{Bmatrix} \theta_{xy} \\ M_{xy} \end{Bmatrix}_L = \begin{bmatrix} 1 & 1 \\ \mathrm{i}k_T GJ & -\mathrm{i}k_T GJ \end{bmatrix} \begin{Bmatrix} \phi_L \\ \phi_R \end{Bmatrix}. \tag{2.47}$$

Here ϕ_L and ϕ_R denote the wave mode amplitude coefficients of torsional vibration. The waveguide equation for the right end of the beam has a similar form.

For the flexural vibration of a uniform Euler-Bernoulli beam, the differential equations of motion are given by

$$-EI\frac{\partial^4 \tilde{u}_y(x,t)}{\partial x^4} + \rho A\frac{\partial^2 \tilde{u}_y(x,t)}{\partial t^2} = 0 \tag{2.48}$$

with stress-displacement relations,

$$\tilde{Q}(x,t) = -EI\frac{\partial^3 \tilde{u}_y(x,t)}{\partial x^3}, \tag{2.49}$$

$$\tilde{M}(x,t) = -EI\frac{\partial^2 \tilde{u}_y(x,t)}{\partial x^2}. \tag{2.50}$$

The solution of equation (2.48) is written as

$$u_y(x) = \sum_{j=1}^{4} w_j e^{\mathrm{i}k_j x}, \tag{2.51}$$

where $k_1 = -k_2 = \left(\rho A\omega^2/EI\right)^{1/4}$, $k_3 = -k_4 = \mathrm{i}\left(\rho A\omega^2/EI\right)^{1/4}$. (2.52)

Using equations (2.49)-(2.52), it is found that the waveguide equations at the both ends of the beam are given by

$$\begin{Bmatrix} u_y \\ \theta \\ M \\ Q \end{Bmatrix}_L = \begin{bmatrix} 1 & 1 & 1 & 1 \\ a_1 & a_2 & a_3 & a_4 \\ b_1 & b_2 & b_3 & b_4 \\ c_1 & c_2 & c_3 & c_4 \end{bmatrix} \begin{Bmatrix} w_1 \\ w_2 \\ w_3 \\ w_4 \end{Bmatrix}, \tag{2.53}$$

$$\begin{Bmatrix} u_y \\ \theta \\ M \\ Q \end{Bmatrix}_R = \begin{bmatrix} e^{ik_1L} & e^{ik_2L} & e^{ik_3L} & e^{ik_4L} \\ a_1e^{ik_1L} & a_2e^{ik_2L} & a_3e^{ik_3L} & a_4e^{ik_4L} \\ b_1e^{ik_1L} & b_2e^{ik_2L} & b_3e^{ik_3L} & b_4e^{ik_4L} \\ c_1e^{ik_1L} & c_2e^{ik_2L} & c_3e^{ik_3L} & c_4e^{ik_4L} \end{bmatrix} \begin{Bmatrix} w_1 \\ w_2 \\ w_3 \\ w_4 \end{Bmatrix}, \tag{2.54}$$

where $a_j = \mathrm{i}k_j,\ b_j = -EIk_j^2,\ c_j = -\mathrm{i}EIk_j^3, j=1,2,3,4.$ (2.55)

These waveguide equations are derived in a local co-ordinate system, they may be changed to global co-ordinate system by a transformation matrix $[Tr]$. That is

$$\begin{Bmatrix} u \\ f \end{Bmatrix}_G = [Tr]\begin{Bmatrix} u \\ f \end{Bmatrix} = [Tr]\begin{bmatrix} Z_{uL} & Z_{uR} \\ Z_{fL} & Z_{fR} \end{bmatrix}\begin{Bmatrix} w_L \\ w_R \end{Bmatrix}. \tag{2.56}$$

Concepts such as continuity of member displacements, equilibrium of member forces and satisfaction of displacement boundary conditions at a junction are used to calculate the junction scattering. The condition that must be satisfied at a junction or boundary in which the junction force or displacement is prescribed is written as

$$f_1 + f_2 + \cdots + f_n = \hat{F}, \tag{2.57}$$

$$u_1 = u_2 = \cdots = u_n = \hat{U}, \tag{2.58}$$

where n denotes the total number of beams connected to the junction, $\hat{F}$ and $\hat{U}$ denote prescribed junction loads and displacements respectively.

The substitution of equation (2.56) into equations (2.57), (2.58) yields the junction scattering equation as follows

$$\{w_R\} = [S]\{w_L\} + [G]\{R\}, \tag{2.59}$$

where $[S]$, $[G]$ are called the junction scattering and generation matrices respectively and $\{R\}$ denote the generalised junction loads.

After solving equation (2.59), the displacement, coupling force and power flow at the junction may be obtained using equations (2.4), (2.5) and (2.56).

2.5. Field Equations and Power Flow in Viscoelastic Continuum

The power flow approaches presented previously focus on specific application to beam and plate structures. Here the general description of power flow in a continuum is introduced.

2.5.1. Field Equation

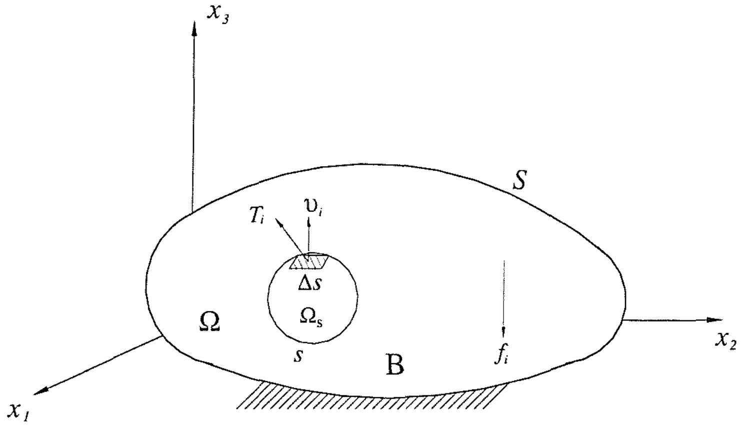

Figure 2.3 Energy transmission from one part to another in the elastic body

To develop field equations and a power flow equation in a continuum, a standard Cartesian tensor notation and a summation convention (see, for example, Reismann & Pawlik 1980 or Xing & Price 1999) are used herein. Therefore any valuable with a subscript *i, j, k* or *l* (*i, j, k, l*=1,2,3) indicates the valuable is a vector.

The equation of motion of the continuum system is expressed as

$$\sigma_{ij,j} + \hat{f}_i = \rho \dot{v}_i, \qquad (2.60)$$

where σ_{ij} denotes a stress tensor, $\sigma_{ij,j} = {}^{\partial \sigma_{ij}}\!/_{\partial x_j}$, $\hat{f}_i$ a body force per unit volume of the continuum, ρ represents the density and $v_i, \dot{v}_i$ the velocity and acceleration along the *i*th direction respectively.

When a sinusoidal exciting force is applied to a viscoelastic solid, the strain e_{ij} is observed to lag behind the stress. Their relative phase angle φ denotes a loss angle. In engineering analysis, the hysteretic energy-absorption mechanism related to linear viscoelastic materials is normally introduced into Hook's constitutive equation (see, for example, Cremer *et al* 1988) defining the elastic solid by a complex modulus of elasticity. That is,

$$\tilde{\sigma}_{ij} = \tilde{C}_{ijkl}\tilde{e}_{kl}, \quad \tilde{C}_{ijkl} = C_{ijkl}(1+\mathrm{i}\eta), \tag{2.61}$$

where the real part of the complex modulus represents the stiffness of the material in association with a storage modulus coefficient, and the imaginary part represents the damping capacity of the material and hence is associated with a loss modulus coefficient.

If the complex strain has the form

$$\begin{aligned}\tilde{e}_{ij} &= E_{ij}e^{\mathrm{i}(\omega t+\varphi)} = E_{ij}\left(\cos(\omega t+\varphi)+\mathrm{i}\sin(\omega t+\varphi)\right)\\ &= e_{ij} - \mathrm{i}\left(\dot{e}_{ij}\big/\omega\right),\end{aligned} \tag{2.62}$$

the complex stress in equation (2.61) becomes

$$\begin{aligned}\tilde{\sigma}_{ij} &= C_{ijkl}(1+\mathrm{i}\eta)E_{kl}e^{\mathrm{i}(\omega t+\varphi)}\\ &= C_{ijkl}\left(e_{kl}+(\eta/\omega)\dot{e}_{kl}\right)+\mathrm{i}C_{ijkl}\left(\eta e_{kl}-\dot{e}_{kl}/\omega\right).\end{aligned} \tag{2.63}$$

Therefore the real form of the constitutive equation representing a viscoelastic material is expressed as

$$\sigma_{ij} = \sigma_{ij}^{e} + \sigma_{ij}^{d} = C_{ijkl}e_{kl} + C_{ijkl}(\eta/\omega)\dot{e}_{kl}. \tag{2.64}$$

The strain – displacement relation is given by

$$e_{ij} = \frac{1}{2}\left(u_{i,j}+u_{j,i}\right) \tag{2.65}$$

and the rate of strain by

$$\dot{e}_{ij} = (e_{ij})_{,t} = \frac{1}{2}\left(v_{i,j}+v_{j,i}\right), \tag{2.66}$$

where u_i denotes the displacement and $u_{i,j} = \partial u_i \big/ \partial x_j$.

For a problem in solid mechanics, the traction condition on the boundary S_T and the displacement condition on the displacement boundary S_U are usually defined as

$$\text{Traction:} \qquad \sigma_{ij}\upsilon_j = \hat{T}_i \quad \text{on } S_T, \tag{2.67}$$

$$\text{Displacement:} \quad u_i = \hat{U}_i \qquad \text{on } S_U, \tag{2.68}$$

where υ_j denotes a unit normal.

2.5.2. Energy Flow Components

The energy transmission from one part to another in a continuum excited by an external force can be investigated by analysing the energy flow across the closed surface s within the continuum B illustrated in Figure 2.3. Let Δs denote an elemental surface on s and υ_j a unit normal to Δs with its positive direction pointing outward from the (negative) interior to the (positive) exterior. The interactions between material lying on either side of this surface cause internal actions defined by the traction or stress vector T_i representing the force per unit area acting on the surface s. Through the rate of work done by this traction T_i, the power flow across the surface with unit normal υ_j is given by

$$q^{\upsilon} = -v_i T_i. \tag{2.69}$$

A positive value of q^{υ} represents the transmission of energy per unit time through the unit area of Δs from the material within s to the outside.

It follows from Cauchy's formula (see, for example, Fung 1965), that the traction

$$T_i = \sigma_{ij}\upsilon_j, \tag{2.70}$$

so,

$$q^{\upsilon} = -v_i\sigma_{ij}\upsilon_j = q_j\upsilon_j. \tag{2.71}$$

Here, the power flow density vector (see, Xing & Price 1999)

$$q_j = -v_i\sigma_{ij} = -\sigma_{ji}v_i \tag{2.72}$$

is defined by the dot product of the velocity v_i and stress tensor σ_{ij} and is a vector field function dependent on the co-ordinate x_j and time t. In a continuum mechanics approach, this power flow density vector specifies the energy transmission from one part to another per unit time in the dynamic system and allows the determination of power flow at each point in or on the continuum across any interface in any direction with unit normal υ_j through the expression given in equation (2.71). Physically, the *j*th component q_j of the power flow density vector represents the summation of the individual power done by the three stress components σ_{1j}, σ_{2j} and σ_{3j} acting on a unit area with a normal along the *j*th direction of the co-ordinate system.

The time averaged quantity over a period of excitation T is given by

$$\langle q_j \rangle = \frac{1}{T}\int_0^T q_j dt, \tag{2.73}$$

and it is equivalent to the structural intensity parameter described by Hambric (1990), Gavic & Pavic (1993) and has similarity to an acoustic intensity parameter in a fluid domain being the product of pressure and the in-phase component of particle velocity (see, for example, Fahy 1989).

2.5.3. Equations of Energy Flow Balance

The transmission of energy within a continuum is governed by the law of conservation of energy. If heat conduction is neglected, the local equation of energy flow balance is derived from the field equations (2.60)-(2.68) (see, Xing & Price 1999).

Multiplying the motion equation (2.60) by the velocity v_i, we obtain

$$v_i\sigma_{ij,j} + v_i\hat{f}_i = v_i\rho\dot{v}_i, \tag{2.74}$$

and by using equation (2.72), it follows that

$$-q_{j,j} - v_{i,j}\sigma_{ij} + v_i\hat{f}_i = v_i\rho\dot{v}_i = \dot{K}, \tag{2.75}$$

where $\dot{K} = \partial K/\partial t = \partial(\frac{1}{2}\rho v_i^2)/\partial t$ denotes the rate of change of kinetic energy per unit volume. The strain energy density U and energy dissipation per unit volume D in a continuum is defined by (see, for example, Xing & Price 1999)

$$U = \int_0^{e_{ij}} \sigma_{ij}^e de_{ij} = \int_0^t \sigma_{ij}^e \dot{e}_{ij} dt, \tag{2.76}$$

$$D = \int_0^{e_{ij}} \sigma_{ij}^d de_{ij} = \int_0^t \sigma_{ij}^d \dot{e}_{ij} dt. \tag{2.77}$$

From equations (2.64)-(2.66), (2.76) and (2.77), the second term on the left hand of equation (2.75) can be expressed as

$$v_{i,j}\sigma_{ij} = \left(\sigma_{ij}^e + \sigma_{ij}^d\right)\dot{e}_{ij} = \dot{U} + \dot{D}. \tag{2.78}$$

Thus, the final form of the local equation of energy flow balance is given by

$$q_{j,j} = \hat{q}_f - \dot{E} - \dot{D}, \tag{2.79}$$

where $\hat{q}_f = v_i \hat{f}_i$ denotes the rate of energy input and $\dot{E} = \dot{K} + \dot{U}$ the rate of change of mechanical energy representing the ability of the continuum to store mechanical energy.

This equation, defined at any point in the continuum, states that the divergence of the energy flow density vector, i.e. the rate of energy transmission, equals the difference between the rate of energy input and the rate of energy stored and dissipated. The integration of the local energy balance equation (2.79) over the space subdomain Ω_s closed by the surface s (see, figure 2.3) and using Gauss divergence theory allows the integral equation of energy flow balance to be rewritten in the integral form

$$\int_s q_j \upsilon_j ds = \int_{\Omega_s} q_{j,j} d\Omega = \int_{\Omega_s} (\hat{q}_f - \dot{E} - \dot{D}) d\Omega \ . \tag{2.80}$$

The integral of the rate of energy flow on the surface s represents the power flow out of the closed surface s through the work done by the traction T_j. That is,

$$\int_s q_j \upsilon_j ds = \int_s q^{\upsilon} ds = \int_s -v_j T_j ds. \tag{2.81}$$

The integral equation (2.80) of energy flow balance states that the total power flow out of the surface s of the subdomain Ω_s through the rate of work done by the traction force on its surface s, in conjunction with the total rates of change of mechanical energy and energy dissipation in domain Ω_s balance the total power of work done by the external body force in this subdomain. If the integration is on the whole system B which is fixed or free at its boundary, there is no power output or input except excitations. Therefore, equation (2.80) becomes

$$\int_B \hat{q}_f d\Omega = \int_B \left(\dot{E} + \dot{D}\right) d\Omega. \tag{2.82}$$

This means that the total input power of external excitation balances the total rates of change of mechanical energy and energy dissipation in the system at any instant.

In the case of harmonic motions, the kinetic energy and the strain energy remain unchanged after every cycle and for stationary random processes (see, for example, Newland 1975 or Price & Bishop 1974), it follows that the time averaged values of the rates of change of kinetic energy density, the strain energy density are all zero, i.e.

$$\langle \dot{K} \rangle = \langle \dot{U} \rangle = \langle \dot{E} \rangle = 0. \tag{2.83}$$

Therefore, the time averaged power flow balance equation in the whole system is given by

$$\int_B \langle \hat{q}_f \rangle d\Omega = \int_B \langle \dot{D} \rangle d\Omega. \tag{2.84}$$

This means that the total input power of the system in a period of excitation balances the damping dissipation in this period.

3. A SUBSTRUCTURE APPROACH

3.1. Introduction

A substructure or a component mode synthesis approach is usually applied in a finite element analysis to reduce the number of degrees of freedom in the dynamic analysis of large complex structures. Such methods involve dividing the structure into a number of separate substructures or components. Each substructure is represented by modal substitution of a finite element model, a theoretical model or an experimental test model. All the substructures are then assembled together by applying interface conditions and the complete structure analysed. In this way, one large eigen problem is replaced by several smaller ones.

As mentioned previously in Chapter 1, the main advantage of such a technique is that long computer runs are avoided for a large, complicated structures.

There exist two major kinds of substructure approaches. That is, the fixed interface method described by Graig & Bampton (1968), Singh (1978) and the free interface method discussed by Cromer *et al.* (1976), Craig & Chang (1976). The basic steps of these two substructure approaches are the same. The approach presented herein may be classified as a free interface method but it differs from the traditional substructure method by the fact that (i) it does not require the eigen-solutions of the system and (ii) it derives the interface and system responses from the substructure modal parameters.

3.2. Basic Steps in the Substructure Approach

3.2.1. Division of the Structure

In any substructure approach, the first step, is to divide the complete system into a number of substructures. This is illustrated in figure 3.1 where a solid continuum system B with a closed surface S is divided into N substructures with total interfaces N_J. A whole system can be divided theoretically into any number of substructures of any shape. However, the basic rule of the division of the substructure is based on the geometrical or structural features. For example, the L-shaped plate system shown in Figure 5.2 is easily divided into two substructures, each substructure is a rectangular plate. The wings and fuselage of an aircraft are usually treated as different substructures according to their geometrical and structural characteristics.

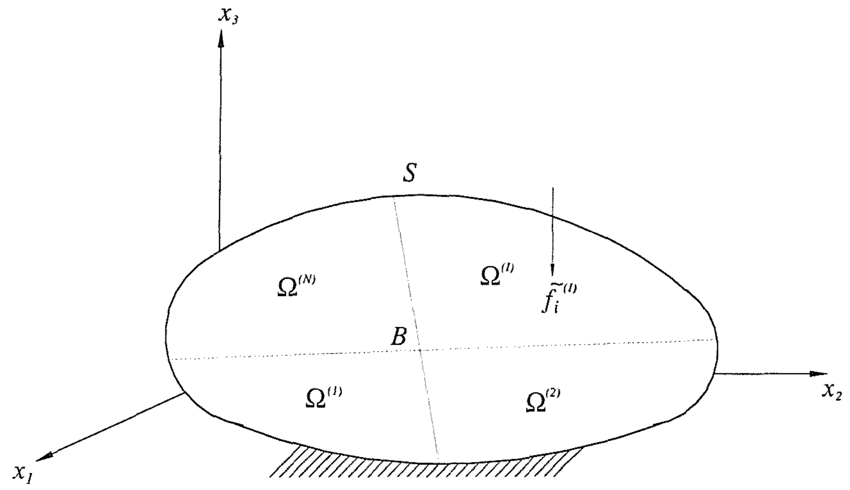

Figure 3.1. Division of a system B into N substructures.

3.2.2. Substructure Receptance Analysis

The second step is to determine the receptance or frequency response function of each substructure. Every substructure can be treated as an independent structure excited by prescribed external excitations $\tilde{f}_i^{(I)}$ and time, frequency dependent internal interface forces $\tilde{T}_i^{(I)}$. It is assumed that each substructure is a viscoelastic body and modal analysis applied to determine the receptance of each substructure. The key function of the modal analysis is to determine the natural frequencies and principal modal shapes of each substructure. Usually, three kinds of approaches are adopted to investigate the natural vibration of an engineering structure, i.e., theoretical solution, numerical calculation and measurement.

Theoretical Solution of Free Vibration of a Continuum

In some cases, when the geometry of the continuum is relatively simple (i.e., uniform beams, plates, etc), analytical solutions of boundary value problems can be generated without too much difficulty. The free bending and longitudinal vibration of uniform beams under almost all kinds of standard boundary conditions can be solved theoretically. However, for uniform plates, only a few cases have exact theoretical solutions. For example, a circular plate simply supported around its edge and a rectangular plate with two opposite simply supported edges. The free vibration solutions of uniform beams and plates are given by Meirovitch (1967), Timoshenko, Young & Weaver (1974), Bishop & Johnson (1979), Gorman (1982), Leissa (1993), etc and their solutions are discussed in the following chapters.

The main advantage of analytical solutions in substructure approaches lies in the convergence of the summation process especially for calculation of the power flow density vector because modes and internal forces have formulated expressions.

Numerical Approach

Many complex engineering structures are assembled with a wide range of different structural components and their receptance functions cannot be determined analytically. To circumvent these difficulties, analysts have applied various numerical techniques to the boundary value problems of elasticity, structural mechanics and vibration.

The essential feature of numerical methods is that the original boundary value problem is replaced by a finite set of simultaneous algebraic equations. The solution of this set of simultaneous equations provides an approximation for displacement or stress in the continuum. This feature makes these methods readily amenable to computer implementation. The more popular numerical approaches are Ritz method, weighted residual method, finite difference method and finite element method (see, for example, Zienkiewicz 1971 or Reismann & Pawlik 1980). The finite element method (FEM) is the most widely used computational scheme to solve problems in the theory of elasticity and vibration.

The idea behind the FEM is quite simple and physically appealing. The given structure is viewed as an assembly of a finite number of elements. These elements are normally chosen because they occur naturally, such as the members in a truss or frame, or because they possess a simple geometrical shape. The displacement in each element is then determined or assumed in terms of its values at certain points in the element called nodes. The nodal degrees of freedom, as they are called, determine the desired solution within each element. When the elements are pieced together to form the structure of interest, one obtains a piecewise approximation for displacement in the entire structure in terms of the as yet unknown nodal degrees of freedom. The total displacement field is then required to satisfy either a variational principle, a conservation law, or an equilibrium condition. This requirement results in a set of linear eigenvalue equations which can be solved for the natural frequencies and mode shapes associated with the continuum. Detailed explanations of finite element vibration analysis are given by Zienkiewicz (1971) and Petyt (1990).

In the substructure approach, each substructure of the continuum system is discretized, the dynamic equation of motion of the form with a loss factor $\eta^{(I)}$ is described by

$$\left[M^{(I)}\right]\left\{\ddot{u}^{(I)}\right\}+\left(1+\mathrm{i}\eta^{(I)}\right)\left[K^{(I)}\right]\left\{u^{(I)}\right\}=\left\{f^{(I)}\right\}+\left\{T^{(I)}\right\},\ I=1,2,\ldots,N, \tag{3.1}$$

where $\left[M^{(I)}\right]$, $\left[K^{(I)}\right]$ denote the mass and stiffness matrices of the Ith substructure, $\left\{u^{(I)}\right\}$ the vector of nodal degrees and $\left\{f^{(I)}\right\}$, $\left\{T^{(I)}\right\}$ the vectors of external exciting nodal forces and coupling forces at the nodes of the interface of the Ith substructure, respectively. There exist several methods to solve the linear eigenvalue problem of equation (3.1) given by the equation

$$-\omega^2\left[M^{(I)}\right]\left[u^{(I)}\right]+\left[K^{(I)}\right]\left[u^{(I)}\right]=0. \tag{3.2}$$

For example (see, Petyt 1990), the Jacobi method to solve for all eigenvalues and eigenvectors simultaneously, or a subspace iteration method for solution of large eigenvalue problems.

Experimental Investigations

If a particular substructure is difficult to model using finite element techniques, its modal representation and receptance function can be determined experimentally and included in a substructure synthesis. It is simpler to test the modal component with free interface boundaries rather than fixed, and therefore a free interface method is easier to use to derive test results. Examples of the combined use of theoretical and experimental models are discussed by Cromer & Lalanne (1976). For a dynamic analysis, a value of the damping loss factor is necessary but cannot be obtained analytically and therefore resort to experiments is the only way to obtain such information for engineering structures.

3.2.3. Substructure Synthesis

The last step in a substructure approach is synthesis of the substructure equations using the displacement compatibility condition and force balance equations at the interfaces of substructures. At an interface between two substructures, the displacements determined by substructure modal analysis at the interfaces of these two substructures should be same and the coupling forces balance. The assembly of the displacement compatibility and force balance conditions at all interfaces of the system allows the coupling forces between the interfaces of substructures to be determined.

3.3. Mathematical Model of the Substructure Approach

3.3.1. Receptance Function of a Substructure

Similar to **2.5.**, a standard Cartesian tensor notation and a summation convention are used herein. Let us examine the dynamics of an elastic body B occupying a domain Ω which has its fixed boundary S_u and traction boundary S_T. It is assumed that this elastic body is subject to a prescribed boundary displacement $\hat{u}_i = 0$ on boundary S_u, traction $\hat{T}_i$ on boundary S_T and body force $\tilde{f}_i$. All these forces are assumed to be harmonic variables with frequency ω.

In the substructure approach, the elastic body is divided into a number of substructures. This is illustrated in figure 3.1 where a whole system B with a closed surface S is divided into N substructures with total interfaces N_J. Each substructure I with its domain $\Omega^{(I)}$, prescribed displacement boundary $S_u^{(I)}$, traction boundary $S_T^{(I)}$ (I=1,2,...,N) and interface $s^{(IJ)}$ (J=1,2,...,N_{IJ}, where N_{IJ} is the total interface number on the Ith substructure) is treated as an independent structure but excited by external excitations $\tilde{f}_i^{(I)}$ and time, frequency dependent internal interface forces $\tilde{T}_i^{(I)}$. The governing equations describing the dynamics of this body are as follows (see, for example, Xing & Price, 1999).

Dynamic equation of motion

$$\rho \ddot{\tilde{u}}_i^{(I)} = \tilde{\sigma}_{ij,j}^{(I)} + \tilde{f}_i^{(I)}, \ x \in \Omega^{(I)}, \ I = 1,2,\ldots,N. \tag{3.3}$$

Constitutive equation

$$\tilde{\sigma}_{ij}^{(I)} = \tilde{C}_{ikjl}^{(I)} \tilde{e}_{kl}^{(I)}, \quad \tilde{C}_{ijkl}^{(I)} = C_{ijkl}^{(I)}(1 + \mathrm{i}\eta), \tag{3.4}$$

Strain – displacement relation

$$\tilde{e}_{kl}^{(I)} = \frac{1}{2}\left(\tilde{u}_{k,l}^{(I)} + \tilde{u}_{l,k}^{(I)}\right) \tag{3.5}$$

Boundary conditions

$$\tilde{u}_i^{(I)} = \hat{u}_i^{(I)} = 0, \qquad x \in S_u^{(I)}. \tag{3.6}$$

$$\tilde{\sigma}_{ij}^{(I)} \upsilon_j^{(I)} = \hat{T}_i^{(I)}, \qquad x \in S_T^{(I)}, \tag{3.7}$$

Internal interface force condition

$$\tilde{\sigma}_{ij}^{(I)} \upsilon_j^{(I)} = \tilde{T}_i^{(I)}, \ x \in s^{(IJ)}, \ J = 1,2,\ldots,N_{IJ}, \tag{3.8}$$

where ρ is the density of the substructure, $s^{(IJ)}$ denotes the Jth interface of the Ith substructure.

If the traction boundary $S_T^{(I)}$ is assumed free, boundary condition (3.7) becomes

$$\tilde{\sigma}_{ij}^{(I)} \upsilon_j^{(I)} = 0, \qquad x \in S_T^{(I)}, \tag{3.9}$$

For a harmonic motion, a set of boundary conditions which describe how the viscoelastic body is supported and how it comes into contact with other media along its boundary and interfaces (equations 3.6-3.9), together with the differential equation (3.3) of motion, constitute a *boundary-value* problem.

According to a theorem due to Rayleigh (1894), any distortion of a substructure may be expressed as an aggregate of distortions in its principal modes. That is

$$\tilde{u}_i^{(I)} = \sum_{r=1}^{n} \varphi_i^{(r),(I)} \tilde{p}^{(r),(I)}(t), \quad x \in \Omega^{(I)}, \quad I=1,2,\ldots,N \tag{3.10}$$

where $\varphi_i^{(r),(I)}$, $\tilde{p}^{(r),(I)}(t)$ denote the *r*th principal modal shape and principal co-ordinate of the *I*th substructure in the system and *n* modes are admitted into the analysis. From equations (3.3)-(3.9), the *boundary-value* problem of no damping free vibration is given by

$$\begin{cases} C_{ijkl}^{(I)} \tilde{u}_{k,lj}^{(I)} = \rho \ddot{\tilde{u}}_i, & x \in \Omega^{(I)}, \\ C_{ijkl}^{(I)} \tilde{u}_{k,l}^{(I)} \upsilon_j = 0, & x \in S_T^{(I)}, \\ \tilde{u}_i^{(I)} = 0, & x \in S_u^{(I)}. \end{cases} \tag{3.11}$$

The natural vibration of the elastic structure is given by $\tilde{u}_i^{(I)} = U_i^{(I)} e^{i\omega t}$ from which it follows that

$$\begin{cases} C_{ijkl}^{(I)} U_{k,lj}^{(I)} = -\rho \omega^2 U_i^{(I)}, \\ C_{ijkl}^{(I)} U_{k,l}^{(I)} \upsilon_j = 0, \quad x \in S_T^{(I)}, \\ U_i^{(I)} = 0, \quad\quad x \in S_u^{(I)}. \end{cases} \tag{3.12}$$

The natural frequency ω_r and mode shape $\varphi_i^{(r),(I)}$ (r =1,2,..., n) are determined from equation (3.12) using analytical, numerical or test methods. These principal mode shapes of a three-dimensional elastic structure are orthogonal as discussed in Appendix A and satisfy

$$\int_{\Omega^{(I)}} \rho \varphi_i^{(r),(I)} \varphi_i^{(q),(I)} d\Omega = \delta_{rq} m_r = \begin{cases} m_r & r = q \\ 0 & r \neq q \end{cases}, \tag{3.13}$$

$$\begin{aligned} \int_{\Omega^{(I)}} \varphi_{i,j}^{(r),(I)} C_{ijkl}^{(I)} \varphi_{k,l}^{(q),(I)} d\Omega &= -\int_{\Omega^{(I)}} \varphi_i^{(r),(I)} C_{ijkl}^{(I)} \varphi_{k,lj}^{(q),(I)} d\Omega \\ &= \delta_{rq} K_r = \begin{cases} m_r \omega_r^2 & r = q \\ 0 & r \neq q \end{cases} \end{aligned}, \tag{3.14}$$

where δ_{rq} is the *Kronecker* delta and m_r a generalised modal mass.

From equations (3.4), (3.5), (3.10) and (3.11), the differential equation of motion (3.3) of the *I*th substructure under a harmonic excitation takes in the form

$$-\rho\omega^2\sum_{r=1}^{n}\varphi_i^{(r),(I)}\tilde{p}^{(r),(I)}(t)-\tilde{C}_{ijkl}^{(I)}\sum_{r=1}^{n}\varphi_{i,lj}^{(r),(I)}\tilde{p}^{(r),(I)}(t)=\tilde{f}_i^{(I)},\quad x\in\Omega^{(I)} \tag{3.15}$$

with boundary conditions and internal interface force condition as follows

$$C_{ijkl}^{(I)}\sum_{r=1}^{n}\phi_{i,l}^{(r),(I)}\upsilon_j^{(I)}\tilde{p}^{(r),(I)}(t)=\hat{T}_i^{(I)},\quad x\in S_T^{(I)}\ , \tag{3.16}$$

$$\sum_{r=1}^{n}\ \phi_i^{(r),(I)}\tilde{p}^{(r),(I)}(t)=0,\quad x\in S_u^{(I)}, \tag{3.17}$$

$$C_{ijkl}^{(I)}\sum_{r=1}^{n}\phi_{i,l}^{(r),(I)}\upsilon_j^{(I)}\tilde{p}^{(r),(I)}(t)=\tilde{T}_i^{(I)},\quad x\in s^{(IJ)}\ , \tag{3.18}$$

$$(I=1,2,3,\ldots,N;\ \ J\in N_{IJ}).$$

Pre-multiplying equation (3.15) by $\varphi_i^{(q),(I)}$, integrating over the domain $\Omega^{(I)}$ and using boundary conditions and internal interface force conditions (3.16)-(3.18), Green theorem (see, for example, Fung 1965) and the orthogonality of the principal mode shapes (3.13), (3.14) yields the principal co-ordinate in the form

$$\tilde{p}^{(r),(I)}(t)=\frac{\int_{\Omega^{(I)}}\tilde{f}_i^{(I)}\varphi_i^{(r),(I)}d\Omega+\int_{S_T^{(I)}}\hat{T}_i^{(I)}\varphi_i^{(r),(I)}dS+\int_{s^{(IJ)}}\tilde{T}_i^{(I)}\varphi_i^{(r),(I)}dS}{m_r\left((\omega_r)^2-\omega^2+\mathrm{i}(\omega_r)^2\right)}. \tag{3.19}$$

Furthermore, if the traction boundary $S_T^{(I)}$ is assumed free and the external exciting forces and internal coupling forces are assumed concentrated forces, using equations (3.10) and (3.19), the distortion at any interface of the *I*th substructure can be expressed as

$$\tilde{u}_i^{(I)}=R_e^{(I)}\tilde{f}_i^{(I)}+R_s^{(I)}\tilde{T}_i^{(I)},\ I=1,2,\ \ldots,\ N. \tag{3.20}$$

where $R_e^{(I)}$ and $R_s^{(I)}$ denote the interface receptance function under external excitations and internal coupling forces of the *I*th substructure respectively.

Therefore, the response of the viscoelastic continuum is determined after the natural frequencies and principal modal shapes of the structure are determined.

3.3.2. Coupling Relation and Synthesis of Substructures

In a continuum system, at any elemental surface Δs on the interface $s^{(IJ)}$ between any two substructures, the interactions between material lying on either side of this surface cause internal actions defined by the complex traction force vector $\tilde{T}_i^{(I)}$ (I=1,2,...,N) on substructure $\Omega^{(I)}$, representing the force per unit area acting on the interface $s^{(IJ)}$. Therefore, each sub-domain is treated as an independent uncoupled system with two kinds of force acting on it. One is the external exciting force whereas the other is the internal coupling traction force applied at the interface. These latter quantities are unknowns which must be determined. This is achieved through the force balance conditions and geometric compatibility equations at all interfaces, which allow a set of linear simultaneous equations to be constructed. These equations can be solved and the coupling forces determined. The internal traction force balance condition and the displacement compatibility equation at any point over interface $s^{(IJ)}$ of two adjacent substructures I and J (see, for example, figure 3.2) are given by

$$\tilde{T}_i^{(I)} + \tilde{T}_i^{(J)} = 0 \text{ and } \tilde{u}_i^{(I)} = \tilde{u}_i^{(J)} \text{ on } s^{(IJ)}, \tag{3.21}$$

respectively, where $I \leq N$, $J \leq N_{IJ}$ and $J \neq I$.

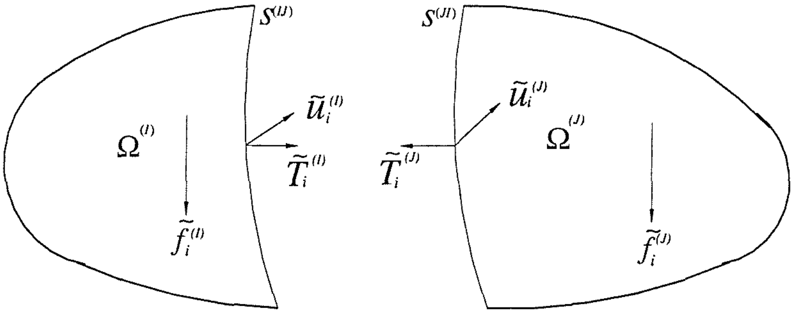

Figure 3.2. Schematic illustration of interface condition between two substructures.

In engineering applications, the interface $s^{(IJ)}$ should be divided into a series of (for example, N_{SIJ}) small areas Δs. Assuming there exists K_I external exciting force in $\Omega^{(I)}$, the displacement response at any position of an interface of each substructure determined by either a theoretical model or a FEA model under the external exciting forces $\{\tilde{f}^{(I)}\}$ and internal coupling forces $\left\{\tilde{T}^{(I)}\right\}$ having the matrix form

$$\left\{\tilde{u}_i^{(I)}\right\}_{3\times1} = \left[R_e^{(I)}\right]_{3\times K_I}\left\{\tilde{f}^{(I)}\right\}_{K_I\times1} + \left[R_s^{(I)}\right]_{3\times3N_{SIJ}}\left\{\tilde{T}^{(I)}\right\}_{3N_{SIJ}\times1}, \quad x\in s^{(IJ)},$$

$$i=1,2,3,\ I=1,2,\ldots,N. \qquad (3.22)$$

The displacement response and interface force vectors of a substructure given by equation (3.22) are usually expressed in a local co-ordinate system. These are related to those in the global co-ordinate (x_1, x_2, x_3) by an orthogonal co-ordinate transformation matrix $[tr]$ (see, for example, Reismann & Pawlik 1980) expressed as

$$\left\{\tilde{u}_{(g)}^{(I)}\right\}_{3\times1} = \left[tr^{(I)}\right]_{3\times3}\left\{\tilde{u}_i^{(I)}\right\}_{3\times1} \ and \ \left\{\tilde{T}_{(g)}^{(I)}\right\}_{3\times1} = \left[tr^{(I)}\right]_{3\times3}\left\{\tilde{T}_i^{(I)}\right\}_{3\times1}, \quad I=1,2,\ldots,N. \qquad (3.23)$$

Therefore, the coupling relations given in equation (3.21) become

$$\left[tr^{(I)}\right]_{3\times3}\left\{\tilde{T}_i^{(I)}\right\}_{3\times1} + \left[tr^{(J)}\right]_{3\times3}\left\{\tilde{T}_i^{(J)}\right\}_{3\times1} = 0 \qquad (3.24)$$

and

$$\left[tr^{(I)}\right]_{3\times3}\left\{\tilde{u}_i^{(I)}\right\}_{3\times1} = \left[tr^{(J)}\right]_{3\times3}\left\{\tilde{u}_i^{(J)}\right\}_{3\times1} \quad \text{on } s^{(IJ)}. \qquad (3.25)$$

The assembly of the coupling relation equations (3.24) and (3.25) at all interfaces of the system and their combination with the receptance function (3.22) of all N substructures yield a homogeneous set of linear algebraic equations for the coupling forces $\left\{\tilde{T}_i^{(I)}\right\}$ and displacement $\left\{\tilde{u}_i^{(I)}\right\}$ ($i=1,2,3$, $I=1,2,\ldots,N$) at all interfaces. It therefore follows that the response of the whole system can be determined after solutions of the receptance functions of all substructures.

If the whole system contains only two substructures as illustrated in figure 3.2, the synthesis process is relatively simple. For example, the force balance condition and the displacement compatibility equation at all positions of the interface take the simplified form

$$\left[Tr^{(1)}\right]_{3N_{S12}\times3N_{S12}}\left\{\tilde{u}^{(1)}\right\}_{3N_{S12}\times1} = \left[Tr^{(2)}\right]_{3N_{S12}\times3N_{S12}}\left\{\tilde{u}_i^{(2)}\right\}_{3N_{S12}\times1}, \qquad (3.26)$$

$$\left[Tr^{(1)}\right]_{3N_{S12}\times3N_{S12}}\left\{\tilde{T}^{(1)}\right\}_{3N_{S12}\times1} + \left[Tr^{(2)}\right]_{3N_{S12}\times3N_{S12}}\left\{\tilde{T}^{(2)}\right\}_{3N_{S12}\times1} = 0, \text{ on } s^{(12)}, \qquad (3.27)$$

where $\left[Tr^{(I)}\right]$ denotes the co-ordinate transformation matrix of all points of the interface of substructure I and $\left[Tr^{(I)}\right]_{3N_{S12}\times 3N_{S12}} = \begin{bmatrix} \left[tr^{(I)}\right] & 0 & 0 & 0 \\ 0 & \left[tr^{(I)}\right] & 0 & 0 \\ 0 & 0 & \ddots & 0 \\ 0 & 0 & 0 & \left[tr^{(I)}\right] \end{bmatrix}$, I=1,2.

The substitution of equation (3.22) into equation (3.26) gives

$$\begin{aligned} &\left[Tr^{(1)}\right]_{3N_{S12}\times 3N_{S12}}\left(\left[R_e^{(1)}\right]_{3N_{S12}\times K_1}\left\{\tilde{f}^{(1)}\right\}_{K_1\times 1}+\left[R_s^{(1)}\right]_{3N_{S12}\times 3N_{S12}}\left\{\tilde{T}_i^{(1)}\right\}_{3N_{S12}\times 1}\right) \\ &=\left[Tr^{(2)}\right]_{3N_{S12}\times 3N_{S12}}\left(\left[R_e^{(2)}\right]_{3N_{S12}\times K_2}\left\{\tilde{f}^{(2)}\right\}_{K_2\times 1}+\left[R_s^{(2)}\right]_{3N_{S12}\times 3N_{S12}}\left\{\tilde{T}_i^{(2)}\right\}_{3N_{S12}\times 1}\right)\end{aligned}, \quad (3.28)$$

and the coupling force vectors at interface determined from the equation

$$\begin{aligned}\left\{\tilde{T}^{(1)}\right\} &= \left(\left[Tr^{(2)}\right]\left[R_s^{(2)}\right]\left[Tr^{(2)}\right]^{-1}\left[Tr^{(1)}\right]+\left[Tr^{(1)}\right]\left[R_s^{(1)}\right]\right)^{-1}\times \\ &\left\{\left[Tr^{(2)}\right]\left[R_e^{(2)}\right]\left\{\tilde{f}^{(2)}\right\}-\left[Tr^{(1)}\right]\left[R_e^{(1)}\right]\left\{\tilde{f}^{(1)}\right\}\right\},\end{aligned} \quad (3.29)$$

$$\left\{\tilde{T}^{(2)}\right\} = -\left[Tr^{(2)}\right]^{-1}\left[Tr^{(1)}\right]\left\{\tilde{T}^{(1)}\right\}. \quad (3.30)$$

It follows that the responses of all substructures are determined using equation (3.10).

In many engineering applications, substructures are connected by spring dampers. In the general situation, these spring dampers are treated as independent substructures. If the spring dampers between the interfaces are assumed massless, to simplify calculation, the couplings between substructures are treated as compliant and dissipative. Let us assume that the dampers are described by a complex stiffness value at any position in the interface given by

$$\tilde{K}_D = K_D(1+\mathrm{i}\eta_D). \quad (3.31)$$

The force balance condition and the geometrical compatibility equation in equations (3.26), (3.27) become

$$\left[Tr^{(1)}\right]\left\{\tilde{T}^{(1)}\right\} = \left[\tilde{K}_D\right]\left(\left[Tr^{(2)}\right]\left\{\tilde{u}^{(2)}\right\}-\left[Tr^{(1)}\right]\left\{\tilde{u}^{(1)}\right\}\right), \quad (3.32)$$

$$\left[Tr^{(1)}\right]\left\{\tilde{T}^{(1)}\right\}+\left[Tr^{(2)}\right]\left\{\tilde{T}^{(2)}\right\} = 0. \quad (3.33)$$

Using the equation (3.22), we find that the coupling forces at the compliant and dissipative interface can be written as

$$\begin{aligned}\left[Tr^{(1)}\right]\left\{T^{(1)}\right\} = &\left([\mathrm{I}] + \left[\tilde{K}_D\right]\left[Tr^{(1)}\right]\left[R_s^{(1)}\right]\left[Tr^{(1)}\right]^{-1} + \left[\tilde{K}_D\right]\left[Tr^{(2)}\right]\left[R_s^{(2)}\right]\left[Tr^{(2)}\right]^{-1}\right)^{-1} \\ &\times\left[\tilde{K}_D\right]\left\{\left[Tr^{(2)}\right]\left[R_e^{(2)}\right]\left\{\tilde{f}^{(2)}\right\} - \left[Tr^{(1)}\right]\left[R_e^{(1)}\right]\left\{\tilde{f}^{(1)}\right\}\right\}.\end{aligned} \tag{3.34}$$

Here $[\mathrm{I}]$ is a unit matrix.

3.4. Power Flow Across an Interface

According to the general definition of power flow in equation (2.69), the power flow across an interface at any position $\mathbf{x}$ on the interface $s^{(IJ)}$ of the Ith substructure is given by

$$q^{(I)}(\mathbf{x}) = -\mathrm{Re}\left\{\dot{\tilde{u}}_i^{(I)}(\mathbf{x})\right\}\mathrm{Re}\left\{\tilde{T}_i^{(I)}(\mathbf{x})\right\}, \tag{3.35}$$

where the elements $\dot{\tilde{u}}_i^{(I)}(\mathbf{x})$ and $\tilde{T}_i^{(I)}(\mathbf{x})$ ($\mathbf{x} \in s^{(IJ)}$; I=1,2,…,N, $J \in N_{IJ}$.) are the averaged velocity response and coupling force over a small area Δs, respectively.

The total power transmitted across the interface $s^{(IJ)}$ is

$$q^t = \int_{s^{(IJ)}} q^{(I)}(\mathbf{x})ds = -\mathrm{Re}\left(\left\{\tilde{T}^{(I)}\right\}^T\right)\cdot\mathrm{Re}\left(\left\{\dot{\tilde{u}}^{(I)}\right\}\right) \tag{3.36}$$

with a time averaged value over a period of excitation of

$$\left\langle q^t\right\rangle = \frac{1}{T}\int_0^T q^t dt = -\frac{1}{2}\mathrm{Re}\left(\left\{\tilde{T}^{(I)}\right\}^T\left\{\dot{\tilde{u}}^{(I)}\right\}^*\right). \tag{3.37}$$

4. POWER FLOW ANALYSIS OF INDETERMINATE ROD/BEAM SYSTEMS

In this chapter, the power flow characteristics of two indeterminate vibrating systems consisting of three rods and eight beams, respectively, are examined. The first one is a segment of a rod-truss system, which is used widely in engineering. Usually, only compressive responses in the rod are considered in a static analysis and/or in the low modal density range analysis of the rod-truss system, but herein bending influence is also examined because there may be many bending modes in the frequency range under investigation. The second example consisting of eight beams also examines in both bending and compressive influences. A theoretical modal substructure approach is used to evaluate the vibration power flow characteristics of these systems. Hence, natural frequencies and mode shapes of the single rod/beam are first determined and then a receptance function or frequency response function is derived for the coupled system. This is achieved by introducing geometrical compatibility conditions which supplement the normal dynamic equations describing the vibrating characteristics in the indeterminate system. Both instantaneous and time-averaged power flows in the rod/beam systems are calculated and their characteristics discussed.

4.1. Theoretical Receptance Function of a Single Uniform Beam

The receptance analysis presented here is based on modal analysis. This implies that the natural frequencies and modal shapes of the substructure are first determined and then the receptance function or frequency response function of a single uniform beam derived from a theorem due to Rayleigh (1894).

Usually, three kinds of vibrations exist in a single beam. That is, axial, torsional and flexural bending vibrations. The receptance function of a uniform beam under all standard boundary conditions can be derived theoretically. If the beam vibrates in a plane, there is no torsional vibration component, but this must be considered when the system vibrates in three-dimensions, as arises for a beam coupled to a plate.

Here a substructure is treated as an idealised system consisting of a single uniform beam of length l (see, figure 4.1). This beam of uniform cross-section area A, moment of inertia I and polar second moment J is made of material of mass density ρ, elastic Young's modulus E, shear modulus G and its structural damping properties are represented by a linear Voigt viscoelastic model with hysteretic damping or loss factor η.

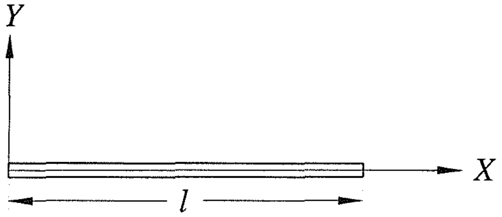

Figure 4.1. A uniform beam and its coordinate axis system.

It is assumed that the axial, torsional and transverse beading responses of the beam are uncoupled. This allows these vibrations to be determined independently.

4.1.1. Axial Vibration of a Uniform Beam

For axial extension vibration it is assumed that cross sections, which are initially plane and perpendicular to the axis X of the beam, remain plane and perpendicular to that axis and that the normal stress in the axial direction X is the only component of stress.

The free vibration equation describing the axial displacement $\tilde{u}_x(x,t)$ (see, for example, Meirovitch 1967 or Warburton 1976) is given in the form

$$-EA\frac{\partial^2\tilde{u}_x(x,t)}{\partial x^2}+\rho A\frac{\partial^2\tilde{u}_x(x,t)}{\partial t^2}=0 \tag{4.1}$$

with stress-displacement relation

$$\tilde{N}(x,t)=A\tilde{\sigma}_x(x,t)=EA\frac{\partial\tilde{u}_x(x,t)}{\partial x}. \tag{4.2}$$

For free vibration it is assumed that the displacement is a harmonic function of time, i.e.

$$\tilde{u}_x(x,t)=U_x(x)e^{\mathrm{i}(\omega t+\varphi)}. \tag{4.3}$$

The substitution of this equation into equation (4.1) gives the auxiliary equation for U_x in the form

$$\frac{E}{\rho}\frac{d^2U_x}{dx^2}+\omega^2U_x=0, \tag{4.4}$$

with solution

$$U_x=B_1\sin kx+B_2\cos kx. \tag{4.5}$$

The coefficients in equation (4.5) are determined by utilising the boundary conditions. When the beam is clamped at *x=0*, free at *x=l*, the natural frequencies ω_r and principal mode shapes φ_r are given by

$$\omega_r=\frac{(2r-1)\pi}{2l}\sqrt{\frac{E}{\rho}}, \tag{4.6}$$

$$\varphi_r=\sin\frac{(2r-1)\pi x}{2l}=\sin k_r x,\quad r=1,2,\ldots\ldots \tag{4.7}$$

When the beam is free at both ends, the natural frequencies ω_r and principal mode shapes φ_r are given by

$$\omega_r=\frac{r\pi}{l}\sqrt{\frac{E}{\rho}}, \tag{4.8}$$

$$\varphi_r=\cos\frac{r\pi x}{l}=\cos k_r x,\quad r=0,1,2,\ldots\ldots \tag{4.9}$$

It can be shown that these mode shapes are orthogonal (see, Appendix A), satisfying the condition

$$\int_0^l\varphi_r(x)\varphi_s(x)dx=0,\quad r\neq s, \tag{4.10}$$

for a uniform beam.

If an applied force $\tilde{f}_x(t)$ acts in the *X* direction at the free end of the beam at *x=l*, the equation of motion describing the axial displacement $\tilde{u}_x(x,t)$ is given in the form

$$-EA(1+\mathrm{i}\eta)\frac{\partial^2\tilde{u}_x(x,t)}{\partial x^2}+\rho A\frac{\partial^2\tilde{u}_x(x,t)}{\partial t^2}=\tilde{f}_x(t)\delta(l-x), \tag{4.11}$$

where $\delta(x)$ denotes the *Dirac* delta function.

When the assumed solution from Rayleigh's theorem (equation 3.10) is substituted into the equation of motion (4.11) and the resulting equation multiplied by $\varphi_s(x)$ prior to integrating with respect to x over the length of the beam, the equation describing the rth principal co-ordinate $\tilde{p}_r(t)$ is expressed as

$$\begin{aligned} A[E(1+i\eta)k_r^2\tilde{p}_r(t)+\rho\ddot{\tilde{p}}_r(t)]\int_0^l\varphi_r^2(x)dx &= \int_0^l\varphi_r(x)\tilde{f}_x(t)\delta(l-x)dx \\ &= \varphi_r(l)\tilde{f}_x(t) \end{aligned} \tag{4.12}$$

for $r = 1,2,3,\cdots\cdots,n$. If the applied force is harmonic and given by

$$\tilde{f}_x(t)=\tilde{F}_x e^{\mathrm{i}\omega t}=\left|\tilde{F}_x\right|e^{\mathrm{i}(\omega t+\varphi_F)}, \tag{4.13}$$

the principal co-ordinate is defined by the expression

$$\begin{aligned} \tilde{p}_r(t) &= \frac{\tilde{F}_x\varphi_r(l)}{A[-\rho\omega^2+E(1+\mathrm{i}\eta)k_r^2]\int_0^l\varphi_r^2(x)dx}e^{\mathrm{i}\omega t} \\ &= \frac{[(\omega_r^2-\omega^2)-\mathrm{i}\eta\omega_r^2]\tilde{F}_x\varphi_r(l)}{m_r[(\omega_r^2-\omega^2)^2+\eta^2\omega_r^4]}e^{\mathrm{i}\omega t}, \end{aligned} \tag{4.14}$$

where $m_r=\int_0^l\rho A\varphi_r^2(x)dx$ denotes the generalised modal mass of the beam. The substitution of equation (4.14) into equation (3.10) gives the axial displacement of the beam at position x, $0 \le x \le l$. That is

$$\tilde{u}_x(x,t)=\sum_{r=1}^{n}\frac{[(\omega_r^2-\omega^2)-\mathrm{i}\eta\omega_r^2]\varphi_r(x)\varphi_r(l)\tilde{F}_x}{m_r[(\omega_r^2-\omega^2)^2+\eta^2\omega_r^4]}e^{\mathrm{i}\omega t}, \tag{4.15}$$

together with the vibration velocity,

$$\begin{aligned} \tilde{v}(x,t)=\dot{\tilde{u}}_x(x,t) &= \sum_{r=1}^{n}\frac{\mathrm{i}\omega[(\omega_r^2-\omega^2)-\mathrm{i}\eta\omega_r^2]\varphi_r(x)\varphi_r(l)\tilde{F}_x}{m_r[(\omega_r^2-\omega^2)^2+\eta^2\omega_r^4]}e^{\mathrm{i}\omega t} \\ &= \sum_{r=1}^{n}\frac{\omega\varphi_r(x)\varphi_r(l)\tilde{F}_x}{m_r[(\omega_r^2-\omega^2)^2+\eta^2\omega_r^4]^{1/2}}e^{\mathrm{i}(\omega t+\varphi_u)} \end{aligned} \tag{4.16}$$

where

$$\varphi_u(x) = \tan^{-1}\left[\sum_{r=1}^{n} \frac{(\omega_r^2-\omega^2)\varphi_r(x)\varphi_r(l)}{m_r\left[(\omega_r^2-\omega^2)^2+\eta^2\omega_r^4\right]} \Bigg/ \sum_{r=1}^{n} \frac{\eta\omega_r^2\varphi_r(x)\varphi_r(l)}{m_r\left[(\omega_r^2-\omega^2)^2+\eta^2\omega_r^4\right]} \right]$$ is the phase angle between the velocity and axial applied force.

4.1.2. Torsional Vibration of a Uniform Beam

For torsional vibration, it is initially assumed that the cross section of the beam is circular. The cross sections of the beam initially perpendicular to the axis X remain plane and their radii remain straight during deformation. Then from elementary elasticity theory (Reismann & Pawlik 1980) the torque-twist relation is

$$\tilde{M}_x = GJ\frac{\partial \tilde{\theta}_x}{\partial x} \tag{4.17}$$

where $\tilde{M}_x$ is the torque at section x, $\tilde{\theta}_x$ is the angular rotation about the X axis. From consideration of the dynamic equilibrium, the free vibration equation describing the angular rotation (see, for example Warburton 1976) is given in the form

$$-C_2^2\frac{\partial^2\tilde{\theta}_x(x,t)}{\partial x^2} + \frac{\partial^2\tilde{\theta}_x(x,t)}{\partial t^2} = 0 \tag{4.18}$$

where $C_2 = \left(G/\rho\right)^{1/2}$ is the velocity of propagation of shear waves in the material.

Equation (4.18) has the same generic form as the axial extension differential equation (4.1), thus its natural frequencies are similar to those expressed in equations (4.6) and (4.8) with G replacing E. For example, for a beam free at both ends, the natural frequencies ω_r and principal mode shapes φ_r are given by

$$\omega_r = \frac{r\pi}{l}\sqrt{\frac{G}{\rho}}, \tag{4.19}$$

$$\varphi_r = \cos\frac{r\pi x}{l} = \cos k_r x, \quad r=0,1,2,\ldots\ldots \tag{4.20}$$

For a beam clamped at both ends, the natural frequencies ω_r and principal mode shapes φ_r are given by

$$\omega_r = \frac{r\pi}{l}\sqrt{\frac{G}{\rho}}, \tag{4.21}$$

$$\varphi_r = \sin\frac{r\pi x}{l} = \sin k_r x, \quad r=1,2,3,\ldots\ldots \tag{4.22}$$

For non-circular cross sections the torque-twist relation can be expressed as

$$\tilde{M}_x = \kappa GJ\frac{\partial\tilde{\theta}_x}{\partial x} \tag{4.23}$$

where κ denotes a numerical factor depending on the cross sectional dimensions. The only change in the analysis is that C_2 is refined as $C_2 = \left(\kappa G/\rho\right)^{1/2}$. Thus for non-circular sections the solution depends on the dimensions of the cross section. Timoshenko & Goodier (1970) give an extensive treatment of the torsion of non-circular rods and include data from which the factor κ can be determined.

The angular rotation response of the beam under an external torque $\tilde{M}$ at position x_e, $0 \le x_e \le l$ has a similar form to that expressed in equation (4.15). That is

$$\tilde{\theta}_x(x,t) = \sum_{r=1}^{n}\frac{[(\omega_r^2-\omega^2)-\mathrm{i}\eta\omega_r^2]\varphi_r(x)\varphi_r(x_e)\tilde{M}}{m_r[(\omega_r^2-\omega^2)^2+\eta^2\omega_r^4]}e^{\mathrm{i}\omega t}. \tag{4.24}$$

Here, the rth modal mass $m_r = \int_0^l \rho J\varphi_r^2(x)dx$.

4.1.3. Bending Vibration of a Uniform Beam

For transverse bending vibration, the beam is treated as a simple Euler-Bernoulli beam. It is assumed that planes which are normal to the beam axis X in the non deformed state remain plane in the deformed state and the vertical displacement of all points on any normal cross sectional plane is the same. The effect of rotary inertia and transverse shear deformation are neglected. A more sophisticated theory may be adopted e.g. assuming a Timoshenko beam, Vlasov beam, etc, which add complication to the analysis without contributing additional insights into the power flow mechanisms.

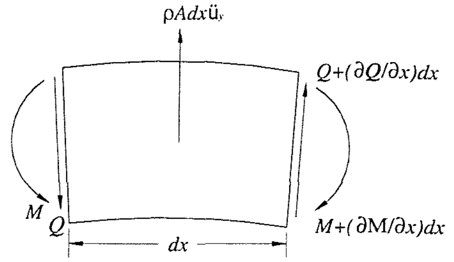

Figure 4.2. Element of beam in flexure.

As shown in figure 4.2, the free vibration equation describing the transverse displacement $\tilde{u}_y(x,t)$ (see, for example, Meirovitch 1967 or Warburton 1976) is given in the form

$$-EI\frac{\partial^4\tilde{u}_y(x,t)}{\partial x^4}+\rho A\frac{\partial^2\tilde{u}_y(x,t)}{\partial t^2}=0 \tag{4.25}$$

with stress-displacement relation

$$\tilde{Q}(x,t)=-EI\frac{\partial^3\tilde{u}_y(x,t)}{\partial x^3}, \tag{4.26}$$

$$\tilde{M}(x,t)=-EI\frac{\partial^2\tilde{u}_y(x,t)}{\partial x^2}, \tag{4.27}$$

where $\tilde{Q}(x,t)$ and $\tilde{M}(x,t)$ denote the shear force and bending moment at section x.

For free vibrations, $\tilde{u}_y(x,t)$ is a harmonic function of time, i.e.

$$\tilde{u}_y(x,t)=U_y(x)e^{\mathrm{i}(\omega t+\varphi)}, \tag{4.28}$$

and the substitution into equation (4.25), the auxiliary equation for U_y is given by

$$\frac{d^4U_y}{dx^4}-\frac{\rho A}{EI}\omega^2U_y=0, \tag{4.29}$$

with solution

$$U_y=B_1\sin kx+B_2\cos kx+B_3\sinh kx+B_4\cosh kx. \tag{4.30}$$

The coefficients in equation (4.30) are determined by utilising the boundary conditions. The standard end conditions are

(a) simply supported, for which the displacement and bending moment are zero, i.e.

$$U_y=0 \text{ and } {d^2U_y}\Big/{dx^2}=0; \tag{4.31}$$

(b) fixed or clamped, for which the displacement and slope are zero, i.e.

$$U_y=0 \text{ and } {dU_y}\Big/{dx}=0; \tag{4.32}$$

(c) free, for which the shear force and bending moment are zero, i.e.

$$ {d^2U_y}\Big/{dx^2}=0 \text{ and } {d^3U_y}\Big/{dx^3}=0. \tag{4.33}$$

Generally, the boundary conditions used in a free-free interface substructure approach are one end free, the other simply supported, fixed or free.

When the beam is clamped at $x=0$, free at $x=l$, the end conditions are:

At $x=0$, $U_y=0$, i.e. $B_2+B_4=0$. (4.34)

At $x=0$, ${dU_y}\Big/{dx}=0$, i.e. $B_1+B_3=0$. (4.35)

At $x=l$, ${d^2U_y}\Big/{dx^2}=0$, i.e. $k^2B_1(-\sin kl-\sinh kl)+k^2B_2(-\cos kl-\cosh kl)=0$. (4.36)

At $x=l$, ${d^3U_y}\Big/{dx^3}=0$, i.e. $k^3B_2(\sin kl-\sinh kl)+k^3B_1(-\cos kl-\cosh kl)=0$. (4.37)

Eliminating B_1/B_2, we derive the frequency equation

$$\cos kl \cosh kl+1=0. \tag{4.38}$$

The successive roots k_1, k_2, k_3, ... of equation (4.38), from which the natural frequencies are obtained, are given by

$k_1l\approx 1.875$, $k_2l\approx 4.694$, $k_3l\approx 7.855$, $k_rl\approx (r-0.5)\pi$ for $r\geq 4$; and

$$\omega_r=k_r^2\left({EI}\Big/{\rho A}\right)^{1/2}, \tag{4.39}$$

with its principal mode shapes

$$\varphi_r(x) = \cosh k_r x - \cos k_r x - \frac{\cos k_r l + \cosh k_r l}{\sin k_r l + \sinh k_r l}(\sinh k_r x - \sin k_r x), \quad r=1,2,\ldots \tag{4.40}$$

For a beam simply supported at $x=0$, free at $x=l$, the frequency equation is given by

$$\cos kl \sinh kl - \cosh kl \sin kl = 0, \tag{4.41}$$

with successive roots,

$$k_1 l = 0,\ k_2 l \approx 3.927,\ k_3 l \approx 7.069,\ k_r l \approx (r-0.75)\pi \text{ for } r \geq 4.$$

The natural frequencies have the same form as addressed by equation (4.39) and the principal mode shapes are given by

$$\varphi_r(x) = \begin{cases} x/l & r=1 \\ \sin k_r x + \dfrac{\sin k_r l}{\sinh k_r l}\sinh k_r x & r=2,3,4,\ldots \end{cases} \tag{4.42}$$

For a beam free at both ends, the frequency equation is given by

$$\cos kl \cosh kl = 1, \tag{4.43}$$

with successive roots,

$$k_1 l = 0,\ k_2 l = 0,\ k_3 l \approx 4.730,\ k_4 l \approx 7.853,\ k_5 l \approx 10.996,\ k_r l \approx (r-1.5)\pi \text{ for } r \geq 6.$$

The natural frequencies have the same form as expressed in equation (4.39) and the principal mode shapes are given by

$$\varphi_r(x) = \begin{cases} 1 & r=1 \\ 1-2x/l & r=2 \\ \cos k_r x + \cosh k_r x + \dfrac{\sinh k_r l + \sin k_r l}{\cosh k_r l - \cos k_r l}(\sin k_r x + \sinh k_r x), & r=3,4,5,\ldots \end{cases} \tag{4.44}$$

The orthogonality condition of mode shapes is

$$\int_0^l \varphi_r(x)\varphi_s(x)dx = 0, \quad r \neq s, \tag{4.45}$$

for a uniform beam.

If a harmonic distributed applied force $\tilde{f}_y(x)e^{i\omega t}$ acts in the Y direction along the length of the beam and a harmonic concentrated force $\tilde{Q}e^{i\omega t}$ as well as a moment $\tilde{M}e^{i\omega t}$

act at the free end of the beam $x=l$, the equation of motion describing the transverse displacement $\tilde{u}_y(x,t)$ is given in the form

$$-EI(1+\mathrm{i}\eta)\frac{\partial^4\tilde{u}_y(x,t)}{\partial x^4}+\rho A\frac{\partial^2\tilde{u}_y(x,t)}{\partial t^2}=\left(\tilde{f}_y(x)+\tilde{Q}\delta(l-x)-\frac{d\left(\tilde{M}\delta(l-x)\right)}{dx}\right)e^{\mathrm{i}\omega t}. \quad (4.46)$$

When the assumed solution from Rayleigh's theorem (equation 3.10) is substituted into the equation of motion (4.46) and the resulting equation multiplied by $\varphi_s(x)$ prior to integrating with respect to x over the length of the beam, the equation describing the rth principal co-ordinate $\tilde{p}_r(t)$ is expressed as

$$\begin{aligned}&\left[EI(1+\mathrm{i}\eta)k_r^4\tilde{p}_r(t)-\rho A\omega^2\tilde{p}_r(t)\right]\int_0^l\varphi_r^2(x)dx=\\&\left(\int_0^l\varphi_r(x)\tilde{f}_y(x)dx+\int_0^l\varphi_r(x)\tilde{Q}\delta(l-x)dx-\int_0^l\varphi_r(x)\frac{d\left(\tilde{M}\delta(l-x)\right)}{dx}dx\right)e^{\mathrm{i}\omega t}\end{aligned} \quad (4.47)$$

for $r=1,2,3,\cdots\cdots,n$.

Since (see, for example, Riley, *et al* 1998)

$$\int_0^l\tilde{Q}\delta(l-x)\varphi_r(x)dx=\tilde{Q}\varphi_r(l), \quad (4.48)$$

$$\begin{aligned}\int_0^l\varphi_r(x)\frac{d\left(\tilde{M}\delta(l-x)\right)}{dx}dx&=\int_0^l\frac{d\left(\tilde{M}\delta(l-x)\varphi_r(x)\right)}{dx}dx-\int_0^l\tilde{M}\delta(l-x)\frac{d\left(\varphi_r(x)\right)}{dx}dx\\&=\tilde{M}\left.\frac{d\varphi_r(x)}{dx}\right|_{x=l}=\tilde{M}\varphi_r'(l),\end{aligned} \quad (4.49)$$

the principal coordinate is defined by the expression

$$\tilde{p}_r(t)=\frac{\left[(\omega_r^2-\omega^2)-\mathrm{i}\eta\omega_r^2\right]\left(\int_0^l\tilde{f}_y(x)\varphi_r(x)dx+\tilde{Q}\varphi_r(l)+\tilde{M}\varphi_r'(l)\right)}{m_r[(\omega_r^2-\omega^2)^2+\eta^2\omega_r^4]}e^{\mathrm{i}\omega t}, \quad (4.50)$$

where $m_r=\int_0^l\rho A\varphi_r^2(x)dx$. The substitution of equation (4.50) into equation (3.10) gives the transverse displacement of the beam at position x, $0\le x\le l$. That is

$$\tilde{u}_y(x,t)=\sum_{r=1}^{n}\frac{\left[(\omega_r^2-\omega^2)-\mathrm{i}\eta\omega_r^2\right]\left(\int_0^l\tilde{f}_y(x)\varphi_r(x)dx+\tilde{Q}\varphi_r(l)+\tilde{M}\varphi_r'(l)\right)\varphi_r(x)}{m_r[(\omega_r^2-\omega^2)^2+\eta^2\omega_r^4]}e^{\mathrm{i}\omega t}, \quad (4.51)$$

together with the vibration velocity,

$$\begin{aligned}\dot{\tilde{u}}_y(x,t) &= \sum_{r=1}^{n} \frac{\omega\left[\mathrm{i}(\omega_r^2-\omega^2)+\eta\omega_r^2\right]\left(\int_0^l \tilde{f}_y(x)\varphi_r(x)dx + \tilde{Q}\varphi_r(l) + \tilde{M}\varphi_r'(l)\right)\varphi_r(x)}{m_r[(\omega_r^2-\omega^2)^2+\eta^2\omega_r^4]} e^{\mathrm{i}\omega t} . \\ &= \tilde{v}(x,t)\end{aligned}$$

(4.52)

These solutions are the receptance functions and have form similar to equation (3.19).

4.2. Power Flow Characteristics of a Single Uniform Beam

After accounting for the different ways power flows through the rod and equation (3.35), the instantaneous power flow in the rod at section x is given by:

$$q(x,t) = -\mathrm{Re}\{\dot{\tilde{u}}_x(x,t)\}\mathrm{Re}\{\tilde{N}(x,t)\} - \mathrm{Re}\{\dot{\tilde{u}}_y(x,t)\}\mathrm{Re}\{\tilde{Q}(x,t)\} + \mathrm{Re}\{\dot{\tilde{\theta}}(x,t)\}\mathrm{Re}\{\tilde{M}(x,t)\},$$

(4.53)

where $\tilde{N}(x,t)$, $\tilde{Q}(x,t)$, $\tilde{M}(x,t)$ denote the axial force, transverse shear force and bending moment respectively. The sign of the third term on the right hand side of equations (4.53) is dependent on the directions of $\tilde{M}$ and $\dot{\tilde{\theta}}$ based on the sign convention of elasticity theory (see, for example, Reismann & Pawlik 1980).

The time-averaged value of power flow over a period of excitation T at position x is given by

$$\langle q(x,t)\rangle = \frac{1}{T}\int_0^T q(x,t)dt. \qquad (4.54)$$

It is easy to obtain from basic beam theory all the parameters in equation (4.53) and those in equations (4.16), (4.52) respectively. The definition of power flow given by Goyder & White (1980) or Cremer *et al* (1988, Chapter 4, equation 129), i.e. $P = \frac{1}{2}\mathrm{Re}\{\tilde{f}(x,t)\tilde{v}^*(x,t)\}$, where $\tilde{v}^*(x,t)$ is the conjugate of the velocity, is the time-averaged power flow of equation (4.53), and hence, is equivalent to equation (4.54).

For illustrative purposes and to simplify analysis only, a one end free another end fixed steel rod of mass m=3120 kg, with properties $\eta = 0.015$, E/ρ=2.69×10^7 m^2/s^2, length l=10 m, section area A=0.04 is examined under a unit amplitude excitation in the axial direction at the end of the beam. That is, transverse bending is not considered in this example such that the instantaneous power flow in the rod simplifies to

$$\begin{aligned} q(x,t) &= -\mathrm{Re}\left\{\dot{\tilde{u}}_x(x,t)\right\}\mathrm{Re}\left\{\tilde{N}(x,t)\right\} \\ &= -U(x)\overline{T}(x)\cos(\varphi_u(x)-\varphi_T(x))\cos^2(\omega t+\varphi_T(x)), \\ &+\frac{1}{2}U(x)\overline{T}(x)\sin(\varphi_u(x)-\varphi_T(x))\sin 2(\omega t+\varphi_T(x)) \end{aligned} \tag{4.55}$$

where $U(x)$ and $\overline{T}(x)$ are the amplitude distributions of axial velocity and traction force respectively, $\varphi_T(x)$ is the phase angle between the traction force and axial exciting force. This equation is similar in form to the instantaneous sound intensity derived by Fahy (1989) and has two components: (i) an active component, of which the time averaged value is non-zero, corresponding to local transport of the energy; and (ii) a reactive component, of which the time averaged value is zero, corresponding to local oscillatory transport of energy, that is, the local transport between kinetic and potential energy.

Figures 4.3 and 4.4 illustrate the magnitudes of response velocity, traction force and power flow distributed along the rod at frequencies of 200 Hz and 388.9 Hz. The frequency 388.9Hz corresponds to the resonance frequency of the second natural mode of the rod. In this case, the magnitude of input power and time averaged input power induced by the unit amplitude excitation have the same value of 8.74×10^{-6}w. The frequency 200 Hz corresponds to a non-resonance condition, its magnitude of input power and time averaged input power induced by the unit amplitude excitation have values of 2.71×10^{-7} w and 8.59×10^{-9} w respectively.

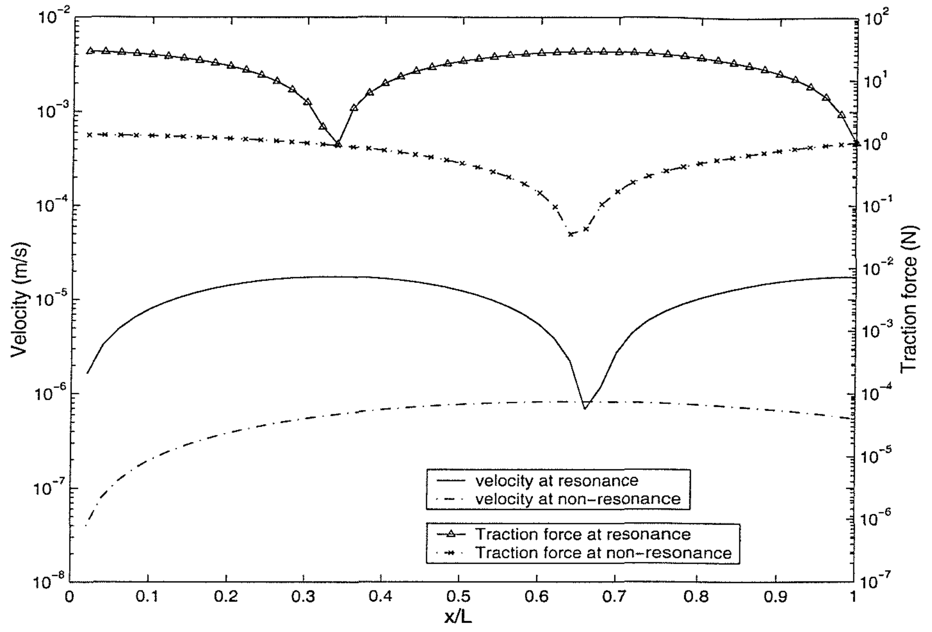

Figure 4.3. Distribution of the magnitudes of velocity and traction force.

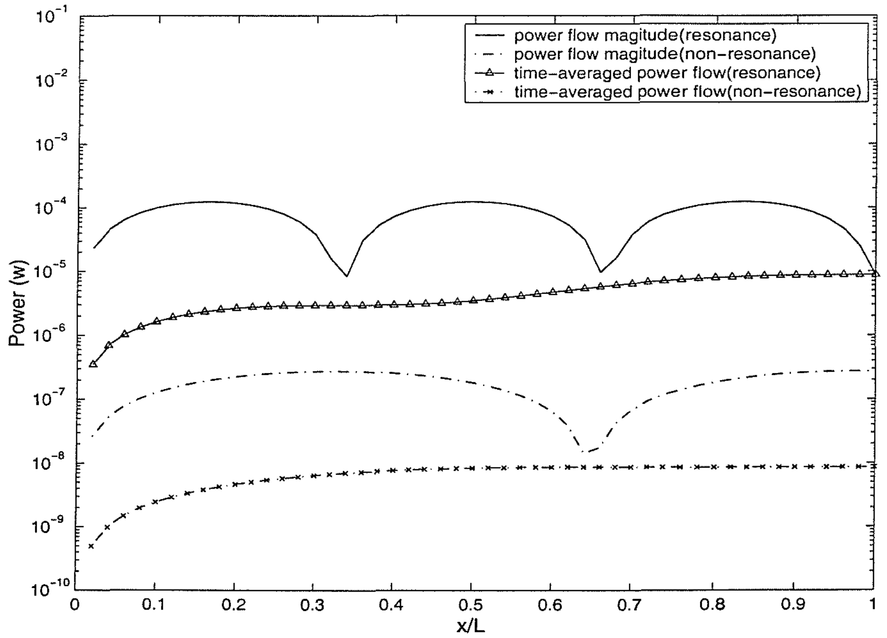

Figure 4.4. Distribution of power flow along the rod.

As shown in figure 4.3, at the resonance frequency of 328.9Hz, the response velocity and traction force along the rod experience minimum values at different position, thus creating two troughs in the power flow distribution curve as shown in figure 4.4. At a non-resonance frequency of 200 Hz, only the traction force exhibits a minimum value producing only a single power flow trough at exactly the same position on the rod. The magnitude of instantaneous power flow at any point along the rod (i.e., $0< x< l$) may be larger than the magnitude of instantaneous input power of the exciting force at $x=l$ due to the influence of resonance. The reactive power along the rod in equation (4.55) has different phase angles and the reactive power at some points may be opposite to those observed at other points. This means some points of the rod store energy whereas other points release energy. Whilst the rate of energy transfer between kinetic and potential energy at some sections of the rod is larger than the input power, the magnitude of instantaneous power flow at these sections is larger than the magnitude of instantaneous input power of the exciting force. The distribution curve of the time averaged power flow does not exhibit troughs along the rod in both resonant and non-resonant conditions as shown in figure 4.4. The time averaged power flow values always increase with increasing x along the rod. This is due to the fact that in any period, the time-averaged power flow value in any section x is equal to the rate of total energy dissipation of the rod from sections 0 to section x.

4.3. Application to a Three-beam Indeterminate System

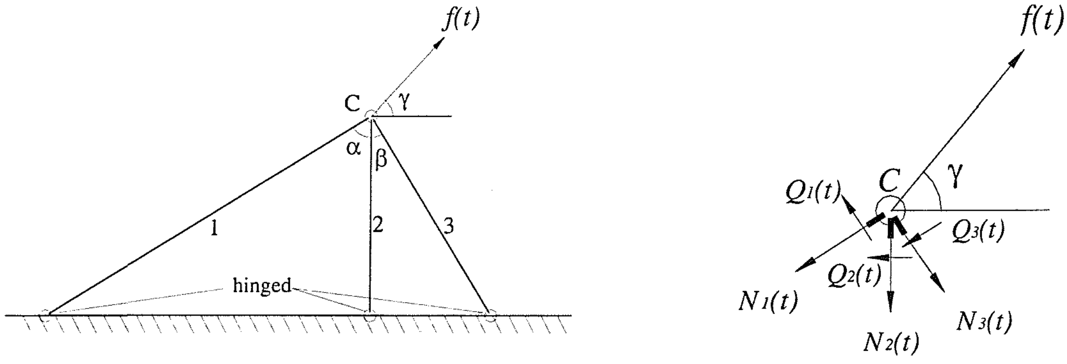

Figure 4.5. A three-beam indeterminate system

Figure 4.5 illustrates the three-beam system under examination. It is assumed that each uniform beam is constructed of the same material (i.e. same Young's modulus E and structural damping loss factor η) but of different lengths $l_j\,(j=1,2,3)$, moments of the inertia I_j, cross-sectional areas A_j and masses $m_j=\rho l_j A_j$. Each rod is hinged at its base (see also figure 4.5) and connected at their ends at C where an external exciting force $f(t)=Fe^{i\omega t}$ acts causing axial traction forces $\tilde{N}_j(t)$ and transverse shear forces $\tilde{Q}_j(t)$ at C.

Because of structural damping, the axial traction force and transverse shear force in each rod at C is expressed in the complex valued form

$$\begin{aligned}\tilde{N}_j(t)&=N_j e^{\mathrm{i}(\omega t+\varphi_{N_j})}\\ \tilde{Q}_j(t)&=Q_j e^{\mathrm{i}(\omega t+\varphi_{Q_j})}\end{aligned}, \tag{4.56}$$

where φ_{N_j}, φ_{Q_j} denote the phase angles between the external force $f(t)$ and axial traction force $\tilde{N}_j(t)$, the external force $f(t)$ and transverse shear force $\tilde{Q}_j(t)$ of the rod j, for $j=1,2,3$, respectively.

For the simplified indeterminate system under examination, the force balance equation at C is given by

$$\begin{aligned}\tilde{N}_1(t)\sin\alpha+\tilde{Q}_1(t)\cos\alpha+\tilde{Q}_2(t)-\tilde{N}_3(t)\sin\beta+\tilde{Q}_3(t)\cos\beta&=f(t)\cos\gamma,\\ \tilde{N}_1(t)\cos\alpha-\tilde{Q}_1(t)\sin\alpha+\tilde{N}_2(t)+\tilde{N}_3(t)\cos\beta+\tilde{Q}_3(t)\sin\beta&=f(t)\sin\gamma,\end{aligned} \tag{4.57}$$

where the angles are defined in figure 4.5. For solution, this set of equations must be supplemented by a geometrical compatibility equation. That is, the distortions or velocities at point C of the three rods are the same in all directions, thus providing the conditions

$$\begin{aligned}&\dot{\tilde{u}}_{x1}(t)\sin\alpha+\dot{\tilde{u}}_{y1}(t)\cos\alpha-\dot{\tilde{u}}_{y2}(t)=0\\ &\dot{\tilde{u}}_{x1}(t)\cos\alpha-\dot{\tilde{u}}_{y1}(t)\sin\alpha-\dot{\tilde{u}}_{x2}(t)=0\\ &-\dot{\tilde{u}}_{x3}(t)\sin\beta+\dot{\tilde{u}}_{y3}(t)\cos\beta-\dot{\tilde{u}}_{y2}(t)=0\\ &\dot{\tilde{u}}_{x3}(t)\cos\beta+\dot{\tilde{u}}_{y3}(t)\sin\beta-\dot{\tilde{u}}_{x2}(t)=0\end{aligned}, \tag{4.58}$$

where $\dot{\tilde{u}}_{xj}(t)$, $\dot{\tilde{u}}_{yj}(t)$ denote the axial and transverse velocities, respectively, at point C of the rod j.

It follows from equations (4.16), (4.52) that the axial and transverse velocities at C in each rod of this *indeterminate system* can be expressed in the form

$$\dot{\tilde{u}}_{xj}(t) = \tilde{N}_j(t) U_{xj} e^{i\varphi_{u_{xj}}} , \tag{4.59}$$

$$\dot{\tilde{u}}_{yj}(t) = \tilde{Q}_j(t) U_{yj} e^{i\varphi_{u_{yj}}} , \tag{4.60}$$

where U_{xj}, $\varphi_{u_{xj}}$ are the amplitude of axial velocity and the phase angle between axial velocity $\dot{u}_{xj}(t)$ and traction force $\tilde{N}_j(t)$ at C of the jth beam respectively, U_{yj}, $\varphi_{u_{yj}}$ are the amplitude of transverse velocity and the phase angle between transverse velocity $\dot{u}_{yj}(t)$ and shear force $\tilde{Q}_j(t)$ at C of the jth beam respectively, for $j=1, 2, 3$.

The information contained within the force balance equation (4.57), the geometrical compatible equation (4.58) and the receptance functions (4.59), (4.60) allow the traction forces $\tilde{N}_j(t)$ and shear forces $\tilde{Q}_j(t)$ in each rod C to be determined.

The real input power to each rod at connection point C is given by

$$q_j(t) = \mathrm{Re}\{\dot{\tilde{u}}_{xj}(t)\}\mathrm{Re}\{\tilde{N}_j(t)\} + \mathrm{Re}\{\dot{\tilde{u}}_{yj}(t)\}\mathrm{Re}\{\tilde{Q}_j(t)\}. \tag{4.61}$$

The substitution of equations (4.59) and (4.60) into the previous equation gives

$$\begin{aligned} q_j(t) &= \mathrm{Re}\left\{U_{xj}\cdot N_j e^{i(\omega t+\varphi_{N_j}+\varphi_{u_{xj}})}\right\}\mathrm{Re}\left\{N_j e^{i(\omega t+\varphi_{N_j})}\right\} \\ &\quad + \mathrm{Re}\left\{U_{yj}\cdot Q_j e^{i(\omega t+\varphi_{Q_j}+\varphi_{u_{yj}})}\right\}\mathrm{Re}\left\{Q_j e^{i(\omega t+\varphi_{Q_j})}\right\} \\ &= \frac{1}{2}U_{xj}N_j^2\left[\cos\varphi_{u_{xj}} + \cos(2\omega t + 2\varphi_{N_j} + \varphi_{u_{xj}})\right] + \frac{1}{2}U_{yj}N_j^2\left[\cos\varphi_{u_{yj}} + \cos(2\omega t + 2\varphi_{Q_j} + \varphi_{u_{yj}})\right] \\ &= \frac{1}{2}\left(U_{xj}N_j^2\cos\varphi_{u_{xj}} + U_{yj}Q_j^2\cos\varphi_{u_{yj}}\right) + C_j\cos(2\omega t + \varphi_j) \end{aligned} \tag{4.62}$$

and its time averaged value over a period T of excitation is

$$\langle q_j(t)\rangle = \frac{1}{T}\int_0^T q_j(t)dt = \frac{1}{2}U_{xj}N_j^2\cos\varphi_{u_{xj}} + \frac{1}{2}U_{yj}Q_j^2\cos\varphi_{u_{yj}}, \tag{4.63}$$

where

$$\varphi_j = \cos^{-1}\left[\frac{U_{xj}N_j^2\cos(2\varphi_{N_j}+\varphi_{u_{xj}})+U_{yj}Q_j^2\cos(2\varphi_{N_j}+\varphi_{u_{yj}})}{C_j}\right],$$

$$C_j = \frac{1}{2}\left[\left(U_{xj}N_j^2\cos(2\varphi_{N_j}+\varphi_{u_{xj}})+U_{yj}Q_j^2\cos(2\varphi_{Q_j}+\varphi_{u_{yj}})\right)^2\right.$$

$$\left.+\left(U_{xj}N_j^2\sin(2\varphi_{N_j}+\varphi_{u_{xj}})+U_{yj}Q_j^2\sin(2\varphi_{Q_j}+\varphi_{u_{yj}})\right)^2\right]^{1/2}.$$

The combination of these last two equations gives

$$q_j(t) = \langle q_j(t)\rangle + \langle q_j(t)\rangle\frac{\cos(2\omega t+\varphi_j)}{\cos\varphi_j}, \tag{4.64}$$

indicating that the power flow in each rod contains a component equal to its time averaged power flow value and hence constant in time but varying with frequency of excitation. Because of the influence of structural damping, $\cos\varphi_j > 0$, since $\varphi_j \neq 90^\circ$ and this component reduces in value as $\eta \to 0$. The dynamic component has an oscillatory behaviour of double the frequency of excitation. The instantaneous power flow $q_j(t)$ expressed in equation (4.62) or (4.64) is similar in form to the instantaneous sound intensity component derived by Fahy (1989) and Bobrovnitskii (1999). It contains two components: an active component, with a non-zero time averaged value, corresponding to local transport of the energy and a reactive component, with a zero time averaged value, corresponding to local oscillatory transport of energy.

Similarly, the input power at C due to the external exciting force is given by

$$q_{in}(t) = \mathrm{Re}\{\dot{u}_c(t)\}\mathrm{Re}\{f(t)\}, \tag{4.65}$$

with a corresponding averaged quantity $\langle q_{in}(t)\rangle$, where $\dot{u}_c(t)$ is the velocity along the direction of exciting force $f(t)$ at point C. From the geometrical compatibility condition, the input power at C due to the external exciting force becomes

$$q_{in}(t) = \mathrm{Re}\{\dot{u}_{x2}(t)\}\mathrm{Re}\{f(t)\}\sin\gamma + \mathrm{Re}\{\dot{u}_{y2}(t)\}\mathrm{Re}\{f(t)\}\cos\gamma, \tag{4.66}$$

with the corresponding time averaged quantity $\langle q_{in}(t)\rangle$.

It is interesting to note that expressions for the power flow balance condition at C

may be obtained by multiplying the geometric compatible equations by the velocity at *C*. Unfortunately, in this form these balance equations are difficult to handle in terms of deriving solutions of power flows. The basic power flow balance equation from the geometric compatible equation at *C* is given by

$$q_{in}(t) = q_1(t) + q_2(t) + q_3(t), \tag{4.67}$$

with time averaged quantity,

$$\langle q_{in}(t) \rangle = \langle q_1(t) \rangle + \langle q_2(t) \rangle + \langle q_3(t) \rangle. \tag{4.68}$$

Let us assume that the indeterminate system is defined by the data set:

$l_1 = 10\,m,\ l_2 = 5\,m,\ l_3 = 5.7735\ m,\ A_1 = 0.04m^2 = A_2 = A_3,$
$I_1 = I_2 = I_3 = 1.333\times10^{-4}\,m^4;$

$\rho = 7.8\ g\,cm^{-3}$, E=$2.1\times10^{11}Nm^{-2}$, $\eta = 0.015$; $\alpha = 60°$, $\beta = 30°$, F=1.0 N.

The largest natural frequency for the substructure modal analysis of both compressive and bending vibration in each rod is chosen to be greater than ten times of the maximum frequency used in calculation.

In the following presentation of predictions of power flow variation with frequency or time, figures 4.7-4.11 relate to condition $\gamma = 45°$ (see figure 4.5). Figure 4.7 illustrates the variation of the amplitude of power flow with frequency ω and non-dimensional frequency Ω ($\Omega = \frac{\omega l_1}{\pi}\sqrt{\rho/E}$) in each beam at *C* (i.e. equation 4.62) and the excitation power flow given by equation (4.65). Figure 4.8 shows their time average quantities, i.e. $\langle q_j(t) \rangle$ and $\langle q_{in}(t) \rangle$. Figures 4.9 and 4.10 present the same information in terms of $\frac{1}{3}\,Oct$ value. Figure 4.11 illustrates the time variation of the power flow quantities under investigation at an exciting frequency $f_n = 375\,Hz$. Figures 4.12-4.15 show a selection of power flow results for $\gamma = 0°$, $45°$, $90°$ and $135°$, allowing comparison with figure 4.9 to evaluate the effect of angle of application of the external excitation on the dynamic characteristics of the indeterminate system.

Although the instantaneous excitation input power $q_{in}(t)$ is equal to the sum of the three input powers of each rod, as observed in equation (4.67) and figure 4.11, its value is not necessarily larger than the individual quantities. This is due to the influence of resonance and the manner in which energy is transferred within the overall system. For example, the amplitude $q_1(t)$ is much larger than the amplitudes of $q_3(t)$ or $q_{in}(t)$ but at any instant their phasing is such that the energy in the total system remains in balance.

In contrast, as shown in figures 4.8 and 4.10, the time averaged excitation power $\langle q_{in}(t)\rangle$ is always greater in value than the other time averaged quantities. This is due to the fact that in any period, the time-averaged power of excitation is equal to the rate of total energy dissipation of the system, (see, for example, Lyon 1975, Fahy 1994 and Xing & Price 1999) and is equal to the sum of the energy dissipations in each rod, (see equation 4.68). As demonstrated in equation (4.63), each time averaged quantity $\langle q_j(t)\rangle$ contains a constant component contribution to the overall dynamics of the system, depending on both the amplitude of the instantaneous input power and the phase angle between the velocity response and the traction and shear forces. Their peak values occur at resonance because both values of amplitude of power and $\cos\varphi_{u_{xj}}$ *or* $\cos\varphi_{u_{yj}}$ are largest.

In the low frequency band range, figures 4.9 and 4.10 show both the instantaneous power and time-averaged power influenced by resonance but this diminishes with increasing frequency values. For frequencies greater than 1.25kHz, both instantaneous and time-averaged input powers expressed in the 1/3 Oct scale range are stable in form. This is due to the presence of more modes and an increased influence of damping in the higher frequency band range, indicating that SEA is an appropriate analysis tool over 1.25 kHz.

For the indeterminate system under examination, input power depends on the excitation, dynamic and geometrical characteristics of the structures. It can be seen clearly from the selected results shown in figures 4.12-4.15 that the input power of excitation and the power flow in each rod is related to the angle of excitation (figure 4.5).

For illustrative and comparison purposes, figures 4.16-4.19 relate to condition $\gamma = 45°$ (see figure 4.5) and show a set of results including and excluding bending influences. That is, in the latter case, only the compressive response of the rod is considered. Figures 4.16 and 4.17 illustrate the variation of the amplitude of power flow with $\frac{1}{3}\,Oct$ in each rod at C and the excitation power. Figures 4.18 and 4.19 show their time averaged quantities.

Although there are many bending modes in the rod truss system, the amplitudes of instantaneous and time-averaged power flow in each rod at C and the excitation power flow have similar levels of magnitude in the middle and high frequency ranges for both conditions examined. There are obvious resonant bending mode influences below and near the first natural frequency (about 120 Hz) of compressive vibration of rod 1. These resonant influences in a time-averaged power flow analysis become larger and more noticeable because time-averaged power depends on both values of amplitude of power and $\cos\varphi_{u_{xj}}$ or $\cos\varphi_{u_{yj}}$ (see, equation 4.63) with $\cos\varphi_{u_{yj}}$ largest in the bending resonant condition.

4.4. Application to a Eight-beam Frame System

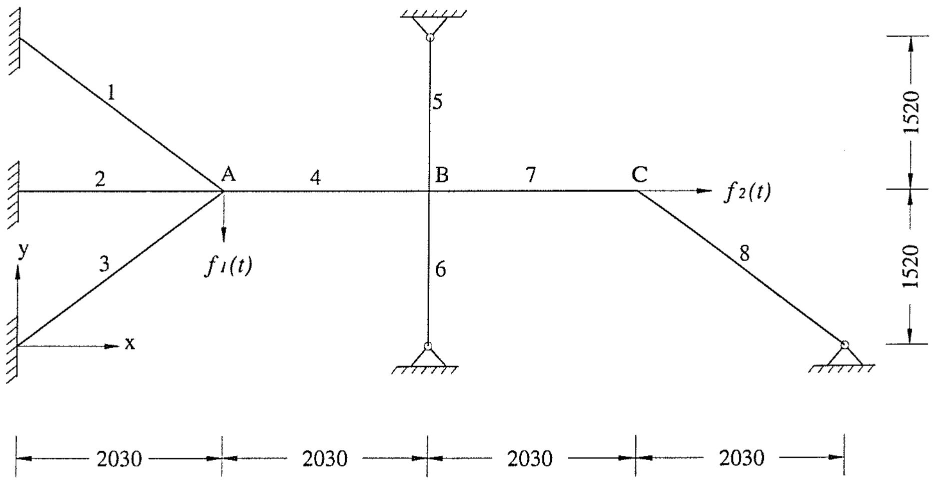

Figure 4.6. A beam frame with eight members of lengths measured in *mm* (Beale & Accorsi 1995).

The second example shown in figure 4.6 is a more complex beam system constructed using eight beam members. Their material and geometric properties are as follows: E=207 GPa, $\rho = 7860\,kg/m^3$, $\eta = 0.01$; section area of beams (1), (3), (5), (6), (7)=203×203 $(\mathrm{mm})^2$, section area of beams (2), (4), (8) =152×152 $(\mathrm{mm})^2$. The frame is loaded at junctions *A* and *C* by harmonic forces $f_1(t)=22.25e^{i\omega t}N$ and $f_2(t)=44.5e^{i\omega t}N$ respectively. This system was originally examined by Beale & Accorsi (1995) to assess its dynamic characteristics adopting a travelling wave model.

Similar to the calculations described in example 1, a modal substructure approach is again used to calculate the power flow utilising the force (moment) balance equations and geometrical compatibility equations at junctions *A*, *B* and *C*. The substructure boundary conditions used here are one end fixed, one end free for beams (1), (2), (3), two free ends for beams (4), (7) and one end simply supported, one end free for beams (5), (6), (8). The expressions describing power flow at a junction are similar to those given in equations (4.66), (4.67) and (4.68). The power flow at a junction is zero (for example, junction *B*) if there is no applied external excitation force at this position because of the balance between internal forces and continuous displacements.

Figures 4.20-4.22 illustrate the variation of the amplitude of power flow with frequency at junctions *A* and *C*. The calculated time averaged power flow values at junctions *A* and *C* demonstrate the same trends as those presented by Beale & Accorsi (1995). From figure 4.22, it is observed that the time averaged power flow at junction *A* produces negative values at several exciting frequencies implying that the direction of the exciting force $f_1(t)$ and the velocity are opposite to one another. This means that the exciting force source $f_1(t)$ at junction *A* absorbs power from the system and it behaves as an active control source at these frequencies.

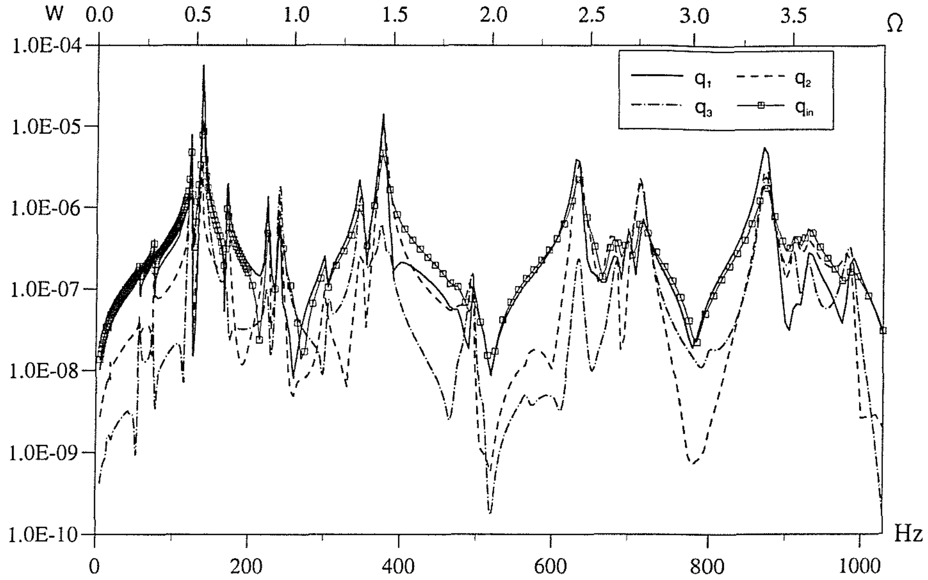

Figure 4.7. The variation with frequency of the amplitudes of the input power flows in the three rods q_j, $j=1, 2\ 3$ and excitation q_{in}.

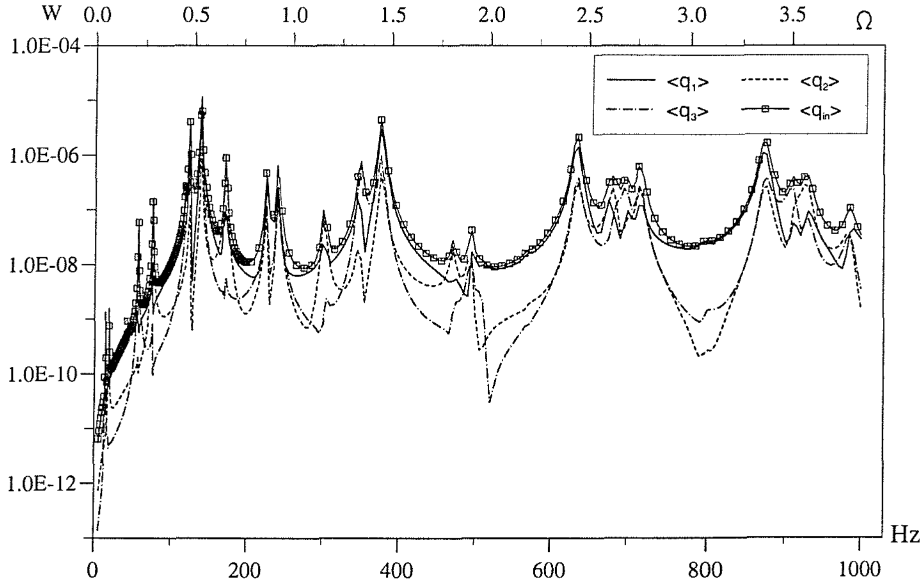

Figure 4.8. The variation with frequency of the amplitudes of the time averaged input power flows in the three rods $\langle q_j(t)\rangle$ and excitation $\langle q_{in}(t)\rangle$.

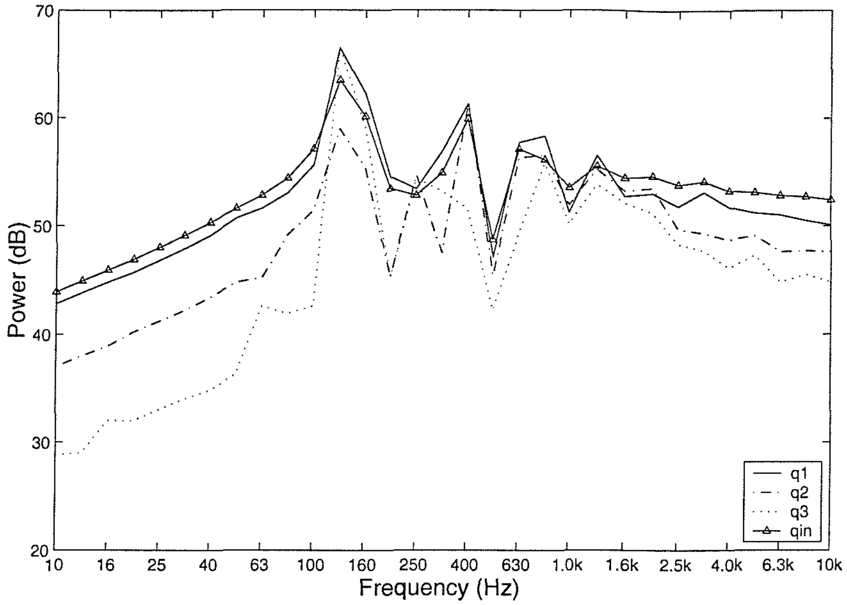

Figure 4.9. The corresponding information to figure 4.7 expressed in a 1/3 Oct scale (Ref. power 10^{-12} W).

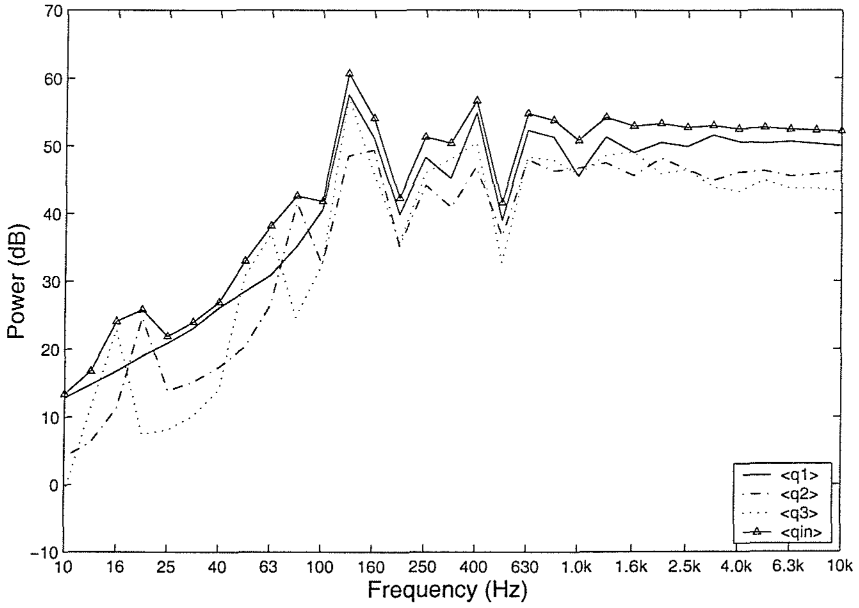

Figure 4.10. The corresponding information to figure 4.8 expressed in a 1/3 Oct scale.

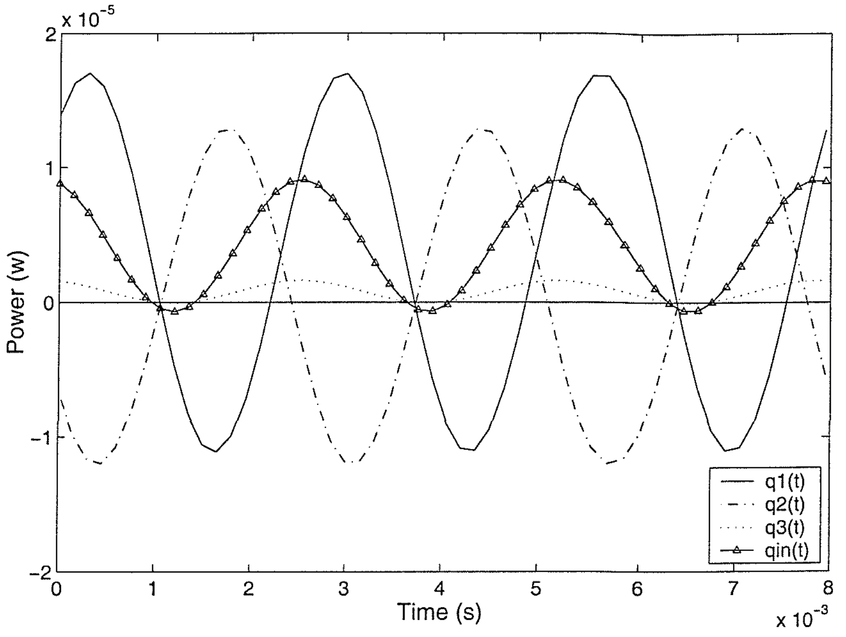

Figure 4.11. The variation with time of the input power flows in the three rods and the excitation at an exciting frequency of 375 Hz and angle of application of force, $\gamma = 45^{\circ}$ (see, figure 4.5).

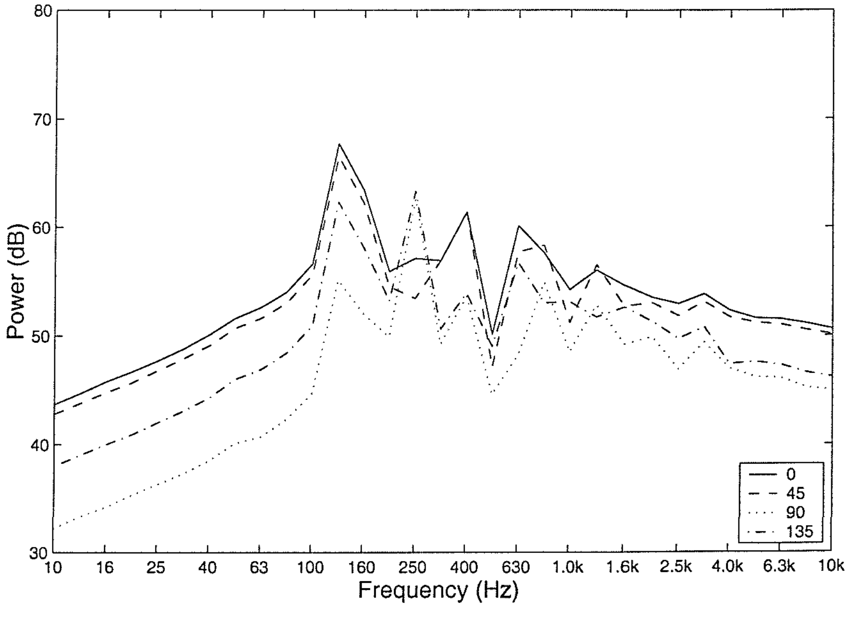

Figure 4.12. The variation with frequency of the amplitudes of the input power flow to rod 1 (see, figure 4.5) expressed in a 1/3 Oct scale for different angles of application of force γ.

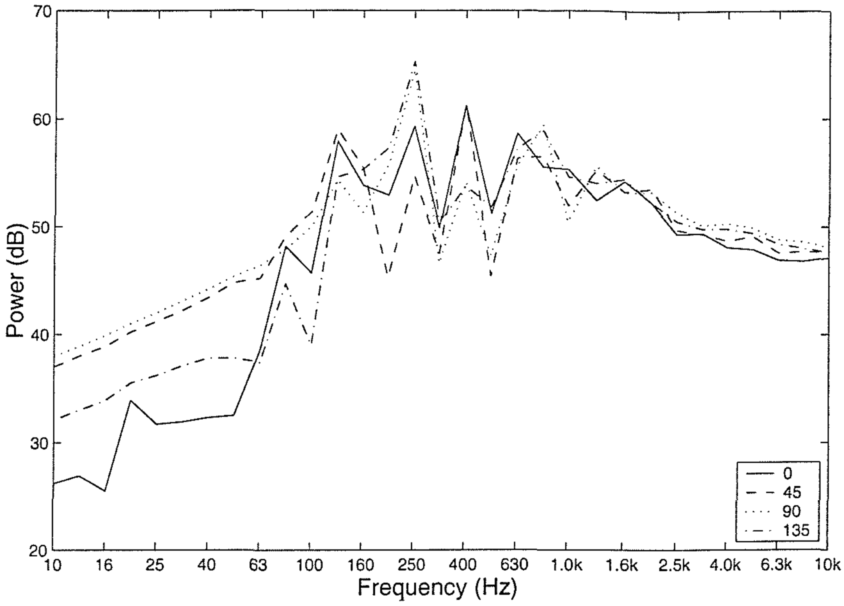

Figure 4.13. The variation with frequency of the amplitudes of the input power flow to rod 2 (see, figure 4.5) expressed in a 1/3 Oct scale for different angles of application of force γ.

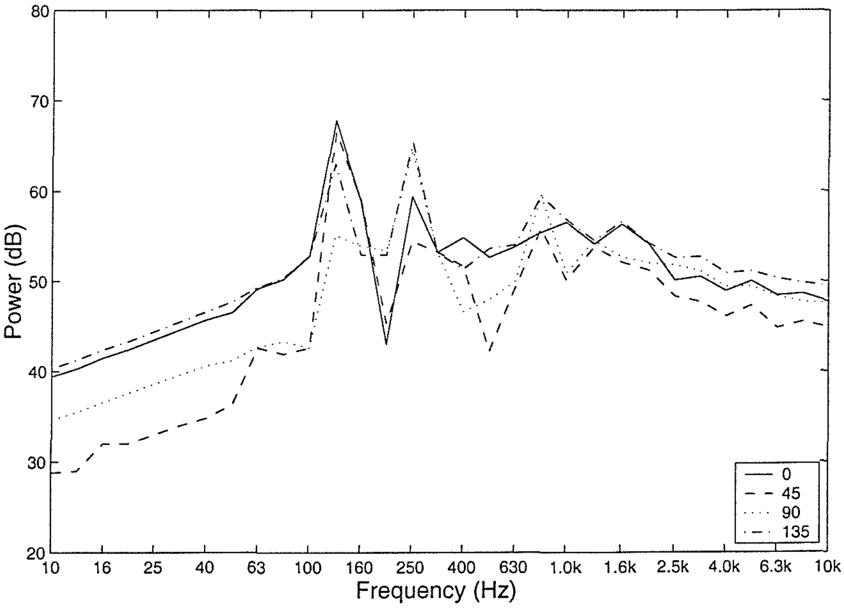

Figure 4.14. The variation with frequency of the amplitudes of the input power flow to rod 3 (see, figure 4.5) expressed in a 1/3 Oct scale for different angles of application of force γ.

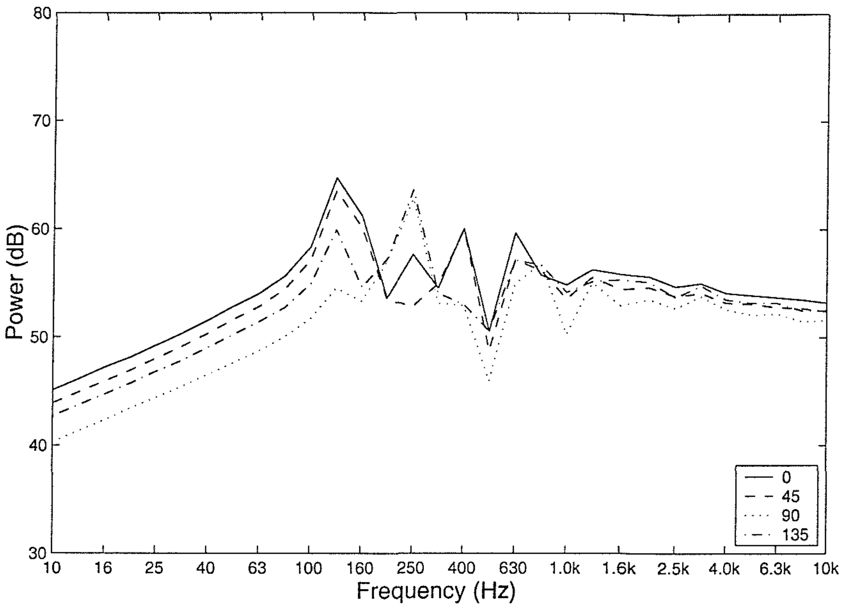

Figure 4.15. The variation with frequency of the amplitudes of the excitation power flow expressed in a 1/3 Oct scale for different angles of application of force γ (see, figure 4.5).

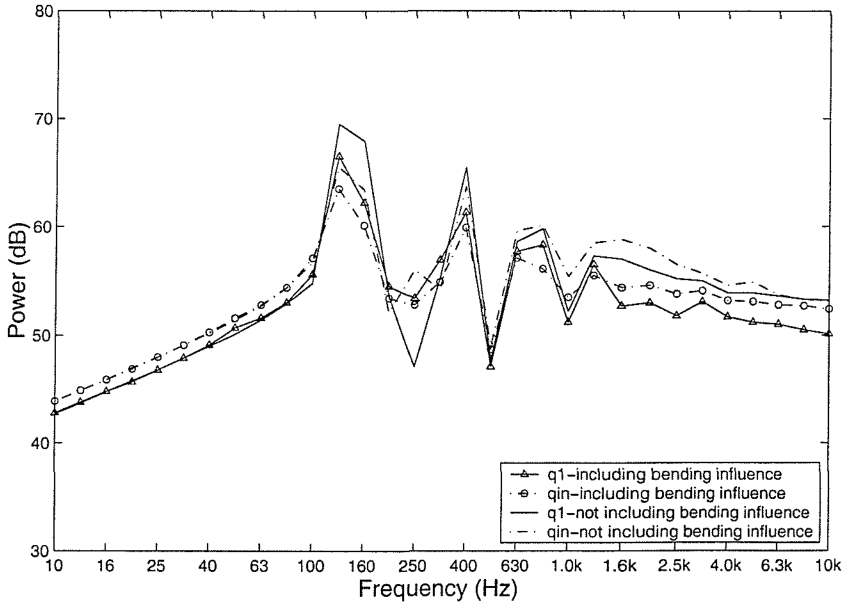

Figure 4.16. The variation with frequency of the amplitudes of the power flow in rod 1 and excitation expressed in a 1/3 Oct scale.

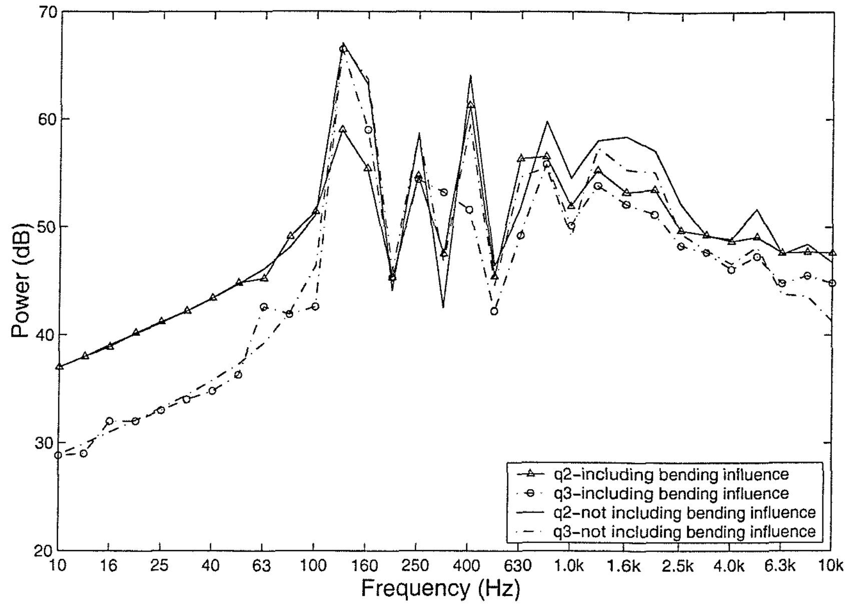

Figure 4.17. The variation with frequency of the amplitudes of the power flow $q_2(t)$, $q_3(t)$ in rods 2, 3 respectively expressed in a 1/3 Oct scale.

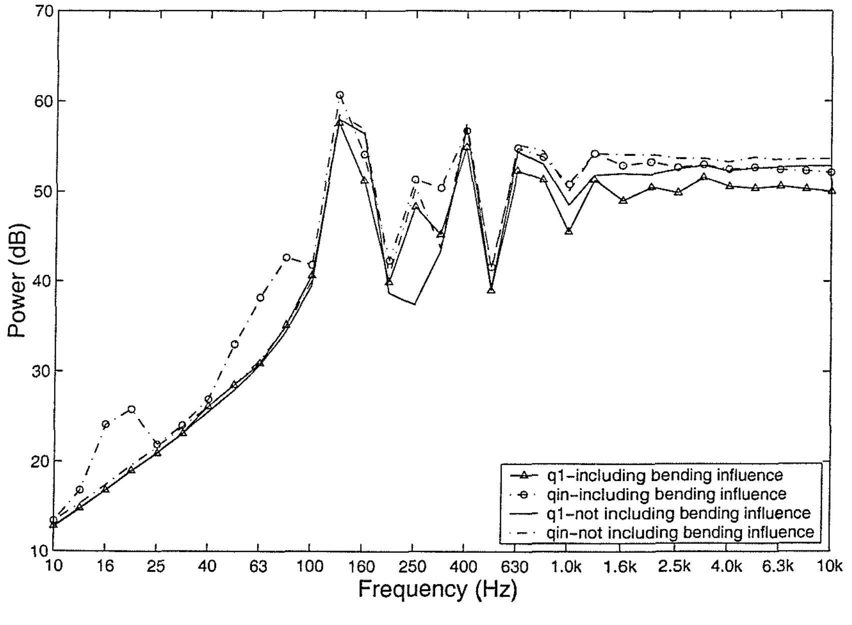

Figure 4.18. The variation with frequency of the time averaged power flow $\langle q_1(t)\rangle$ in rod 1 and excitation $\langle q_{in}(t)\rangle$ expressed in a 1/3 Oct scale.

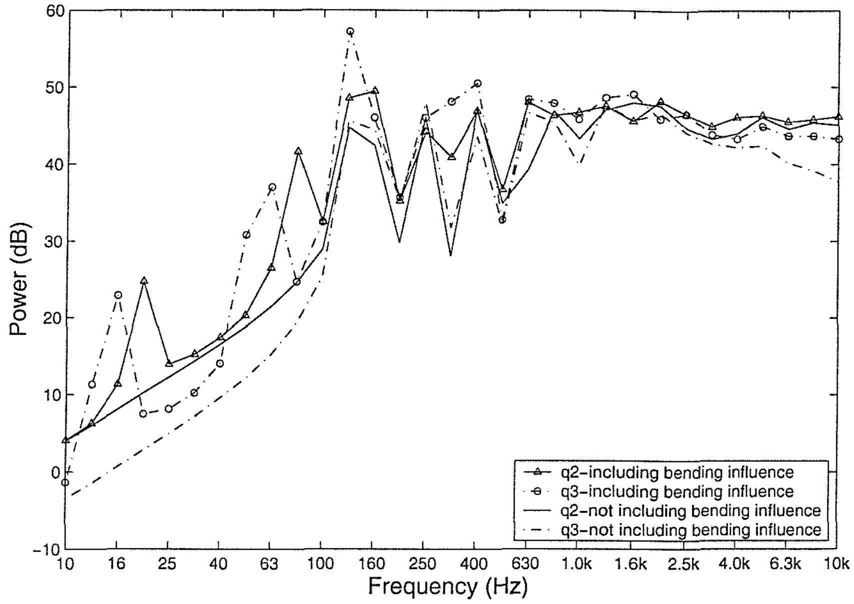

Figure 4.19. The variation with frequency of the time averaged power flow $\langle q_2(t) \rangle$, $\langle q_3(t) \rangle$ in rods 2, 3 respectively expressed in a 1/3 Oct scale.

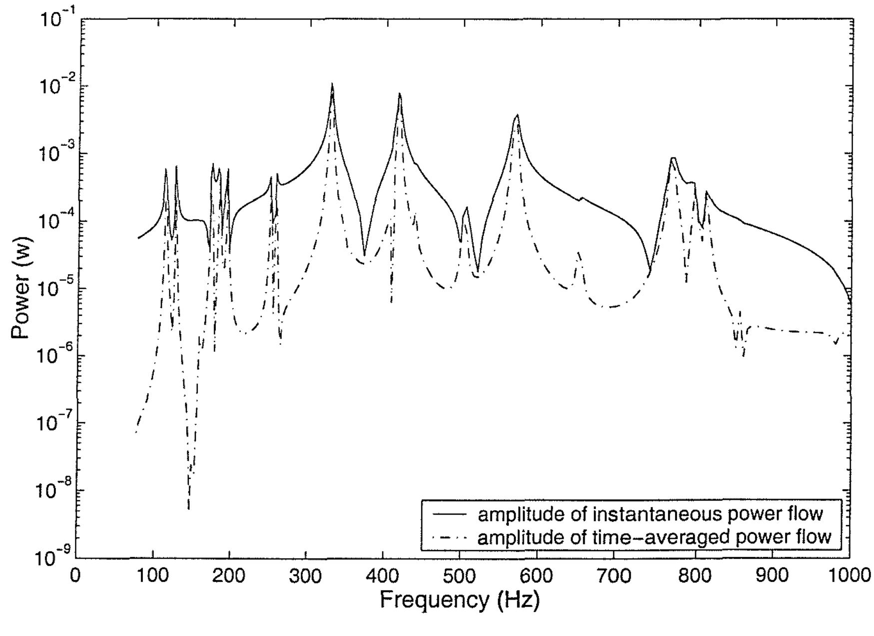

Figure 4.20. The variation with frequency of the amplitudes of the power flow in junction A.

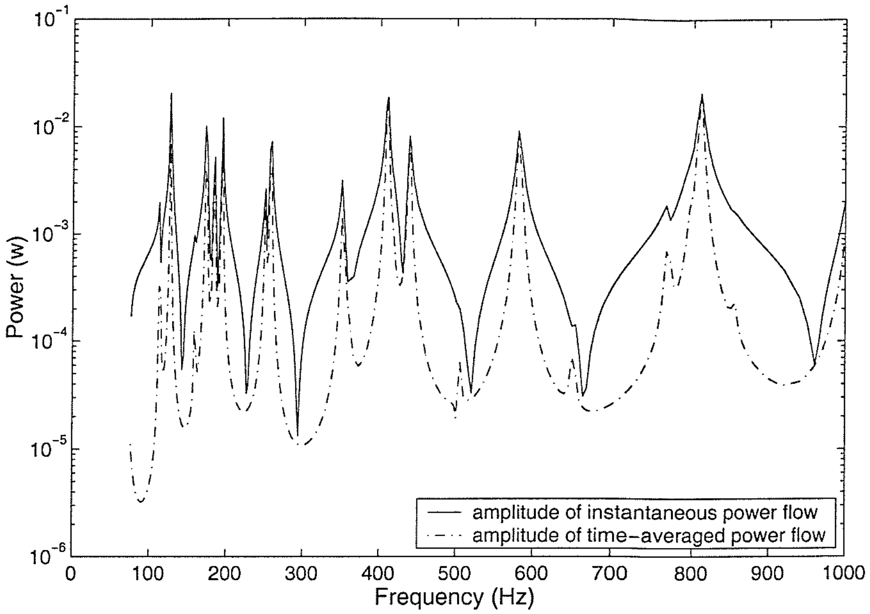

Figure 4.21. The variation with frequency of the amplitudes of the power flow in junction *C*.

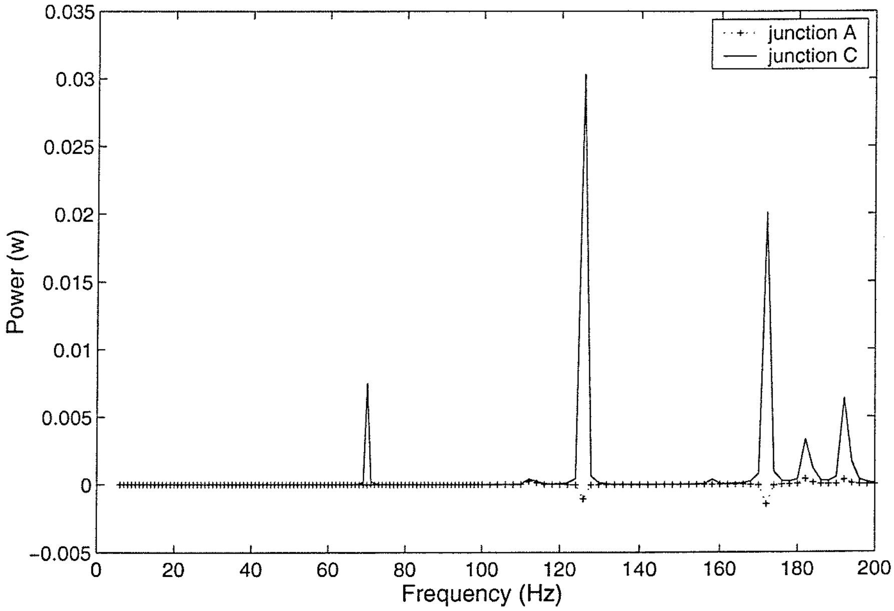

Figure 4.22. The variation with frequency of the time averaged power flow in junctions *A* and *C*.

5. POWER FLOW ANALYSIS IN COUPLED PLATE SYSTEMS

In this chapter, the power flow characteristics of two coupled plate systems are examined. One is a L-shaped plate system and the other is a corner plate system. It is assumed that all substructures in these two systems are thin uniform rectangular plates.

The substructure approach discussed in chapter 3 is used to evaluate the vibration power flow characteristics of the two proposed systems. Hence, natural frequencies and mode shapes of the single plate are first determined using both theoretical solution and FEA and then a mobility function or frequency response function is derived for the coupled system by introducing the force balance equations and geometrical compatibility conditions. Both instantaneous and time-averaged power flows within the system and across the coupling edges are calculated and their characteristics discussed.

5.1. Substructure Analysis of a Coupled Plate System

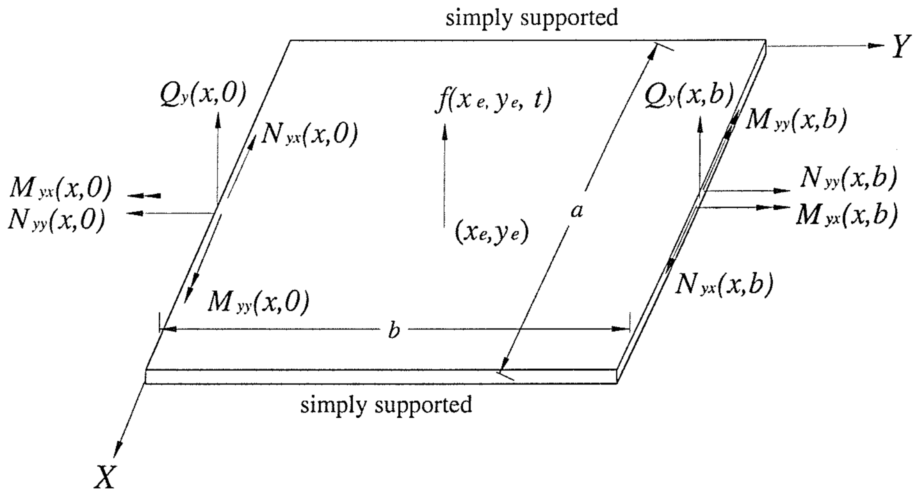

Figure 5.1. Schematic illustration of a uniform rectangular plate in the local co-ordinate system.

Figure 5.1 shows a substructure treat as an idealised system consisting of a single rectangular uniform plate of length a and width b. The material properties of this plate are mass density ρ, elastic Young's modulus E and its structural damping properties are represented by a linear Voigt viscoelastic model with hysteretic damping or loss factor η. A harmonic external exciting force is applied at (x_e, y_e) and internal distributed coupling forces act on the free edge of the plate.

5.1.1. In-plane Vibration of a Thin Rectangular Plate

The basic underlying assumption of in-plane vibration of a rectangular plate lies in the fact that a small deflection and small slope in the deformed shape leads to a bending vibration in the plate which is uncoupled from the in-plane vibration. The differential equations describing in-plane vibration of a plate (see, for example, Leissa 1993) under excitation force vector $\left[\tilde{f}_x, \tilde{f}_y\right]e^{i\omega t}$ at position (x_e, y_e) are given by

$$C_L^2 \frac{\partial^2 \tilde{u}_x}{\partial x^2} + C_T^2 \frac{\partial^2 \tilde{u}_x}{\partial y^2} + (\mu C_L^2 + C_T^2)\frac{\partial^2 \tilde{u}_y}{\partial x \partial y} + \omega^2 \tilde{u}_x = -\frac{\tilde{f}_x}{\rho h}\delta(x - x_e)\delta(y - y_e), \quad (5.1)$$

$$C_L^2 \frac{\partial^2 \tilde{u}_y}{\partial y^2} + C_T^2 \frac{\partial^2 \tilde{u}_y}{\partial x^2} + (\mu C_L^2 + C_T^2)\frac{\partial^2 \tilde{u}_x}{\partial x \partial y} + \omega^2 \tilde{u}_y = -\frac{\tilde{f}_y}{\rho h}\delta(x - x_e)\delta(y - y_e), \quad (5.2)$$

where $\tilde{u}_x, \tilde{u}_y$ are the displacements in the x and y directions respectively. $C_L^2 = E/\rho(1-\mu^2)$, $C_T^2 = E/2\rho(1+\mu)$ denote the square of the longitudinal wave speed and transverse (in-plane) shear wave speed in the plate respectively. μ denotes the Poisson ratio and h the thickness of the plate.

Theoretical solutions of equations (5.1), (5.2) are difficult to derive analytically because these two equations are coupled. Numerical methods, for example FEA, can be used to obtain accurate solutions for the in-plane vibration of the plate under different boundary conditions (see, Grice & Pinnington 2000). Langley (1989), Farag & Pan (1998) resort to an approximate method for simple engineering applications. They assume neglect of the coupling between displacement responses $\tilde{u}_x$ and $\tilde{u}_y$ resulting in the absence of the third term on the left hand side of equations (5.1), (5.2). The coupling between $\tilde{u}_x$ and $\tilde{u}_y$ is due to Poisson effects and shear waves accompanying the longitudinal waves. The main emphasis of the present study is to assess the coupling between longitudinal and flexural vibrations of the plates at the coupling edge, so it is reasonable to neglect the influences of Poisson effects and shear waves in the manner of

Farag & Pan (1998). When the plate is assumed clamped at *x=0, x=a, y=0* and free at *y=b,* the solution of equation (5.2) takes the form

$$\tilde{u}_y(x,y,t) \approx \sum_{r=1}^{n} \sum_{s=1,3,5,\cdots}^{m} A_{rs} \sin\frac{r\pi x}{a} \sin\frac{s\pi y}{2b} e^{i\omega t} \,. \tag{5.3}$$

The governing equation for in-plane vibration becomes

$$\sum_{r=1}^{n} \sum_{s=1,3,\cdots}^{m} \left\{ C_L^2 \left(\frac{s\pi}{2b}\right)^2 + C_T^2 \left(\frac{r\pi}{a}\right)^2 - \omega^2 \right\} \sin\frac{r\pi x}{a} \sin\frac{s\pi y}{2b} A_{rs} = \frac{\tilde{f}_y}{\rho h} \delta(x-x_e)\delta(y-y_e) \tag{5.4}$$

and after using the orthogonal property of the assumed principal mode shapes,

$$A_{rs} = \frac{4\tilde{f}_y \sin\dfrac{r\pi x_e}{a} \sin\dfrac{s\pi y_e}{2b}}{\rho abh\left[C_L^2\left(\dfrac{r\pi}{a}\right)^2 + C_T^2\left(\dfrac{s\pi}{2b}\right)^2 - \omega^2\right]} \tag{5.5}$$

for $r = 1,2,3,\cdots\cdots,n$ and $s = 1,3,5,\cdots\cdots,m$.

The displacement response $\tilde{u}_x$ in the *x* direction has the same form as described in equations (5.3), (5.5). These solutions can be expressed in a receptance function form similar to equation (3.10).

When the plate is assumed clamped at *x=0, x=a* and free at *y=0, y=b,* in a similar manner to equations (5.3), (5.5), the solution of equation (5.2) takes the form

$$\tilde{u}_y(x,y,t) \approx \sum_{r=1}^{n} \sum_{s=0}^{m} A_{rs} \sin\frac{r\pi x}{a} \cos\frac{s\pi y}{b} e^{i\omega t} \tag{5.6}$$

and

$$A_{rs} = \frac{4\tilde{f}_y \sin\dfrac{r\pi x_e}{a} \cos\dfrac{s\pi y_e}{b}}{\rho abh\left[C_L^2\left(\dfrac{r\pi}{a}\right)^2 + C_T^2\left(\dfrac{s\pi}{2b}\right)^2 - \omega^2\right]}, \tag{5.7}$$

for $r = 1,2,3,\cdots\cdots,n$ and $s = 0,1,2,\cdots\cdots,m$.

The internal forces per unit width caused by in-plane vibration are given by

$$\tilde{N}_{xx} = \frac{Eh}{1-\mu^2}\left(\frac{\partial \tilde{u}_x}{\partial x} + \mu\frac{\partial \tilde{u}_y}{\partial y}\right), \; \tilde{N}_{yy} = \frac{Eh}{1-\mu^2}\left(\frac{\partial \tilde{u}_y}{\partial y} + \mu\frac{\partial \tilde{u}_x}{\partial x}\right),$$

$$\tilde{N}_{xy} = \tilde{N}_{yx} = \frac{Eh}{2(1+\mu)}\left(\frac{\partial \tilde{u}_x}{\partial y} + \frac{\partial \tilde{u}_y}{\partial x}\right) \tag{5.8}$$

and are determined knowing $\tilde{u}_x$ and $\tilde{u}_y$.

5.1.2. Bending Vibration of a Thin Rectangular Plate

For transverse bending vibration of a thin plate it is assumed that the deflection, $\tilde{u}_z$, of a plate is small when compared with the plate thickness h. The normal stresses in the direction transverse to the plate can be ignored. There is no force resultant on the cross-sectional area of a plate element. The middle plane of a plate does not undergo deformation during bending and can be regarded as a neutral plane. Any straight normal to the middle plane before deformation remains a straight line normal to the neutral plane during deformation.

Under these assumptions of thin plate theory, the differential equation with hysteric loss factor η (see, for example, Leissa 1993) describing plate bending vibration is expressed as

$$\rho h\ddot{\tilde{u}}_z(x,y,t) + D(1+\mathrm{i}\eta)\nabla^4\tilde{u}_z(x,y,t) = \tilde{f}(x,y,t), \tag{5.9}$$

with stress-displacement relations

$$\tilde{M}_{xx} = -D\left(\frac{\partial^2 \tilde{u}_z}{\partial x^2} + \mu\frac{\partial^2 \tilde{u}_z}{\partial y^2}\right), \; \tilde{M}_{yy} = -D\left(\frac{\partial^2 \tilde{u}_z}{\partial y^2} + \mu\frac{\partial^2 \tilde{u}_z}{\partial x^2}\right),$$

$$\tilde{M}_{xy} = \tilde{M}_{yx} = -D(1-\mu)\frac{\partial^2 \tilde{u}_z}{\partial x \partial y}, \tag{5.10}$$

$$\tilde{Q}_x = -D\left(\frac{\partial^3 \tilde{u}_z}{\partial x^3} + \frac{\partial^3 \tilde{u}_z}{\partial x \partial y^2}\right), \; \tilde{Q}_y = -D\left(\frac{\partial^3 \tilde{u}_z}{\partial y^3} + \frac{\partial^3 \tilde{u}_z}{\partial x^2 \partial y}\right). \tag{5.11}$$

Here $\tilde{f}(x,y,t)$ denotes the distribution of exciting force which includes the external transverse force and internal coupling force, ∇^4 represents the bi-harmonic operator, $\tilde{Q}_x, \tilde{Q}_y$ the transverse shear forces per unit length and $\tilde{M}_{xx}, \tilde{M}_{yy}, \tilde{M}_{xy}$ the internal bending moments and twisting moment per unit length. The plate flexural rigidity D is given by

$$D = \frac{Eh^3}{12(1-\mu^2)}. \tag{5.12}$$

For free vibration it is reasonable to assume that the displacement is a harmonic function of time, i.e.

$$\tilde{u}_z(x, y, t) = U_z(x, y)e^{\mathrm{i}(\omega t+\varphi)}. \tag{5.13}$$

Substituting equation (5.13) into equation (5.9), we find the auxiliary equation for U_z of free vibration becomes

$$\frac{\partial^4 U_z}{\partial x^4} + 2\frac{\partial^4 U_z}{\partial x^2 \partial y^2} + \frac{\partial^4 U_z}{\partial y^4} - \frac{\rho\omega^2}{D}U_z = 0. \tag{5.14}$$

For a uniform rectangular plate, the analytical solution of equation (5.14) exists only when two opposite edges of the plate are simply supported because two variables x, y in U_z are coupled under general boundary conditions. When two opposing edges of a rectangular plate are simply supported at $x=0$ and $x=a$, as shown in figure 5.1, two variables x, y in U_z are uncoupled and U_z can be expressed using the Levy solution as follows

$$U_z(x, y) = \sum_{r=1}^{n} Y_r(y)\sin\frac{r\pi x}{a}. \tag{5.15}$$

The substitution of equation (5.15) into equation (5.14) gives the auxiliary equation for Y_r in the form

$$\sum_{r=1}^{n}\left\{\frac{d^4 Y_r}{dy^4} - 2\left(\frac{r\pi}{a}\right)^2\frac{d^2 Y_r}{dy^2} + \left[\left(\frac{r\pi}{a}\right)^4 - \frac{\rho\omega^2}{D}\right]Y_r\right\}\sin\frac{r\pi x}{a} = 0. \tag{5.16}$$

Equation (5.16) is the Fourier expansion of a function having zero value over the interval from $x=0$ to $x=a$. The coefficients, that is, the quantities inside the parentheses, must be zero for each r, i.e.

$$\frac{d^4 Y_r}{dy^4} - 2\left(\frac{r\pi}{a}\right)^2\frac{d^2 Y_r}{dy^2} + \left[\left(\frac{r\pi}{a}\right)^4 - \frac{\rho\omega^2}{D}\right]Y_r = 0 \tag{5.17}$$

with solution

$$Y_r(y) = A_r \cosh {}^{\beta_r y}\!/_{b} + B_r \sinh {}^{\beta_r y}\!/_{b} + C_r \cos {}^{\gamma_r y}\!/_{b} + D_r \sin {}^{\gamma_r y}\!/_{b}, \tag{5.18}$$

for $k^2 > (r\pi)^2$ and

$$Y_r(y) = A_r \cosh {}^{\beta_r y}\!/_{b} + B_r \sinh {}^{\beta_r y}\!/_{b} + C_r \cosh {}^{\gamma_r y}\!/_{b} + D_r \sinh {}^{\gamma_r y}\!/_{b}, \tag{5.19}$$

for $k^2 \leq (r\pi)^2$,

where

$$\beta_r = \phi\sqrt{k^2 + (r\pi)^2},\ \gamma_r = \phi\sqrt{\left|k^2 - (r\pi)^2\right|} \tag{5.20}$$

and

$$k^2 = a^2\omega\sqrt{{}^{\rho}\!/_{D}},\ \phi = {}^{b}\!/_{a}. \tag{5.21}$$

The constant coefficients in equations (5.18) and (5.19) are determined from prescribed boundary conditions. Generally, the boundary conditions used in this free-free interface substructure approach are two opposite edges free, or simply supported and one edge free, the other simply supported.

When the plate is simply supported at $y=0$, free at $y=b$, the boundary conditions are

At $y=0$, displacement $Y_r=0$, i.e. $A_r+C_r=0$. (5.22)

At $y=0$, bending moment $\tilde{M}_{yy} = \dfrac{\partial^2 \tilde{u}_z}{\partial y^2} + \mu \dfrac{\partial^2 \tilde{u}_z}{\partial x^2} = 0$, i.e. $A_r\beta_r^2 - C_r\gamma_r^2 = 0$, (5.23)

so, $A_r=C_r=0$.

At $y=b$, bending moment $\tilde{M}_{yy} = \dfrac{\partial^2 \tilde{u}_z}{\partial y^2} + \mu \dfrac{\partial^2 \tilde{u}_z}{\partial x^2} = 0$, i.e.

$$B_r\left[\beta_r^2 - \mu\phi^2(r\pi)^2\right]\sinh\beta_r - D_r\left[\gamma_r^2 + \mu\phi^2(r\pi)^2\right]\sin\gamma_r = 0, \tag{5.24}$$

for $k^2 > (r\pi)^2$ and

$$B_r\left[\beta_r^2 - \mu\phi^2(r\pi)^2\right]\sinh\beta_r + D_r\left[\gamma_r^2 - \mu\phi^2(r\pi)^2\right]\sinh\gamma_r = 0, \tag{5.25}$$

for $k^2 \le (r\pi)^2$.

At $y=b$, effective shear force (see, Warburton 1976), $\frac{\partial^3 \tilde{u}_z}{\partial y^3}+(2-\mu)\frac{\partial^3 \tilde{u}_z}{\partial x^2 \partial y}=0$, i.e.

$$B_r\left[\beta_r\left(\beta_r^2-(2-\mu)\phi^2(r\pi)^2\right)\right]\cosh\beta_r - D_r\left[\gamma_r\left(\gamma_r^2+(2-\mu)\phi^2(r\pi)^2\right)\right]\cos\gamma_r = 0 \qquad (5.26)$$

for $k^2 > (r\pi)^2$ and

$$B_r\left[\beta_r\left(\beta_r^2-(2-\mu)\phi^2(r\pi)^2\right)\right]\cosh\beta_r + D_r\left[\gamma_r\left(\gamma_r^2-(2-\mu)\phi^2(r\pi)^2\right)\right]\cosh\gamma_r = 0 \qquad (5.27)$$

for $k^2 \le (r\pi)^2$.

Eliminating B_r/D_r, we find the eignvalue equation and relative principal mode shapes are given by

$$\begin{aligned}&\gamma_r\left(\gamma_r^2+(2-\mu)\phi^2 r^2\pi^2\right)\left(\beta_r^2-\mu\phi^2 r^2\pi^2\right)\sinh\beta_r\cos\gamma_r \\ &= \beta_r\left(\beta_r^2-(2-\mu)\phi^2 r^2\pi^2\right)\left(\gamma_r^2+\mu\phi^2 r^2\pi^2\right)\cosh\beta_r\sin\gamma_r\end{aligned}, \qquad (5.28)$$

$$\varphi_r(x,y)=\left[\sin\frac{\gamma_r y}{b}+\frac{\left(\gamma_r^2+\mu\phi^2 r^2\pi^2\right)\sin\gamma_r}{\left(\beta_r^2-\mu\phi^2 r^2\pi^2\right)\sinh\beta_r}\sinh\frac{\beta_r y}{b}\right]\sin\frac{r\pi x}{a}, \qquad (5.29)$$

for $k^2 > (r\pi)^2$ and $r=1,2,3,\cdots\cdots$, or

$$\begin{aligned}&\gamma_r\left(\gamma_r^2-(2-\mu)\phi^2 r^2\pi^2\right)\left(\beta_r^2-\mu\phi^2 r^2\pi^2\right)\sinh\beta_r\cosh\gamma_r \\ &= \beta_r\left(\beta_r^2-(2-\mu)\phi^2 r^2\pi^2\right)\left(\gamma_r^2-\mu\phi^2 r^2\pi^2\right)\cosh\beta_r\sinh\gamma_r\end{aligned}, \qquad (5.30)$$

$$\varphi_r(x,y)=\left[\sinh\frac{\gamma_r y}{b}-\frac{\left(\gamma_r^2-\mu\phi^2 r^2\pi^2\right)\sinh\gamma_r}{\left(\beta_r^2-\mu\phi^2 r^2\pi^2\right)\sinh\beta_r}\sinh\frac{\beta_r y}{b}\right]\sin\frac{r\pi x}{a}, \qquad (5.31)$$

for $k^2 \le (r\pi)^2$.

For any r $(=1,2,3,\cdots\cdots)$, a series solution of k, which can be expressed as k_{rs} ($r=1,2,3,\cdots\cdots$; $s=1,2,3,\cdots\cdots$.) is obtained numerically from eigenvalue equation (5.28) or (5.30). The natural frequencies are determined thus in the form $\omega_{rs}=(k_{rs}^2/a^2)\sqrt{D/\rho}$. Its relative principal mode shape $\varphi_r(x,y)$ determined by equation (5.29) or (5.31) should then be rewritten as $\varphi_{rs}(x,y)$ ($r=1,2,3,\cdots\cdots$; $s=1,2,3,\cdots\cdots$.).

Similarly, when both edges at *y=0* and *y=b* (see, for example, figure 5.1) are free, the eignvalue equation and relative principal mode shapes are given by

$$\begin{aligned}&\gamma_r\left(\gamma_r^2+(2-\mu)\phi^2r^2\pi^2\right)\left(\beta_r^2-\mu\phi^2r^2\pi^2\right)\sin\frac{1}{2}\gamma_r\cosh\frac{1}{2}\beta_r\\&=-\beta_r\left(\beta_r^2-(2-\mu)\phi^2r^2\pi^2\right)\left(\gamma_r^2+\mu\phi^2r^2\pi^2\right)\sinh\frac{1}{2}\beta_r\cos\frac{1}{2}\gamma_r\end{aligned}, \tag{5.32}$$

$$\varphi_r(x,y)=\left[\cos\frac{\gamma_r y}{b}+\frac{\left(\gamma_r^2+\mu\phi^2r^2\pi^2\right)\cos\frac{1}{2}\gamma_r}{\left(\beta_r^2-\mu\phi^2r^2\pi^2\right)\cosh\frac{1}{2}\beta_r}\cosh\frac{\beta_r y}{b}\right]\sin\frac{r\pi x}{a}, \tag{5.33}$$

for symmetric modes, for $k^2>(r\pi)^2$,

$$\begin{aligned}&\gamma_r\left(\gamma_r^2-(2-\mu)\phi^2r^2\pi^2\right)\left(\beta_r^2-\mu\phi^2r^2\pi^2\right)\sinh\frac{1}{2}\gamma_r\cosh\frac{1}{2}\beta_r\\&=\beta_r\left(\beta_r^2-(2-\mu)\phi^2r^2\pi^2\right)\left(\gamma_r^2-\mu\phi^2r^2\pi^2\right)\sinh\frac{1}{2}\beta_r\cosh\frac{1}{2}\gamma_r\end{aligned}, \tag{5.34}$$

$$\varphi_r(x,y)=\left[\cosh\frac{\gamma_r y}{b}-\frac{\left(\gamma_r^2-\mu\phi^2r^2\pi^2\right)\cosh\frac{1}{2}\gamma_r}{\left(\beta_r^2-\mu\phi^2r^2\pi^2\right)\cosh\frac{1}{2}\beta_r}\cosh\frac{\beta_r y}{b}\right]\sin\frac{r\pi x}{a}, \tag{5.35}$$

for symmetric modes, $k^2\le(r\pi)^2$,

$$\begin{aligned}&\gamma_r\left(\gamma_r^2+(2-\mu)\phi^2r^2\pi^2\right)\left(\beta_r^2-\mu\phi^2r^2\pi^2\right)\cos\frac{1}{2}\gamma_r\sinh\frac{1}{2}\beta_r\\&=\beta_r\left(\beta_r^2-(2-\mu)\phi^2r^2\pi^2\right)\left(\gamma_r^2+\mu\phi^2r^2\pi^2\right)\cosh\frac{1}{2}\beta_r\sin\frac{1}{2}\gamma_r\end{aligned}, \tag{5.36}$$

$$\varphi_r(x,y)=\left[\sin\frac{\gamma_r y}{b}+\frac{\left(\gamma_r^2+\mu\phi^2r^2\pi^2\right)\sin\frac{1}{2}\gamma_r}{\left(\beta_r^2-\mu\phi^2r^2\pi^2\right)\sinh\frac{1}{2}\beta_r}\sinh\frac{\beta_r y}{b}\right]\sin\frac{r\pi x}{a}, \tag{5.37}$$

for anti-symmetric modes, $k^2>(r\pi)^2$ and

$$\begin{aligned}&\gamma_r\left(\gamma_r^2-(2-\mu)\phi^2r^2\pi^2\right)\left(\beta_r^2-\mu\phi^2r^2\pi^2\right)\cosh\frac{1}{2}\gamma_r\sinh\frac{1}{2}\beta_r\\&=\beta_r\left(\beta_r^2-(2-\mu)\phi^2r^2\pi^2\right)\left(\gamma_r^2-\mu\phi^2r^2\pi^2\right)\cosh\frac{1}{2}\beta_r\sinh\frac{1}{2}\gamma_r\end{aligned}, \tag{5.38}$$

$$\varphi_r(x,y)=\left[\sinh\frac{\gamma_r y}{b}-\frac{\left(\gamma_r^2-\mu\phi^2r^2\pi^2\right)\sinh\frac{1}{2}\gamma_r}{\left(\beta_r^2-\mu\phi^2r^2\pi^2\right)\sinh\frac{1}{2}\beta_r}\sinh\frac{\beta_r y}{b}\right]\sin\frac{r\pi x}{a}, \tag{5.39}$$

for anti-symmetric modes, $k^2\le(r\pi)^2$, $r=1,2,3,\cdots\cdots$.

If the boundary conditions of these two edges (*y=0* and *y=b*) are both simply supported, the solution of equation (5.14) is relatively simple and can be expressed as

$$\omega_{rs}=\pi^2\left(\frac{r^2}{a^2}+\frac{s^2}{b^2}\right)\sqrt{\frac{D}{\rho h}}, \tag{5.40}$$

$$\varphi_r(x,y)=\sin\frac{r\pi x}{a}\sin\frac{s\pi y}{b}. \tag{5.41}$$

According to a theorem due to Rayleigh (1896), any distortion of the plate may be expressed as

$$\tilde{u}_z(x,y,t)=\sum_{r=1}^{n}\sum_{s=1}^{m}\varphi_{rs}(x,y)\tilde{p}_{rs}(t)\ . \tag{5.42}$$

When the excitation $\tilde{f}(x,y,t)$ is harmonic and consists of an external exciting force $\tilde{F}(x_e,y_e)e^{\mathrm{i}\omega t}$ at position (x_e,y_e) and internal distributed forces $\tilde{Q}_y(x,b)e^{\mathrm{i}\omega t}$, $\tilde{M}_{yy}(x,b)e^{\mathrm{i}\omega t}$ at coupling edge (*y=b*), the principal co-ordinate $\tilde{p}_{rs}(t)$ of the plate under examination (see, for example, Cremer, *et al* 1988), using the orthogonality of principal mode shapes, is given by

$$\tilde{p}_{rs}(t)=\frac{\tilde{F}(x_e,y_e)\varphi_{rs}(x_e,y_e)+\int_0^a\left[\tilde{Q}_y(x,b)\varphi_{rs}(x,b)+\tilde{M}_{yy}(x,b)\varphi'_{rs}(x,b)\right]dx}{m_{rs}\left[\omega_{rs}^2-\omega^2+\mathrm{i}\omega_{rs}^2\eta\right]}e^{\mathrm{i}\omega t}, \tag{5.43}$$

where $m_{rs}=\int_0^a\int_0^b\rho h\varphi_{rs}^2(x,y)dxdy$ denotes the generalised mass and $\varphi'_{rs}(x,b)=\left.\frac{\partial\varphi_{rs}(x,y)}{\partial y}\right|_{y=b}$.

Thus the displacement of the rectangular plate is expressed as

$$\tilde{u}_z(x,y,t)=\sum_{r=1}^{n}\sum_{s=1}^{m}\varphi_{rs}(x,y)\frac{\tilde{F}(x_e,y_e)\varphi_{rs}(x_e,y_e)+\int_0^a\left[\tilde{Q}_y(x,b)\varphi_{rs}(x,b)+\tilde{M}_{yy}(x,b)\varphi'_{rs}(x,b)\right]dx}{m_{rs}\left[\omega_{rs}^2-\omega^2+\mathrm{i}\eta\omega_{rs}^2\right]}e^{\mathrm{i}\omega t} \tag{5.44}$$

with the rotation angles, $\tilde{\theta}_x(x,y,t)=\dfrac{\partial\tilde{u}_z(x,y,t)}{\partial y}=\displaystyle\sum_{r=1}^{n}\sum_{s=1}^{m}\frac{\partial\varphi_{rs}(x,y)}{\partial y}\tilde{p}_{rs}(t)$ (5.45)

$$\text{and}\quad \tilde{\theta}_y(x,y,t)=\frac{\partial\tilde{u}_z(x,y,t)}{\partial x}=\sum_{r=1}^{n}\sum_{s=1}^{m}\frac{\partial\varphi_{rs}(x,y)}{\partial x}\tilde{p}_{rs}(t). \tag{5.46}$$

The dynamic responses of the plate under internal distributed forces $\tilde{Q}_y$, $\tilde{M}_{yy}$ at coupling edge (*y=0*) or at both coupling edges (*y=0* and *y=b*) have the same forms as derived in equations (5.44)-(5.46).

Equations (5.44)-(5.46) describe the relationship between the general displacement responses and excitations, that is, the receptance functions. It is noted that all the receptance functions and internal forces have complex values because of the influence of damping.

5.1.3. The Coupling of Substructures

The L-shaped plate system under investigation is shown in figure 5.2. This total system can be separated into two subsystems with each subsystem under examination as shown in figure 5.1. Here, it is assumed that the rectangular plate has simply supported boundary conditions applied to three edges of the plate with the coupling edge (*y=0* in the local co-ordinate system) assumed free. The corner plate system (shown in figure 5.4) has a similar coupling relationship but there now exist three substructures and three coupling edges.

Two kinds of forces act on each substructure. One is the external excitation force at position (x_e, y_e) whereas the other is the internal distributed coupling force acting at the coupling edge, see figure 5.1. The whole system is coupled at the coupling edge by the distributed internal forces of bending moment $\tilde{M}_{yy}$, transverse shear force $\tilde{Q}_y$ and in-plane longitudinal force $\tilde{N}_{yy}$ along the free edge of each subsystem.

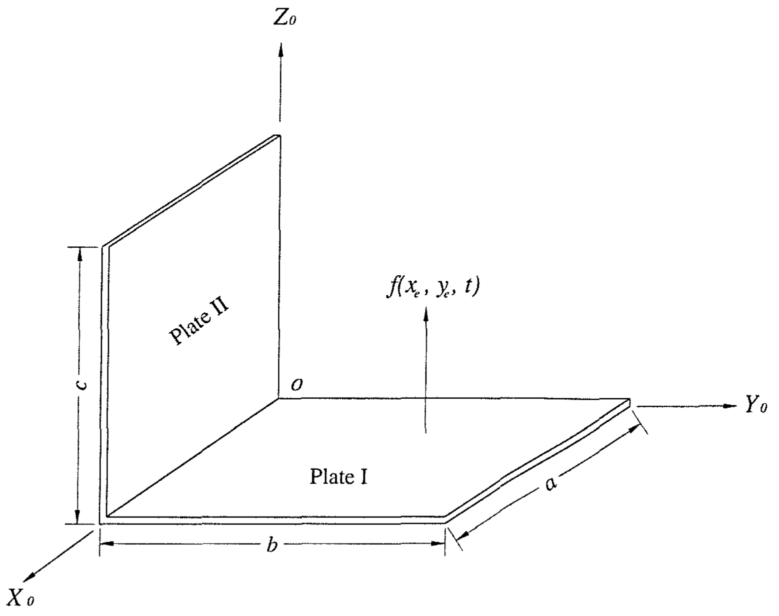

Figure 5.2. Schematic illustration of a L-shaped plate system.

The internal force vector $\left[\tilde{f}^c\right]=\left[\tilde{N}_{yy},\tilde{Q}_y,\tilde{M}_{yy}\right]^T$ and relative displacement vector $\left[\tilde{u}^c\right]=\left[\tilde{u}_y,\tilde{u}_z,\tilde{\theta}_x\right]^T$ at the coupling edge in the local co-ordinate axis reference system (*X*, *Y*, *Z*) are related to those in the global co-ordinate (X_0, Y_0, Z_0) by a co-ordinate transformation matrix $[Tr]$ (see, for example, Reismann & Pawlik 1980) expressed as

$$\left[\tilde{f}_0^c\right]=[Tr]\left[\tilde{f}^c\right] \text{ and } \left[\tilde{u}_0^c\right]=[Tr]\left[\tilde{u}^c\right], \tag{5.47}$$

where

$$[Tr]=\begin{bmatrix}\cos\alpha & -\sin\alpha & 0\\ \sin\alpha & \cos\alpha & 0\\ 0 & 0 & 1\end{bmatrix}. \tag{5.48}$$

The coupling relationship between two connected plates is expressed by their force balance and geometric compatibility conditions at the coupling edge in the global co-ordinate system. That is,

$$[Tr_1]\left[\tilde{u}_1^c\right]=[Tr_2]\left[\tilde{u}_2^c\right], \tag{5.49}$$

$$[Tr_1]\left[\tilde{f}_1^{\,c}\right]+[Tr_2]\left[\tilde{f}_2^{\,c}\right]=0. \tag{5.50}$$

From equations (3.22) and (5.44)-(5.46), the displacement vectors at the coupling edges can be further expressed in terms of components excited by an external excitation vector $\left[\tilde{f}^{\,e}\right]$ and an internal coupling force vector $\left[\tilde{f}^{\,c}\right]$. For example, the displacement vector on the Ith plate is given by

$$\left[\tilde{u}_I^c\right]=\left[R_I^e\right]\left[\tilde{f}_I^e\right]+\left[R_I^c\right]\left[\tilde{f}_I^c\right],\ I=1,2. \tag{5.51}$$

Here, $\left[R_I^e\right]$ and $\left[R_I^c\right]$ denote the receptance functions between displacements at interface and external excitations or internal coupling forces of two substructures respectively.

Equation (5.50) can be rewritten as

$$\left[\tilde{f}_2^{\,c}\right]=-[Tr_2]^{-1}[Tr_1]\left[\tilde{f}_1^{\,c}\right]. \tag{5.52}$$

The substitution of equations (5.51), (5.52) into equation (5.49) gives the coupling forces expressed in the form

$$\left[\tilde{f}_1^{\,c}\right]=\left([Tr_2]\left[R_2^c\right][Tr_2]^{-1}[Tr_1]+[Tr_1]\left[R_1^c\right]\right)^{-1}\left\{[Tr_2]\left[R_2^e\right]\left[\tilde{f}_2^{\,e}\right]-[Tr_1]\left[R_1^e\right]\left[\tilde{f}_1^{\,e}\right]\right\}. \tag{5.53}$$

It therefore follows that the response of the plate system can be determined after solution of the receptance function of a single rectangular plate.

If it is assumed that the coupling edge between the two plates is simply supported, the coupling relationship simplifies to

$$\tilde{\theta}_{x1}=\tilde{\theta}_{x2} \text{ and } \tilde{M}_{yy1}+\tilde{M}_{yy2}=0. \tag{5.54}$$

This formula implies that the coupling relationship is independent of the coupling angle α.

5.2. Power Flow Density Vectors in a Thin Plate

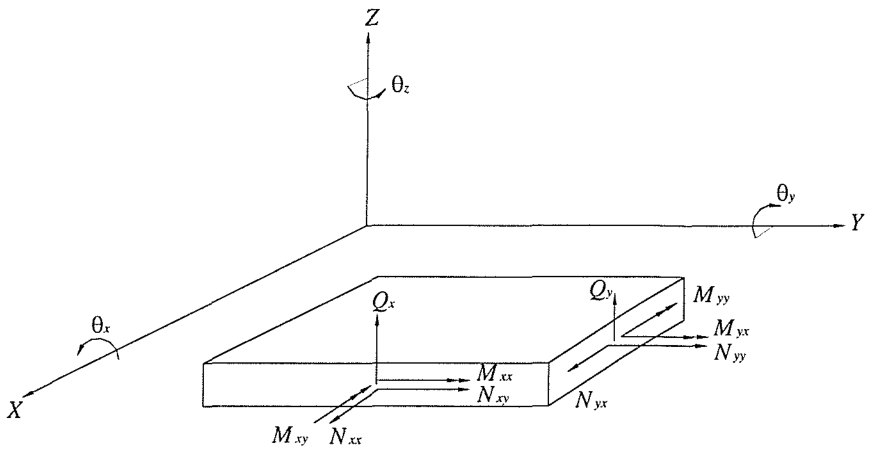

Figure 5.3. Direction convention of force and displacement components on a plate element.

From the general definition of power flow in chapter 2 (also see, Xing & Price 1999), the instantaneous power flow density vector in a thin plate is defined as

$$\begin{aligned} q_x(t) = &-\mathrm{Re}\left\{\dot{\tilde{u}}_z\right\}\mathrm{Re}\left\{\tilde{Q}_x\right\}+\mathrm{Re}\left\{\dot{\tilde{\theta}}_y\right\}\mathrm{Re}\left\{\tilde{M}_{xx}\right\}+\mathrm{Re}\left\{\dot{\tilde{\theta}}_x\right\}\mathrm{Re}\left\{\tilde{M}_{xy}\right\} \\ &-\mathrm{Re}\left\{\dot{\tilde{u}}_x\right\}\mathrm{Re}\left\{\tilde{N}_{xx}\right\}-\mathrm{Re}\left\{\dot{\tilde{u}}_y\right\}\mathrm{Re}\left\{\tilde{N}_{xy}\right\} \end{aligned} \tag{5.55}$$

$$\begin{aligned} q_y(t) = &-\mathrm{Re}\left\{\dot{\tilde{u}}_z\right\}\mathrm{Re}\left\{\tilde{Q}_y\right\}+\mathrm{Re}\left\{\dot{\tilde{\theta}}_x\right\}\mathrm{Re}\left\{\tilde{M}_{yy}\right\}+\mathrm{Re}\left\{\dot{\tilde{\theta}}_y\right\}\mathrm{Re}\left\{\tilde{M}_{xy}\right\} \\ &-\mathrm{Re}\left\{\dot{\tilde{u}}_x\right\}\mathrm{Re}\left\{\tilde{N}_{xy}\right\}-\mathrm{Re}\left\{\dot{\tilde{u}}_y\right\}\mathrm{Re}\left\{\tilde{N}_{yy}\right\} \end{aligned} \tag{5.56}$$

The signs of the second and third terms on the right hand of equations (5.55), (5.56) are dependent on the directions of $\tilde{M}$ and $\dot{\tilde{\theta}}$. They are defined in figure 5.3 based on the sign convention of elasticity theory (see, for example, Reismann & Pawlik 1980).

The time averaged power flow densities over a period of excitation in the thin plate are

$$\left\langle q_x(t)\right\rangle = -\frac{1}{2}\mathrm{Re}\left\{\tilde{Q}_x\dot{\tilde{u}}_z^* - \tilde{M}_{xx}\dot{\tilde{\theta}}_y^* - \tilde{M}_{xy}\dot{\tilde{\theta}}_x^* + \tilde{N}_{xx}\dot{\tilde{u}}_x^* + \tilde{N}_{xy}\dot{\tilde{u}}_y^*\right\}, \tag{5.57}$$

$$\left\langle q_y(t)\right\rangle = -\frac{1}{2}\mathrm{Re}\left\{\tilde{Q}_y\dot{\tilde{u}}_z^* - \tilde{M}_{xy}\dot{\tilde{\theta}}_y^* - \tilde{M}_{yy}\dot{\tilde{\theta}}_x^* + \tilde{N}_{xy}\dot{\tilde{u}}_x^* + \tilde{N}_{yy}\dot{\tilde{u}}_y^*\right\}. \tag{5.58}$$

When the plate is simply supported at all edges and only transverse exciting forces exist, the components of in-plane vibration in equations (5.55)-(5.58) are equal to zero.

The instantaneous and time averaged power flow density vectors in the coupling edge ($y=0$) are only in the y direction and have already been expressed in equations (5.56), (5.58). If the boundary condition on the coupling is also simply supported, the instantaneous and time averaged power flow density vectors in the coupling edge become

$$q_y^c = \mathrm{Re}\{\dot{\tilde{\theta}}_x\}\mathrm{Re}\{\tilde{M}_{yy}\}, \tag{5.59}$$

$$\langle q_y^c \rangle = \frac{1}{2}\mathrm{Re}\{\tilde{M}_{yy}\dot{\tilde{\theta}}_x^*\}. \tag{5.60}$$

The total transmitted power in a coupling edge is given by the integral of the transmitted power flow density along the length of the coupling edge. That is,

$$q_{trans} = \int_0^a q_y^c dx, \tag{5.61}$$

with corresponding time averaged quantity,

$$\langle q_{trans} \rangle = \int_0^a \langle q_y^c \rangle dx. \tag{5.62}$$

It is convenient to determine the power flow at the coupling edge using a substructure receptance approach because the solution of the coupling force in the coupling relationship equations (5.52), (5.53) and the receptance function expressed in equations (5.44)-(5.46) are simple and in the same local co-ordinate axis system.

If an external exciting force $|f|e^{\mathrm{i}\omega t}$ is applied at position (x_e, y_e) and the velocity response at this position is $\tilde{v}_e e^{\mathrm{i}\omega t} = |\tilde{v}_e|e^{\mathrm{i}(\omega t+\varphi_v)}$, the input power from this excitation is given by

$$\begin{aligned} q_{in}(t) &= \mathrm{Re}\{|f|e^{\mathrm{i}\omega t}\}\mathrm{Re}\{\tilde{v}_e e^{\mathrm{i}\omega t}\} \\ &= \frac{1}{2}|f|\cdot|\tilde{v}_e|\cdot[\cos\varphi_v + \cos(2\omega t + \varphi_v)], \end{aligned} \tag{5.63}$$

with corresponding time averaged quantity,

$$\langle q_{in}(t) \rangle = \frac{1}{2}|f|\cdot|\tilde{v}_e|\cos\varphi_v, \tag{5.64}$$

where φ_v denotes the phase angle between exciting force and velocity response.

For illustrative purposes, a power flow analysis of a L-shape plate system and a corner plate system are examined.

5.3. Application to a L-shaped Plate System

Figure 5.2 illustrates the L-shaped plate system under examination. It is assumed that simply supported boundary conditions apply to all edges of the system except the coupling edge. The L-shaped plate system shown in figure 5.2 is defined by the data set:

$\rho = 2710\, kg/m^3$, $E = 72\, GPa$, $\eta = 0.01$, $\mu = 0.3$;

a=1.0 m, $b = c = 0.5\, m$, h=0.00635 m.

Two coupling edge conditions were examined. The first assumes simply supported boundary conditions apply at all edges of each plate including the coupling edge. This system was originally examined by Cuschieri (1990b) to assess the power flow transmitted between two plates adopting a mobility function approach. The other assumes simply supported boundary conditions apply at three edges of each plate but the plates are rigidly connected at the coupling edge. More complex boundary conditions may be adopted, e.g. fixed or free at some edges of a plate, etc, which add complication to the analysis without contributing significant additional insights into the power flow mechanism occurring in the coupled plate system.

5.3.1. Simply Supported Coupling Edge

Figures 5.5 and 5.6 illustrate the variation of the time averaged input power flow and total transmitted power flows along the length of the coupling edge with frequency to a unit amplitude loading applied at different positions. Figure 5.5 shows the results of an excitation at the centre of plate I whereas figure 5.6 displays the predictions caused by a loading at position (0.33 m, 0.125 m) on plate I. The calculated time averaged transmitted power flow values at the coupling edge demonstrate the same trends and magnitudes as those presented by Cuschieri (1990b). The receiving plate i.e. plate II in figure 5.2 is not connected to any other substructure except the source plate (plate I), and thus the transmitted time averaged power in figures 5.5, 5.6 equals the rate of energy dissipation due to the internal loss factor. The total energy dissipation of the system in a period is equal to the time averaged input power in figures 5.5, 5.6.

Because receptance functions of many practical engineering structures cannot be determined theoretically, the results derived by a FEA substructure receptance approach are also included in figures 5.5, 5.6. The FEA plate model has the same structural characteristics as the original substructure and contains 527 nodes and 480 plate-shell elements. Ninety natural frequencies and principal mode shapes of a plate were extracted using FEA package ANSYS spanning the frequency range up to 4150 Hz. It is observed that only small differences exist between the theoretical substructure predictions and those evaluated by the FEA approach after 500 Hz as illustrated in figures 5.5, 5.6. This is because only a small number of principal mode shapes are used in the FEA substructure approach (see, for example, Xing, Price & Du 1996).

In the following presentation of spatial distributions of time averaged power flow density vectors, figures 5.7-5.10 relate to a unit amplitude exciting force applied at position $x_e=0.75m$, $y_e=0.125m$ on plate I and this position of excitation is indicated by the symbol "+" in these figures. For clarity of presentation, the modulus of time averaged power flow density vectors in figures 5.7-5.10 are defined as

$$\left|\langle q(x,y)\rangle\right|^{(d)} = \left|\langle q(x,y)\rangle\right|^{0.2} = \left(\left|q_x(x,y)\right|^2 + \left|q_y(x,y)\right|^2\right)^{0.1}. \qquad (5.65)$$

Figure 5.7 illustrates the distribution of the time averaged power flow density vector at a frequency of 77.7 Hz. This corresponds to the first natural frequency of the system with one bending wave in both x and y directions in each plate. Figure 5.8 shows the corresponding vector distribution at a frequency of 124.1 Hz. This corresponds to the third natural frequency of the system with two bending waves in the x direction and one bending wave in the y direction of each plate. Figure 5.9 shows findings at a frequency of 201.4 Hz. These correspond to the 5th natural frequency of the system with three bending waves in the x direction and one bending wave in the y direction of each plate. Figure 5.10 shows results at a frequency of 263.8 Hz. These relate to the 7th natural frequency of the system with one bending wave occurring in the x direction and two bending waves in the y direction.

A L-shaped plate can be separated into two rectangular plates with a time and frequency dependent distributed moment excitation applied to the coupling edge of the two plates. This moment excitation together with the angular deformation represent the energy exchange between the two plates. As shown in figures 5.8-5.10, the energy does not always flow simply from source plate (plate I) to receiver plate (plate II), because in some parts along the coupling edge, energy flows from receiver to source plate. The direction of time averaged power flow is dependent on the phase angle between internal force and velocity response. This is demonstrated in figure 5.11 through illustration of the shapes of instantaneous bending moment, angular velocity and power flow occurring along the coupling edge of plate I at a frequency of 124.1 Hz. At any position on the coupling edge, when the phase angle between internal bending moment and angular velocity is less than 90°, the sign of the instantaneous power flow is negative and the direction of the rate of energy flow in a period is in a direction indicating energy absorption. Alternatively, if the phase angle is between 90° and 180°, the sign of the instantaneous power flow is positive and the direction of the rate of energy flow in a period is in a direction indicating an output of energy. The total power flowing in and out of the coupling edge remains balanced regardless of the number of plates combining at the coupling edge when the coupling is conservative. This is a mechanism similar to the one observed in Kirchhoff's law of electric current in that the summation of current flow into and out of a connection point is equal to zero.

The power flow in a L-shaped plate is not similar to the power flow in an infinite plate. Goyder & White (1980a) indicate that power flow under a single force excitation at any frequency propagates in the form of a cylindrical wave with decreasing amplitude as the distance from the driving force source increases. Power flow in a L-shaped plate under a single force excitation is frequency dependent and does not display simple cylindrical wave characteristics. The power flow density at a position near to the source is not necessarily always larger than its density at positions further away from the source. Power flows from the excitation source and usually ends at a boundary but there exists the possibility that the time averaged power flow density is equal to zero at positions in the plate and a circulation or vortex type flow exists in the vicinity of this position. Such flows are illustrated in figures 5.8-5.10.

Figures 5.12-5.15 illustrate the instantaneous power flow density vector at four different time instants of the first natural frequency at 77.7 Hz. The instantaneous power flow displays the characteristics of energy exchange between kinetic and potential energies. At instants *t=0* and *t=T/8* (figures 5.12, 5.13), both plates release energy and it is usual for power to flow from the peak value position of a modal shape to a boundary (i.e., the zero position of a modal shape). This peak value position acts similar to a power source. At instants *t=T/4* and *t=3T/8* (figures 5.14, 5.15), both plates absorb energy and there is no obvious power source. Power flows from boundary to the peak value position of the modal shape and this latter position behaves similar to a sink.

Compared to the displacement response, convergence of the calculated internal force (moment and shear force) and power flow density vector is very slow, especially for the moment excitation due to the abrupt changes of stress. The number of principal modes admitted in the present calculation relates to the highest eigenfrequency accepted in the analysis which is at least 150 times higher than the excitation frequency.

5.3.2. Rigidly Connected Coupling Edge

Figures 5.16, 5.17 illustrate the variation of the time averaged transmitted power flows with frequency to different assumed conditions at the coupling edge. An excitation is applied at the centre of plate *I* and results presented over the frequency range of 0-1500 Hz (figure 5.16) and 2000-4000 Hz (figure 5.17). The conditions at the coupling edge are: simply supported (i.e., the same as considered in figures 5.5, 5.6) and rigidly connected with plates at 45°, 90°, 135° and 165° to one another. Below 600 Hz, the results derived for all conditions are almost identical. The right angle set of predictions is similar to the simply supported case below the frequency of 4000 Hz which is about 0.7 times the value of the first natural frequency of in-plane vibration. This implies that the simply supported case assumption at the right angle coupling edge is valid below a frequency of 0.7 times the value of the first natural frequency of in-plane vibration. The influence of in-plane vibration increases as the angle between the two plates deviates from a right angle.

5.4. Application to a Corner Plate System

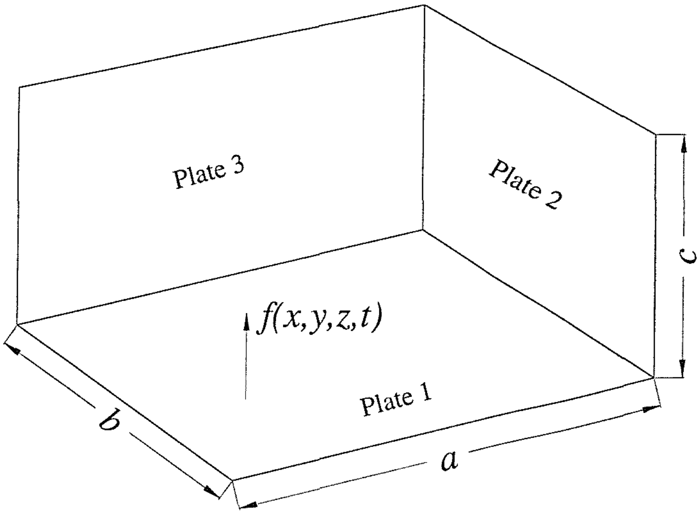

Figure 5.4. Schematic illustration of a corner plate system.

Figure 5.4 illustrates the corner plate system under investigation. The chosen parameters in the calculation are geometric sizes a = 1.0m, b = c = 0.5m, uniform thickness h=0.00635m, Young's modulus $E = 7.2\times10^{10} P_a$, Poisson ratio $\mu = 0.3$, mass density $\rho = 2710 kgm^{-3}$, damping loss factor $\eta = 0.01$.

Similar to the calculations described in the L-shaped plate example, a substructure approach is again used to calculate the power flow characteristics of the corner plate system. The four boundaries of each plate are assumed simply supported.

Figures 5.18 and 5.19 illustrate the variation of time averaged input power of external excitation and time averaged power dissipation in Plate I (I =1, 2, 3) under a unit external excitation force at the centre of the plate 1. The results derived by a FEA model are also included in figures 5.18 and 5.19. The FEA corner plate model consists of 2081 nodes and 2000 plate elements. One hundred natural frequencies and principal mode shapes were extracted using FEA package ANSYS spanning the frequency range up to approximately 2000 Hz. From the surface deflection data at each node, the spatial averaged surface squared velocity of each element was derived. The time averaged power dissipation of plate I, $\langle D_I \rangle$, (Cremer, *et al*, 1988) can be expressed as

$$\langle D_I \rangle \approx \omega\eta\rho abh\left|\overline{v_I^2}\right|, \tag{5.66}$$

where $\left|\overline{v_I^2}\right|$ denotes the spatial averaged squared velocity of the plate I (I=1,2,3). It is observed that only small differences exist between the theoretical substructure predictions and those evaluated by FEA model.

The three substructures of this corner plate system actually form *a delta power flow pattern* (see, 1.3.3) and this type of flow pattern cannot be determined sole by an energy balance analysis. For example, the energy balance conditions of the corner plate system under the external excitation at plate I are

$$\langle D_1 \rangle = \langle q_{in} \rangle - \langle q_{12} \rangle - \langle q_{13} \rangle, \tag{5.67}$$

$$\langle D_2 \rangle = \langle q_{12} \rangle - \langle q_{23} \rangle, \tag{5.68}$$

$$\langle D_3 \rangle = \langle q_{13} \rangle + \langle q_{23} \rangle, \tag{5.69}$$

where $\langle q_{in} \rangle$ is the time averaged external input power, $\langle q_{IJ} \rangle$ (I, J=1,2,3) denotes the power flow from plate I to plate J and

$$\langle q_{IJ} \rangle = -\langle q_{JI} \rangle \tag{5.70}$$

because the coupling is conservative.

These three energy balance equations (5.67)-(5.69) are not linearly independent because the determinant of the coefficient matrix formed from equations (5.67)-(5.69) gives

$$\begin{vmatrix} -1 & -1 & 0 \\ 1 & 0 & -1 \\ 0 & 1 & 1 \end{vmatrix} = 0. \tag{5.71}$$

Therefore, any quantity of power flow added will not affect the energy flow balance in equations (5.67)-(5.69). A global FEA model can be applied to calculate the power dissipation of each substructure but cannot derive power flow crossing the coupling edge of this corner plate system.

Figures 5.20-5.22 show the lines of time averaged power flow density vectors with frequencies of f=80.0, 130.8 and 211.3 Hz excited by a unit amplitude force applied at position $x_e=0.75m$, $y_e=0.125m$ on plate *1* respectively. This position of excitation is indicated by the symbol "+" in these figures. For clarity of presentation, the modulus of the time averaged power flow density vectors in figures 5.20-5.22 are defined in the same manner as given in equation (5.65).

Figure 5.20 illustrates the distribution of the time averaged power flow density vector at a frequency of 80.0 Hz. This corresponds to the first natural frequency of the system with one bending wave in both x and y directions in each plate. Figure 5.21 shows the corresponding vector distribution at a frequency of 130.8 Hz. This corresponds to the third natural frequency of the system with two bending waves in the x direction and one bending wave in the y direction of plates 1 and 3 and one bending wave in both x and y directions in plate 2. Figure 5.22 shows findings at a frequency of 211.3 Hz. These correspond to the 6th natural frequency of the system with three bending waves in the x direction and one bending wave in the y direction of plates 1 and 3 and two bending waves in the x direction and one bending wave in the y direction of plate 2.

As illustrated, power flows similarly to those previously described in the L-shaped plate system shown in figures 5.7-5.10. The corner of three plates is defined as a boundary point because of the basic boundary conditions, so its power density is zero and power flows around the corner of three plates creating a vortex type flow.

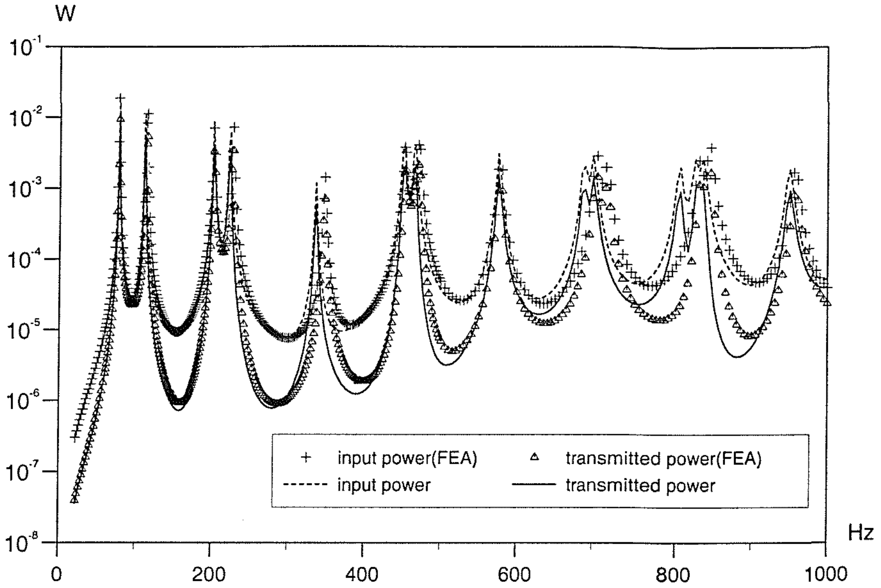

Figure 5.5. Results of time averaged input power and transmitted power flows (excitation at the centre of plate I).

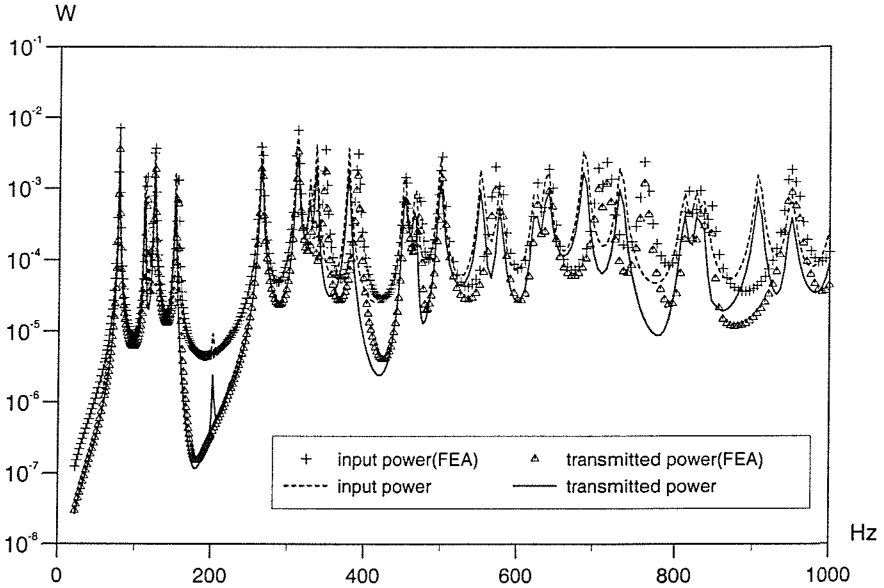

Figure 5.6. Results of time averaged input power and transmitted power flows (excitation at x_e=0.33m, y_e=0.125m of plate I).

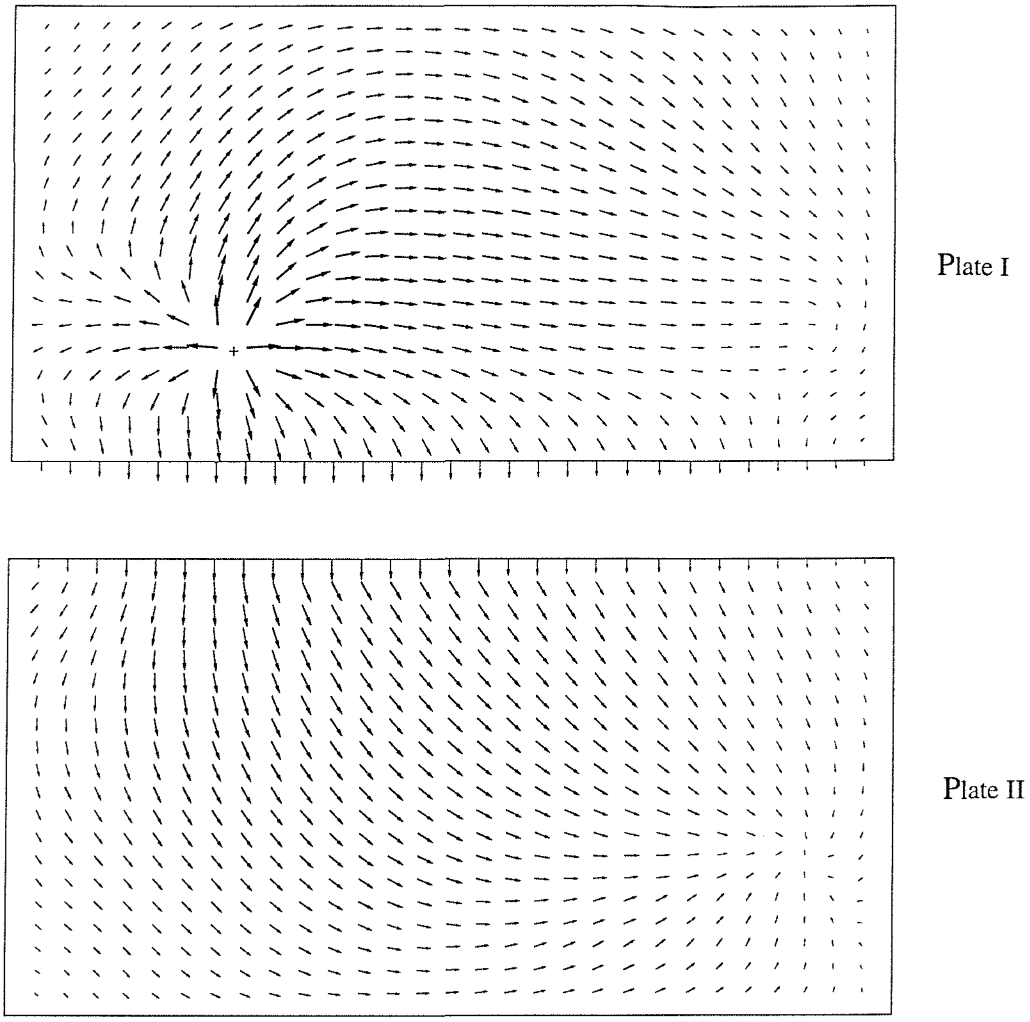

Figure 5.7. Time averaged power flow density vector in two plates, f=77.7 Hz. "+" indicates the excitation position.

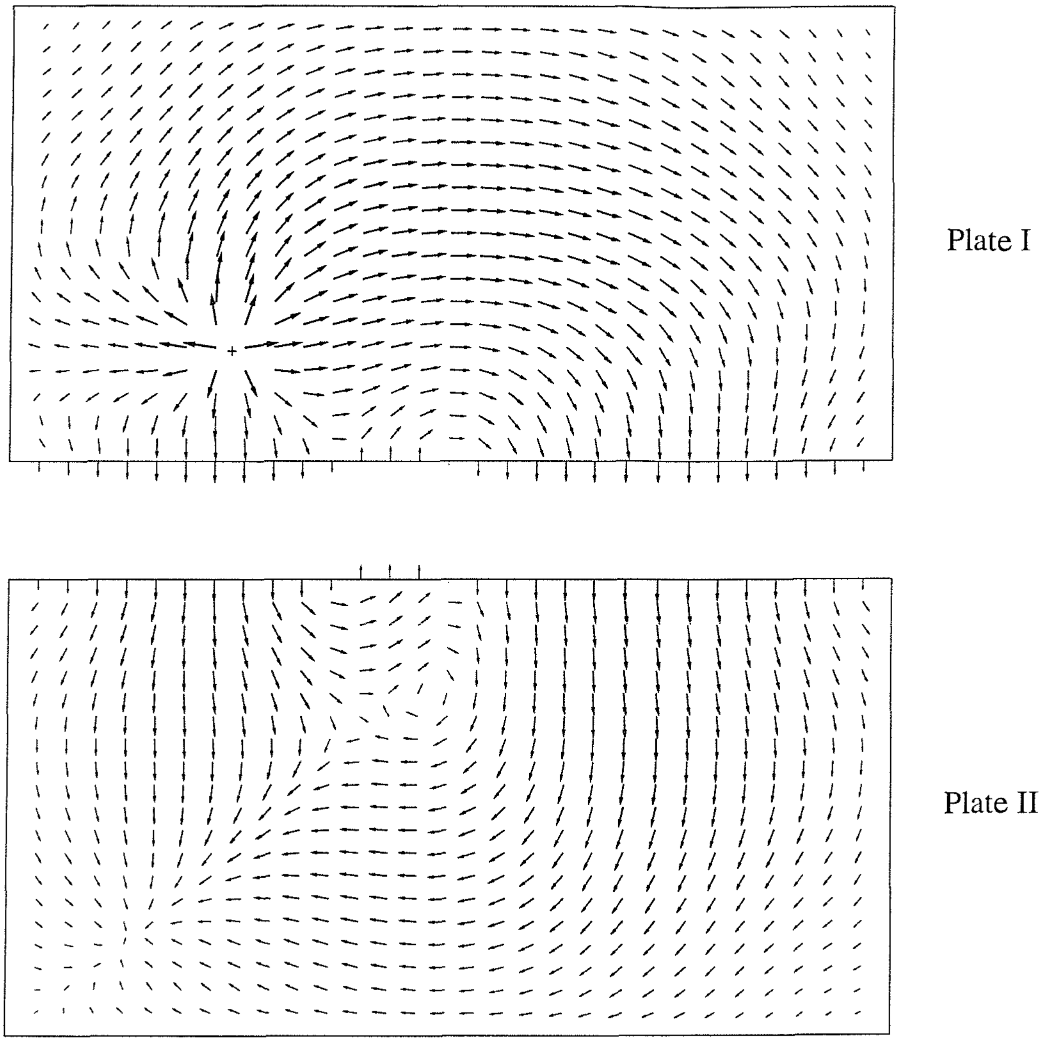

Figure 5.8. Time averaged power flow density vector in two plates, *f*=124.1 Hz. "+" indicates the excitation position.

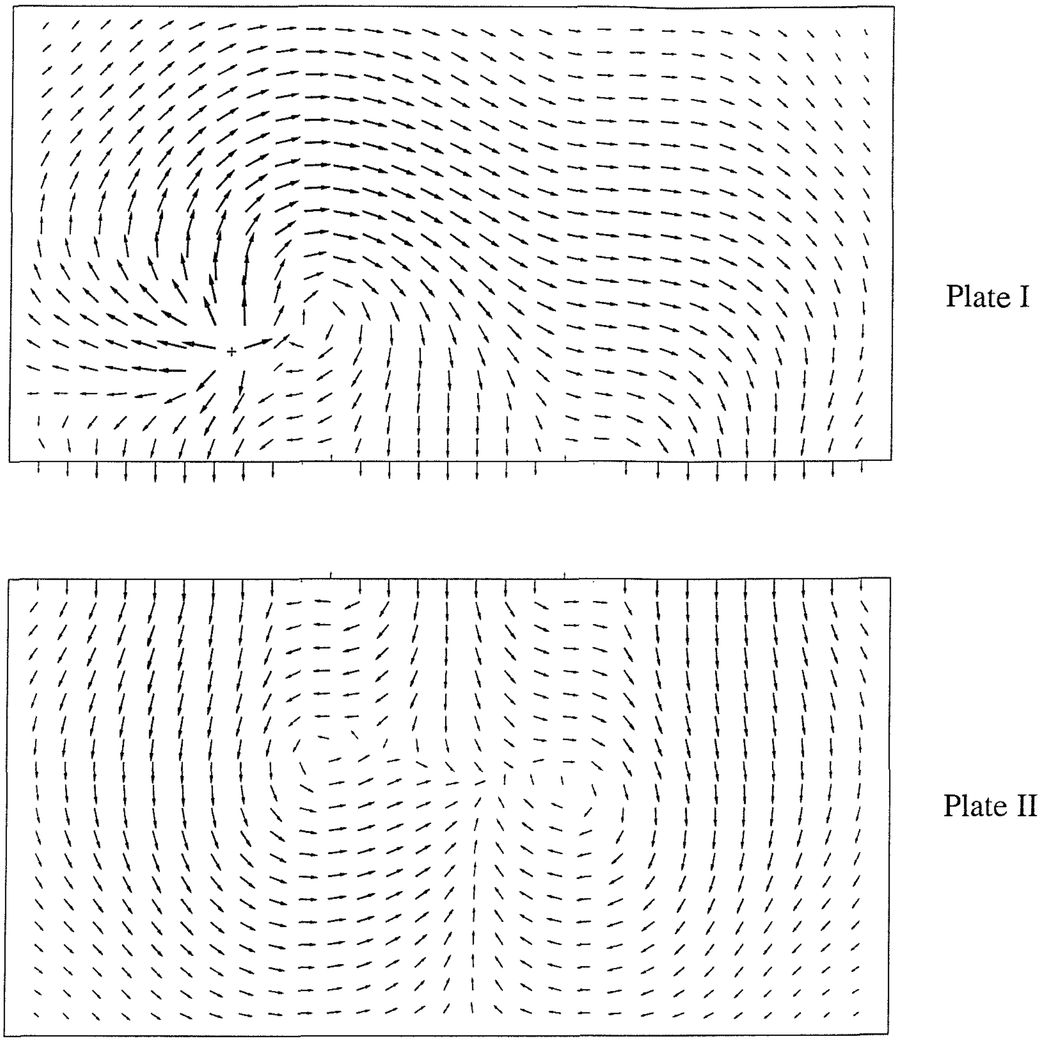

Figure 5.9. Time averaged power flow density vector in two plates, f=201.4 Hz. "+" indicates the excitation position.

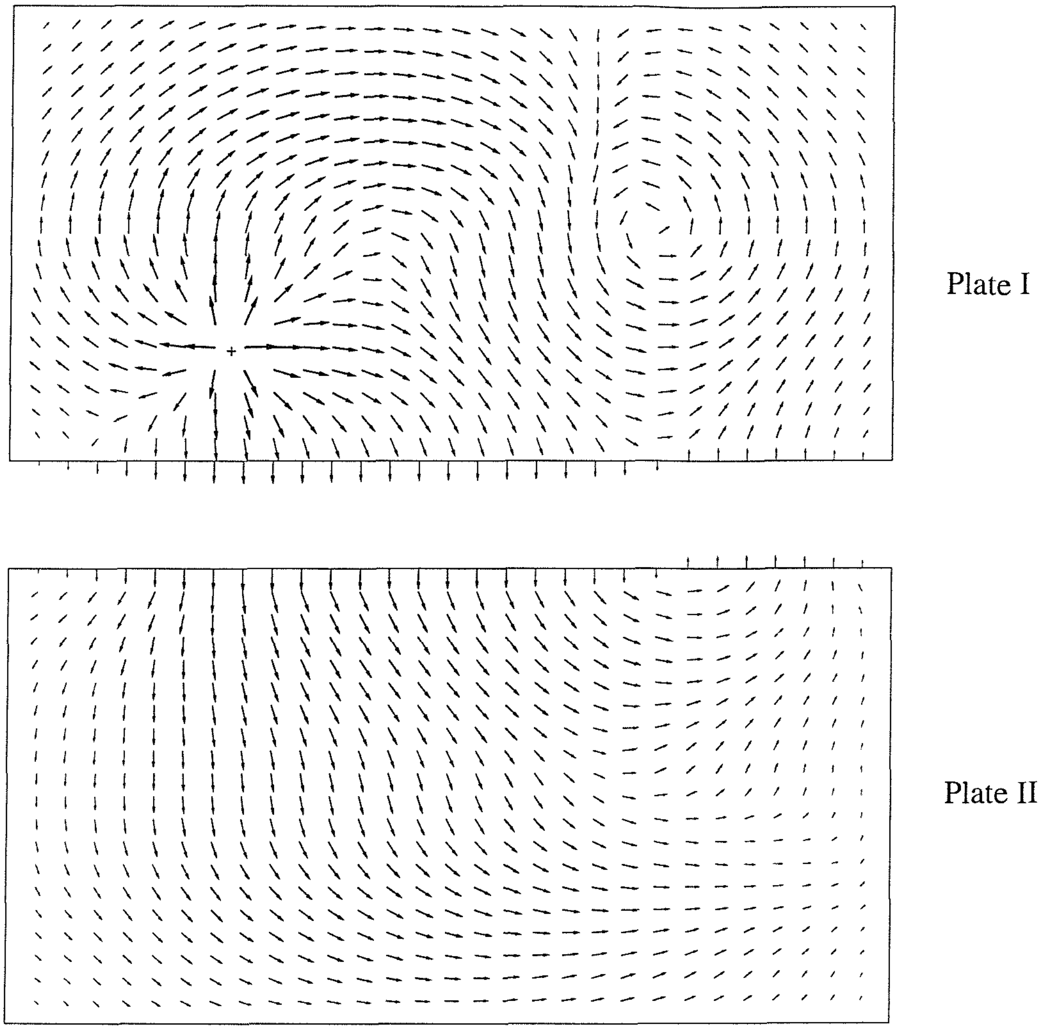

Figure 5.10. Time averaged power flow density vector in two plates, *f*=263.8 Hz. "+" indicates the excitation position.

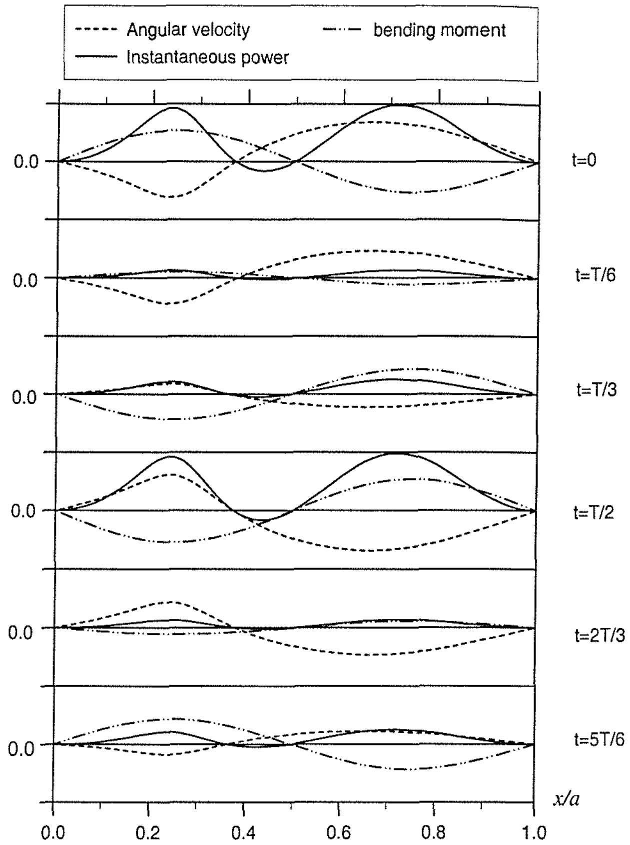

Figure 5.11. Shapes of instantaneous bending moment, angular velocity and transmitted power flow along the coupling edge of plate I at frequency of 124.1 Hz.

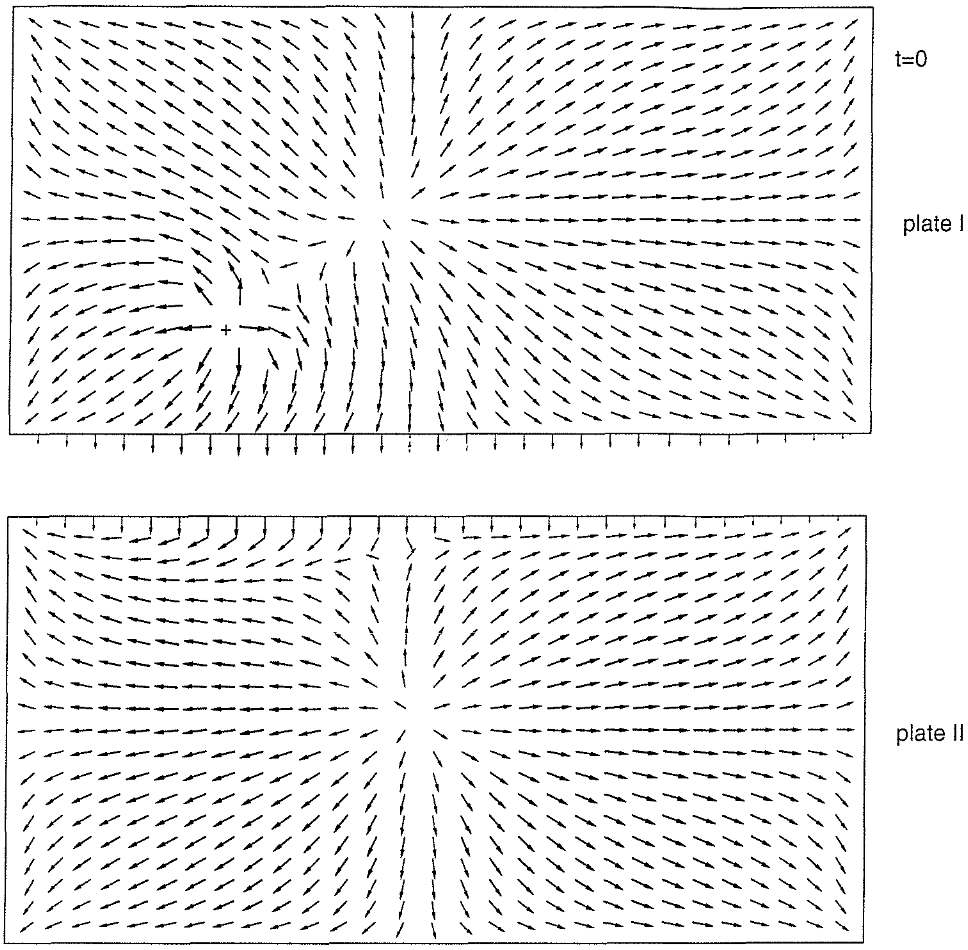

Figure 5.12. Instantaneous power flow density vector at *f*=77.7 Hz, t=0. "+" indicates the excitation position.

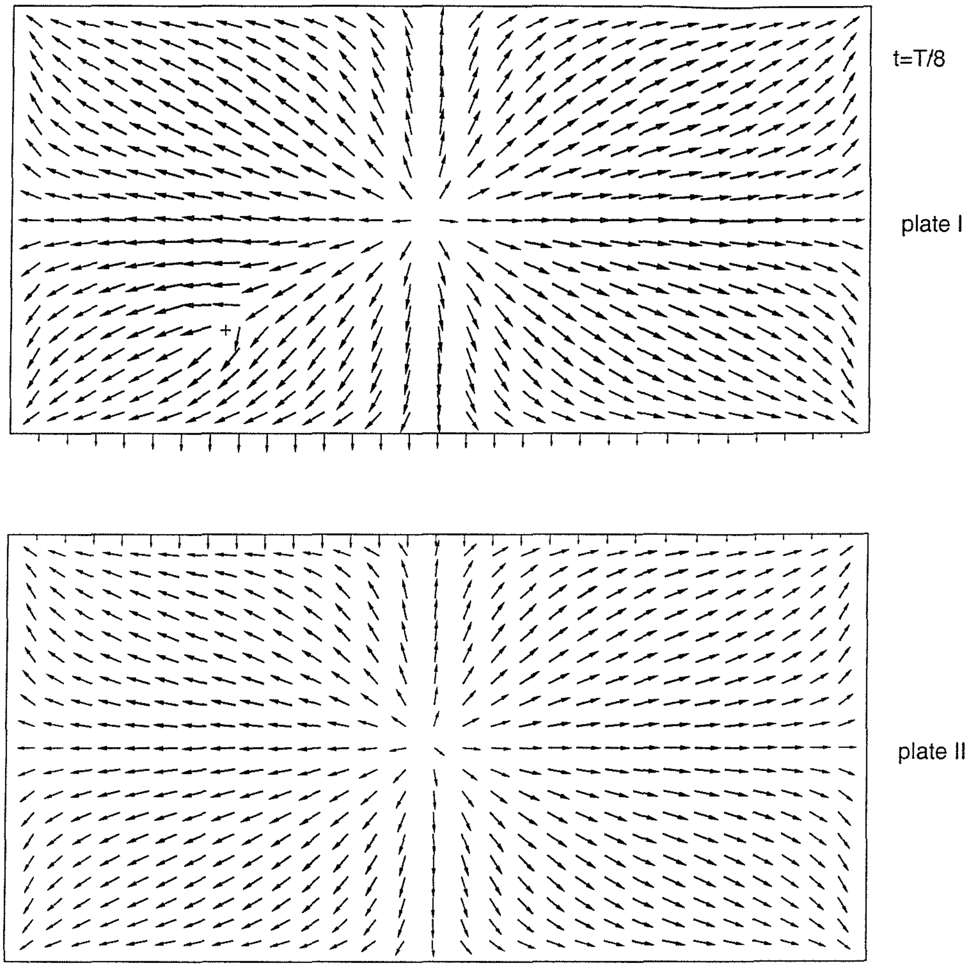

Figure 5.13. Instantaneous power flow density vector at *f*=77.7 Hz, *t*=*T*/8. "+" indicates the excitation position.

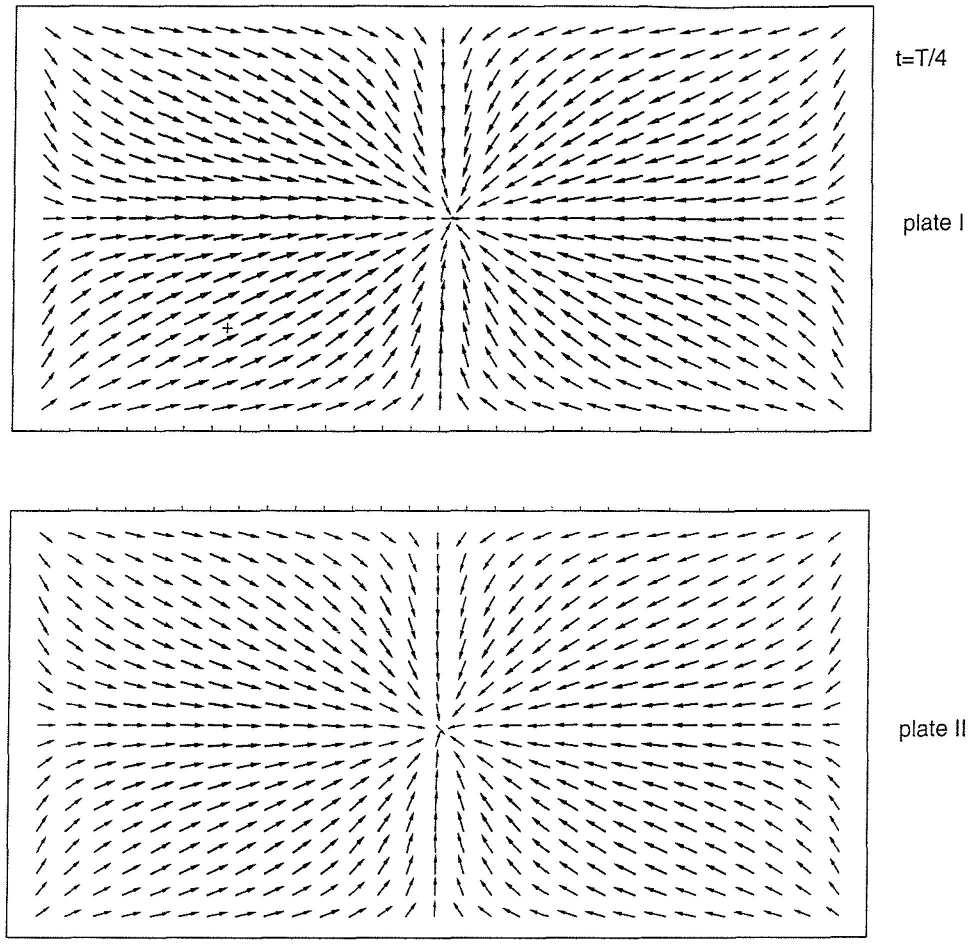

Figure 5.14. Instantaneous power flow density vector at f=77.7 Hz, $t=T/4$. "+" indicates the excitation position.

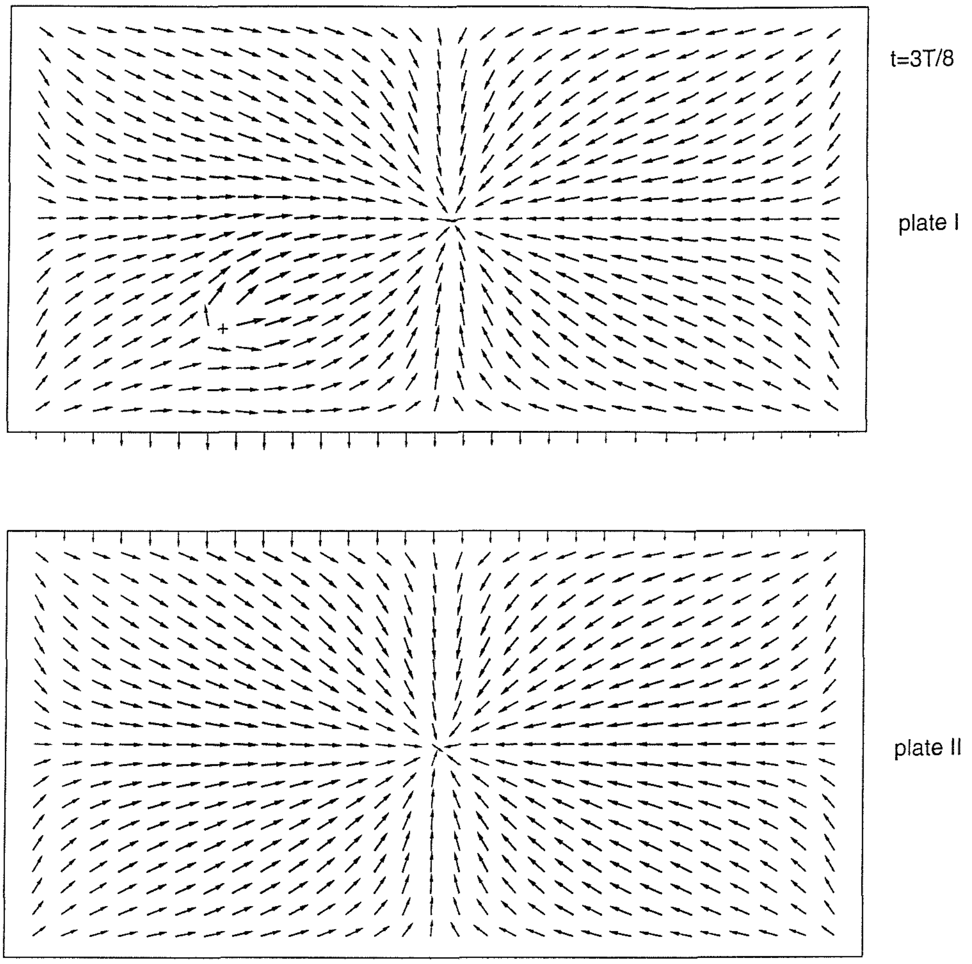

Figure 5.15. Instantaneous power flow density vector at *f*=77.7 Hz, t=*3T/8*. "+" indicates the excitation position.

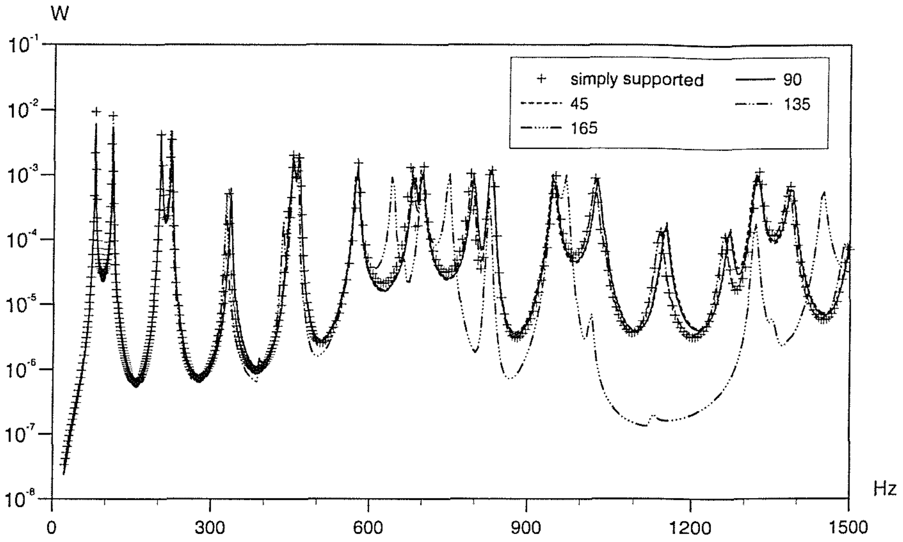

Figure 5.16. The variation with frequency of time averaged transmitted power for different coupling angle (0-1500Hz).

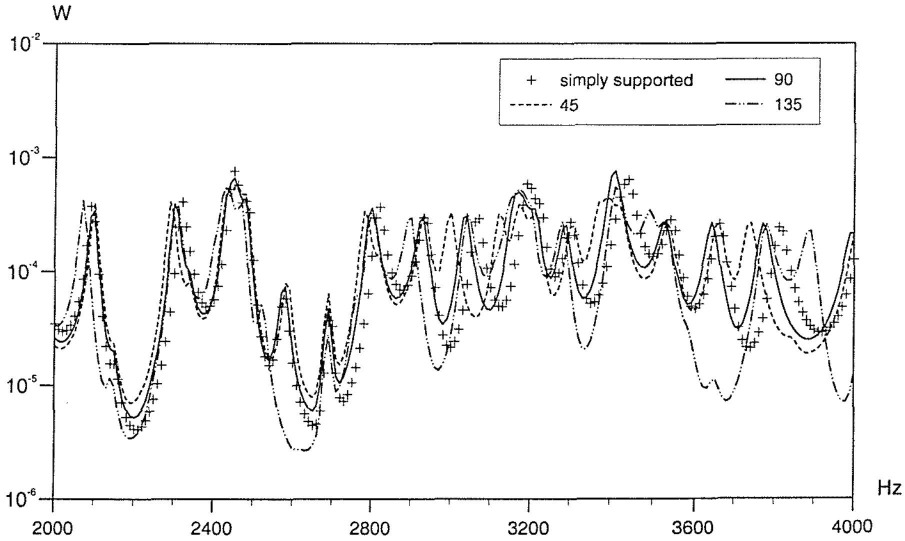

Figure 5.17. The variation with frequency of time averaged transmitted power for different coupling angle (2000-4000Hz).

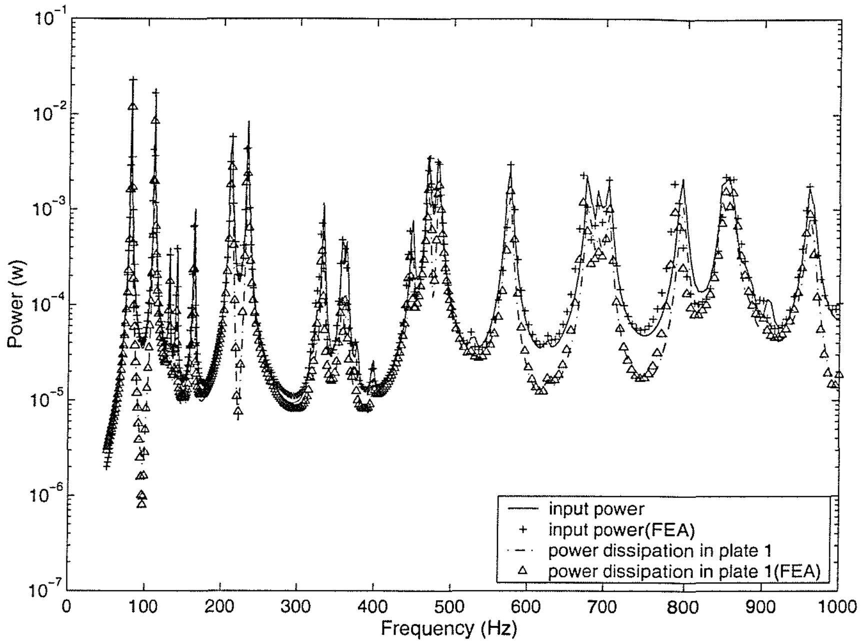

Figure 5.18. Results of time averaged external input power and power dissipation in plate 1 (excitation at the centre of plate I).

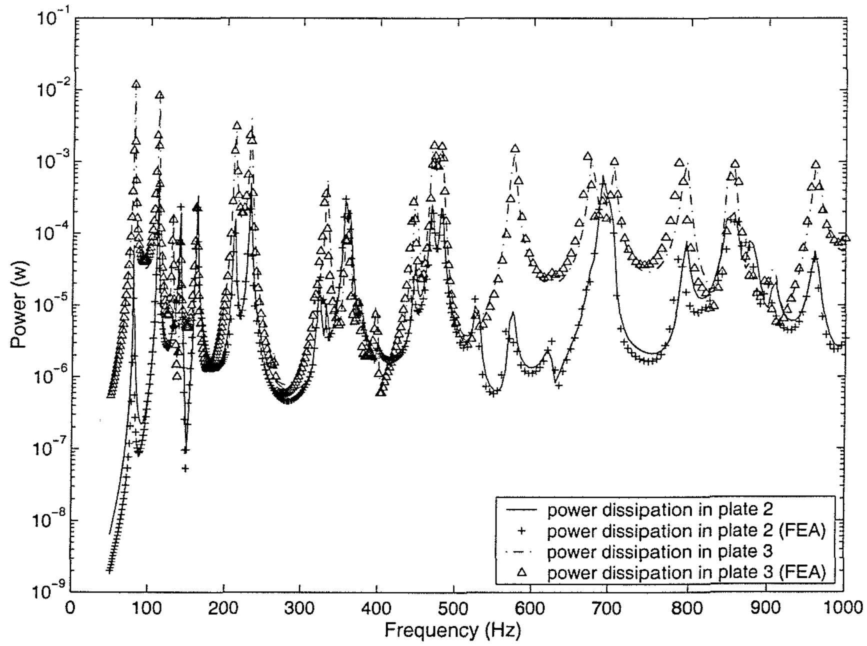

Figure 5.19. Results of time averaged power dissipation in plate 2 and 3 (excitation at the centre of plate I).

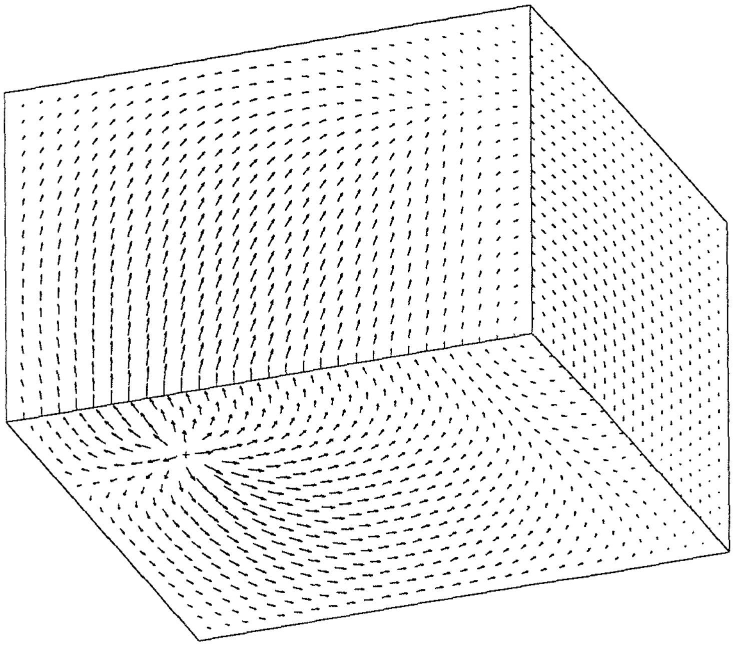

Figure 5.20. Time averaged power flow density vector in the system, *f*=80.0 Hz. "+" indicates the excitation position.

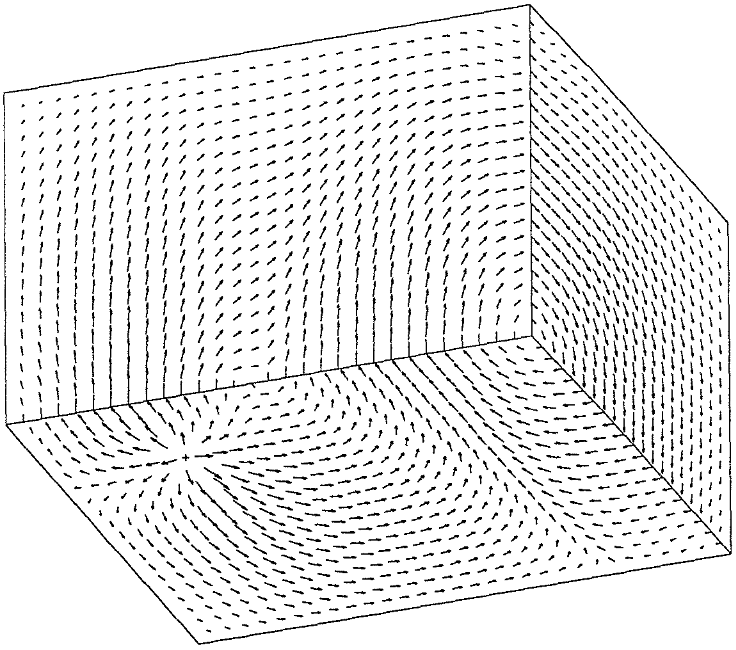

Figure 5.21. Time averaged power flow density vector in the system, *f*=130.8 Hz. "+" indicates the excitation position.

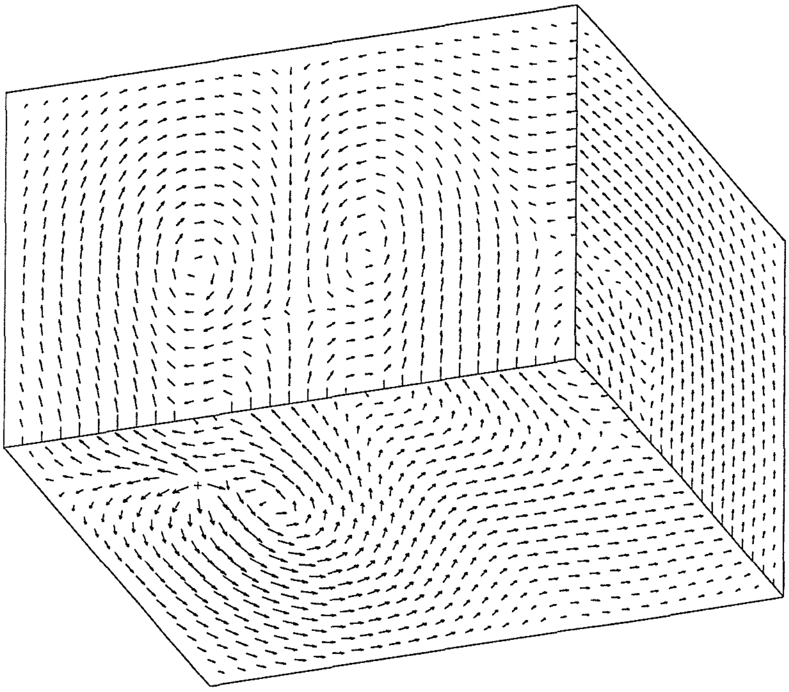

Figure 5.22. Time averaged power flow density vector in the system, *f*=211.3 Hz. "+" indicates the excitation position.

6. POWER FLOWS ANALYSIS OF A BEAM-STIFFENED PLATE

In this chapter, the power flow characteristics of a beam-stiffened plate, shown in figure 6.1, is studied and discussed. It is a typical segment of a beam-stiffened plate system, which is used widely in many engineering structures such as ships, aircraft, etc.

6.1. Substructure Analysis of a Beam-Stiffened Plate

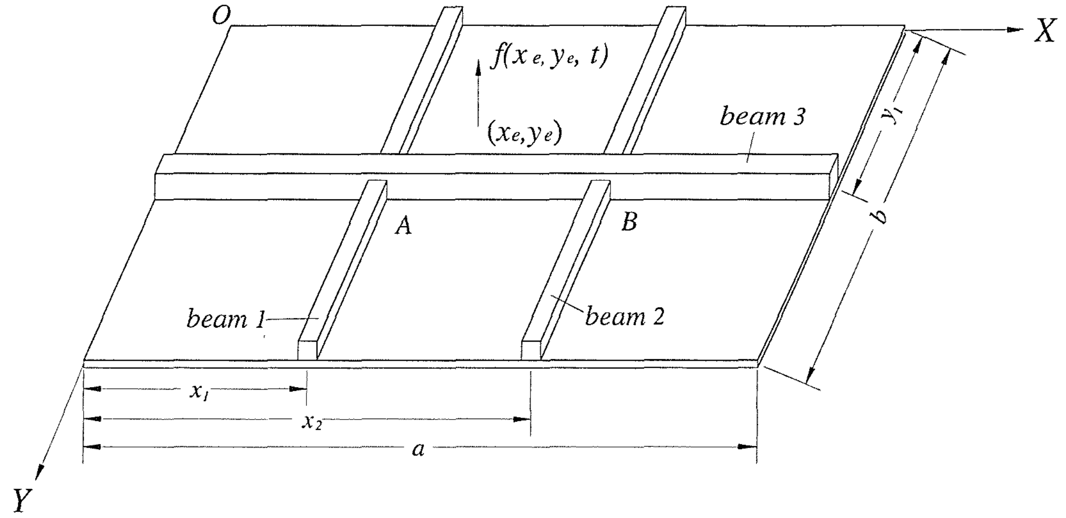

Figure 6.1. Schematic illustration of a beam-stiffened plate.

In a substructure approach, the beam-stiffened plate shown in figure 6.1 can be separated into four substructures, a rectangular plate and three beams. Here, we treat the rectangular plate as a uniform plate with length a, width b and each beam as a uniform beam with length l_j, cross-section area A_j, moment of inertia about x, y axes I_{xj}, I_{yj} and polar moment of inertia J_j (j=1,2,3). All edges of the plate and the two ends of each beam are assumed simply supported. The material properties of all four substructures are mass density ρ, Young's modulus E and the structural damping properties are represented by a linear Voigt viscoelastic model with hysteretic damping or loss factor η.

Beams *1* and *2* are coupled with the plate at $x=x_1$ and $x=x_2$. Beam 3 is coupled with the plate at $y=y_1$. A harmonic external exciting force is applied at point (x_e, y_e) on the plate or at any positions on the beams.

Two types of forces act on each substructure. One is the external excitation force whereas the other is the internal distributed coupling force acting at the coupling edge. The receptance functions of the plate and three beams under both external and internal force can be determined theoretically using the same methods as those described in Chapters 4 and 5. The whole system is coupled by the distributed internal forces of transverse shear force, bending moment and twisting moment along the three coupling lines of each subsystem. There exists in-plane force components along the *X*, *Y* axes and a twist moment component around the *Z* axis at the interfaces between the plate and beams. However, under the small deflection assumption, the bending vibration and in-plane vibration of the plate or beam are uncoupled. Therefore, in-plane force components along the *X*, *Y* axes and the twisting moment component around the *Z* axis can be neglected when the external exciting forces are applied only in the *Z* direction.

The internal force vector $\left[\tilde{f}_{B1}^{c}\right]=\left[\tilde{Q},\tilde{M}_x,\tilde{M}_y\right]^T$ and the relative displacement vector $\left[\tilde{u}_{B1}^{c}\right]=\left[\tilde{u}_z,\tilde{\theta}_x,\tilde{\theta}_y\right]^T$ of beam *1* at the coupling line $x=x_1$ in the local beam co-ordinate axis reference system are balanced and are compatible with the internal force vector $\left[\tilde{f}_{p,x1}^{c}\right]$ and displacement vector $\left[\tilde{u}_{p,x1}^{c}\right]$ of the plate in the global co-ordinate system (as shown in figure 6.1) and expressed as

$$[Tr]\left[\tilde{f}_{B1}^{c}\right]+\left[\tilde{f}_{p,x1}^{c}\right]=0, \tag{6.1}$$

and

$$[Tr]\left[\tilde{u}_{B1}^{c}\right]=\left[\tilde{u}_{p,x1}^{c}\right] \tag{6.2}$$

where

$$[Tr]=\begin{bmatrix}1 & 0 & 0\\ 0 & 0 & -1\\ 0 & 1 & 0\end{bmatrix}. \tag{6.3}$$

The coupling relationships between beam *2* and the plate are exactly the same as defined in equations (6.1), (6.2) but the coupling relationships between beam *3* and the plate are slightly different because the local co-ordinate system of beam 3 is the same as the global co-ordinate system. Therefore, these relationships can be expressed as

$$\left[\tilde{f}^{c}_{B3}\right]+\left[\tilde{f}^{c}_{p,y1}\right]=0, \tag{6.4}$$

and

$$\left[\tilde{u}^{c}_{B3}\right]=\left[\tilde{u}^{c}_{p,y1}\right]. \tag{6.5}$$

There exists two special points *A*, *B* (shown in figure 6.1) because beam *3* is connected to beam *1* and 2. The coupling relationships at point *A* are

$$[Tr]\left[\tilde{f}^{c}_{B1,y1}\right]+\left[\tilde{f}^{c}_{B3,x1}\right]+\left[\tilde{f}^{c}_{p,x1,y1}\right]=0, \tag{6.6}$$

and

$$[Tr]\left[\tilde{u}^{c}_{B1,y1}\right]=\left[\tilde{u}^{c}_{B3,x1}\right]=\left[\tilde{u}^{c}_{p,x1,y1}\right], \tag{6.7}$$

where $\left[\tilde{f}^{c}_{B1,y1}\right]$, $\left[\tilde{u}^{c}_{B1,y1}\right]$ denote the internal force and displacement vectors of beam *1* at the position of the local co-ordinate $x=y_1$. $\left[\tilde{f}^{c}_{B3,x1}\right]$, $\left[\tilde{u}^{c}_{B3,x1}\right]$ have similar definitions to $\left[\tilde{f}^{c}_{B1,y1}\right]$, $\left[\tilde{u}^{c}_{B1,y1}\right]$ and $\left[\tilde{f}^{c}_{p,x1,y1}\right]$, $\left[\tilde{u}^{c}_{p1,x1,y1}\right]$ denote the internal force and displacement vectors of the plate at position $x=x_1$, $y=y_1$. The coupling relationships at point *B* are similar to those at point *A* as defined by equations (6.6), (6.7).

The substitution of the receptance functions of the beam as given in (4.24), (4.51) and those of the plate are expressed in equations (5.44)-(5.46) into equations (6.2), (6.5) and (6.7) yields a homogeneous set of linear algebraic equations for the coupling forces along the three coupling lines. It therefore follows that the response of the whole system can be determined after solution of the receptance functions of a single substructure.

6.2. Power Flow Density Vectors

The instantaneous power flow density vector and its time averaged value over a period of external excitation in a thin plate is the same as the relations expressed in equations (5.55)-(5.58). The instantaneous power flow density vector and its time averaged value in a beam differ from those stated in equations (4.53) and (4.54) because of the contribution of the twisting moment component. The instantaneous power flow density vector at position x in the local co-ordinate system in the beam is given by

$$q(x,t) = -\mathrm{Re}\left\{\dot{\tilde{u}}_z(x,t)\right\}\mathrm{Re}\left\{\tilde{Q}(x,t)\right\} + \mathrm{Re}\left\{\dot{\tilde{\theta}}_y(x,t)\right\}\mathrm{Re}\left\{\tilde{M}_y(x,t)\right\} - \mathrm{Re}\left\{\dot{\tilde{\theta}}_x(x,t)\right\}\mathrm{Re}\left\{\tilde{M}_x(x,t)\right\} \tag{6.8}$$

with its time averaged value over a period of excitation T

$$\langle q(x,t)\rangle = -\frac{1}{2}\left(\mathrm{Re}\left\{\dot{\tilde{u}}_z(x,t)^*\tilde{Q}(x,t)\right\} - \mathrm{Re}\left\{\dot{\tilde{\theta}}_y(x,t)^*\tilde{M}_y(x,t)\right\} + \mathrm{Re}\left\{\dot{\tilde{\theta}}_x(x,t)^*\tilde{M}_x(x,t)\right\}\right). \tag{6.9}$$

The transmitted power between the plate and any beam is given by the product of the coupling force and the velocity along the coupling line. That is,

$$q_{trans} = \mathrm{Re}\left\{\left[\tilde{f}^c_{Bj}\right]\right\} \cdot \mathrm{Re}\left\{\left[\tilde{u}^c_{Bj}\right]^T\right\} \tag{6.10}$$

with corresponding time averaged quantity,

$$\langle q_{trans}\rangle = \int_0^T q_{trans}dt\,. \tag{6.11}$$

For illustrative purposes, a power flow analysis of a beam-stiffened plate is investigated.

6.3. Application to a Beam-Stiffened Plate

Figure 6.1 illustrates a beam-stiffened plate under examination. The system shown in figure 6.1 is defined by the data set:

$\rho = 2710\,kg/m^3$, $E = 72\,GPa$, $\eta = 0.01$, $\mu = 0.3$;

$a=1.0\,m$, $b = 0.5\,m$, $h=0.00635\,m$;

$x_1=0.3m$, $x_2=0.7m$, $y_1=0.25m$; $A_1=A_2=A_3=1.5875\times10^{-4}m^2$;

$I_{x1}=I_{x2}=I_{x3}= I_{y1}=I_{y2}=I_{y3}=8.27\times10^{-9}m^4$, $J_1=J_2=J_3=8.8\times10^{-9}m^4$.

Figures 6.2 and 6.3 illustrate the variation of the time averaged input power and transmitted power flowing from the plate to the beams with frequency caused by a unit amplitude loading applied at the centre of the plate. The results derived by a FEA model are also included in figures 6.2 and 6.3. The FEA model of the beam-stiffened plate consists of 861 nodes, 400 plate elements and 80 beam elements (20 elements for beam 1 and 2 respectively, 40 elements for beam 3). Forty natural frequencies and principal mode shapes were extracted using FEA package ANSYS spanning the frequency range up to about 2000 Hz. From the deflection data at each beam node, the spatial averaged squared velocity of each beam element was derived. The time averaged power dissipation $\langle D_I \rangle$ of the beam *I* as given by Cremer, *et al* (1988) is

$$\langle D_I \rangle \approx \omega \eta \rho A_I x_I \left| \overline{v_I^2} \right|, \qquad (6.12)$$

where $\left| \overline{v_I^2} \right|$ denotes the spatial averaged squared velocity of beam *I* (*I*=1,2,3). It is observed that only small differences exist between the theoretical substructure predictions and those evaluated by the FEA model. Because each beam of the system is only connected to the plate except at the cross points *A* and *B* (see, figure 6.1), the time averaged power dissipation of each beam is approximately equal to the power transferred from the plate to the beam. It is observed in figures 6.2, 6.3 that the theoretical substructure predictions and those evaluated by the FEA approach produce almost same results for the time averaged input power generated by the external excitation but small differences arise for the transmitted power flows from plate to beams. This is because each beam is connected not only to the plate but also to another beam at a point. Therefore a small part of power is transferred between the beams. It is difficult to evaluate this portion of power transmitted using energy balance equations in a global FEA model as previously undertaken when examining the corner plate system in **5.4**.

In the following presentation of spatial distributions of time averaged power flow density vectors, figures 6.4-6.8 relate to a unit amplitude exciting force applied at position x_e=*0.4m*, y_e=*0.15m* on the plate and this position of excitation is indicated by the symbol “x” in these figures. For clarity of presentation, the modulus of the time averaged power flow density vectors in figures 6.4-6.8 are defined in a similar manner presented in equation (5.65).

Figure 6.4 illustrates the distribution of the time averaged power flow density vector at a frequency of 92.9 Hz. This corresponds to the first natural frequency of the system with one bending wave in both x and y directions present in the system. Figure 6.5 shows the corresponding vector distribution at a frequency of 147.7 Hz. This corresponds to the second natural frequency of the system with two bending waves existed in the x direction and one bending wave present in the y direction. Figure 6.6 shows findings at a frequency of 253.3 Hz. This corresponds to the third natural frequency of the system with three bending waves existed in the x direction and one bending wave present in the y direction. Figure 6.7 shows results at a frequency of 330.3 Hz. This relates to the 4th natural frequency of the system with one bending wave occurring in the x direction and two bending waves existed in the y direction. Figure 6.8 shows results at a frequency of 392.8 Hz. This relates to the 5th natural frequency of the system with two bending waves occurring in the both x and y directions.

The basic features of time averaged power flow arising in the beam-stiffened plate are similar to those previously described in a plate as discussed in chapter 5. The stiffened beam can absorb and transfer power, this produces some special features in the beam stiffened-plate. It is observed in figures 6.4 and 6.5 that there exist obvious differences in the amplitudes or directions of power flow densities on both sides of beam 1 under the exciting frequencies f=92.9 and 147.7 Hz. If the whole system is divided into six regions, as shown in figure 6.9, the amplitudes of power flow densities alongside beam 1 in region 2 (i.e., excitation region) are much larger than those values alongside beam 1 in region 1. This means some energy is transferred from the plate to beam 1. Opposite directions of power flow densities on both sides of beam 1 in regions 4 and 5 are observed in figures 6.4 and 6.5. This means that beam 1 releases energy to the plate in this area. This phenomena can also be observed in the distribution of time averaged transmitted power along beam 1 as shown in figure 6.10 under the same excitation as used in figures 6.4 and 6.5. It is observed in figure 6.10 that almost half of the beam absorbs energy, the other releases energy. The stiffened beam in the system absorbs energy from the plate in some areas. This absorbed energy can be separated into two parts — the one is dissipated by beam damping and the other transmitted along the beam and released to other areas of the plate.

Figures 6.11-6.13 illustrate the spatial distributions of time averaged power flow density vectors under a unit amplitude exciting force applied at position $x_e=0.3m$,

$y_e=0.25m$ at the beam cross point *A* (see, figure 6.1) of beams 1 and 3. The position of excitation is indicated by the symbol "x" in these figures. Figure 6.11 illustrates the distribution of time averaged power flow density vector at a frequency of 92.9 Hz. Figure 6.12 shows the corresponding vector distribution at a frequency of 147.7 Hz. Figure 6.13 shows findings at frequency 253.3 Hz. Figures 6.14 and 6.15 illustrate the distributions of time averaged transmitted power between the plate and beams 1 and 3.

It is observed from figures 6.11-6.13 that the amplitudes of power flow density vectors in beams 1 and 3 are much larger than those in the plate. This means beams 1 and 3 are the main transmitted paths of power flow in the whole system. The results shown in figures 6.14 and 6.15 also indicate this phenomena. Apart from the position of the external exciting input power, almost all portions of beams 1 and 3 release energy to the plate. This implies that power flows from the external excitation to sections of the beam and it is further released to the plate.

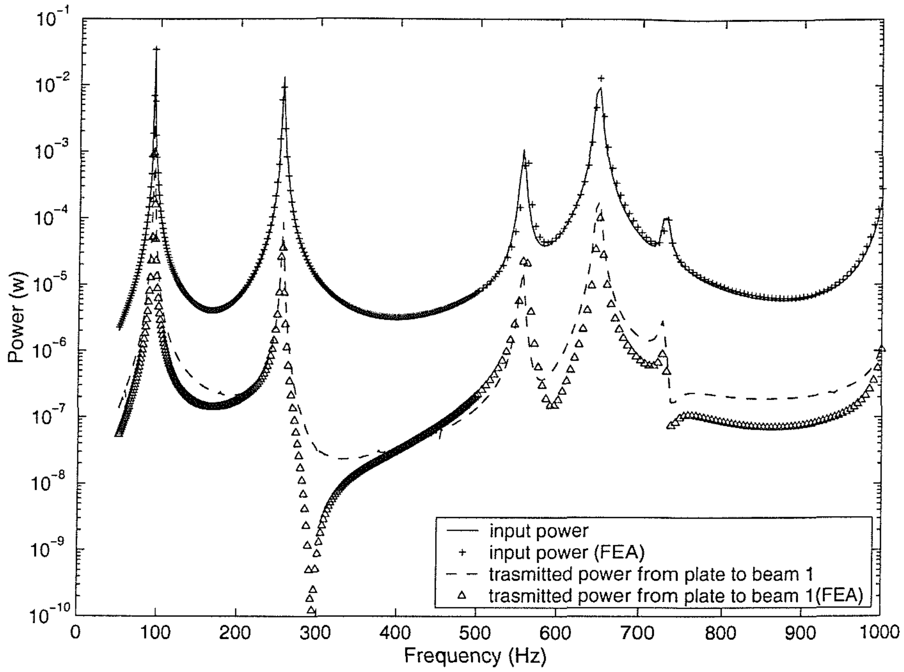

Figure 6.2. Results of time averaged input power and transmitted power flows from plate to beam 1 (excitation at the centre of plate).

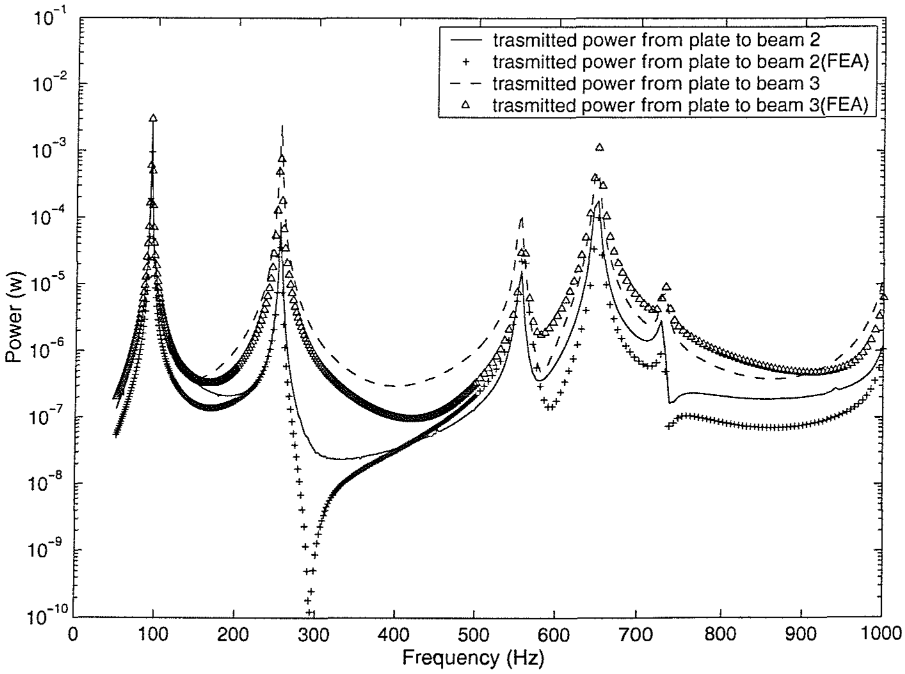

Figure 6.3. Results of time averaged transmitted power flows from plate to beam 2 and beam 3 (excitation at the centre of plate).

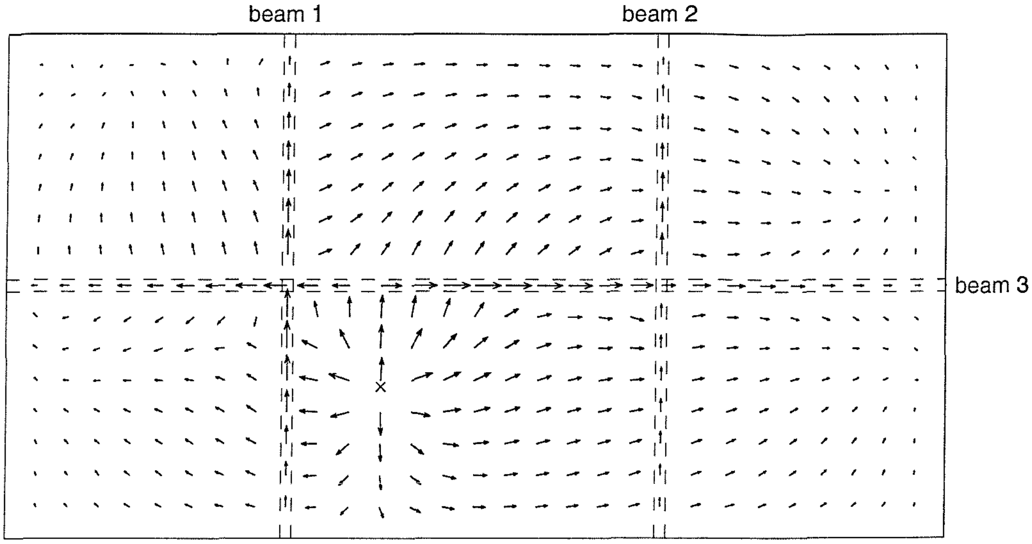

Figure 6.4. Time averaged power flow density vector in the beam-stiffened plate, *f*=92.9 Hz. "×" indicates the excitation position at the plate.

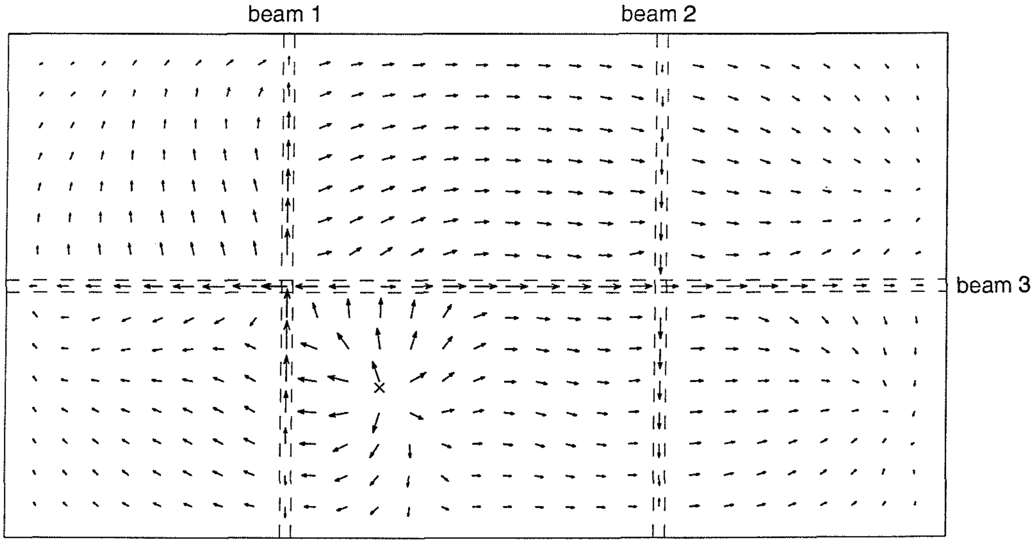

Figure 6.5. Time averaged power flow density vector in the beam-stiffened plate, *f*=147.7 Hz. "×" indicates the excitation position at the plate.

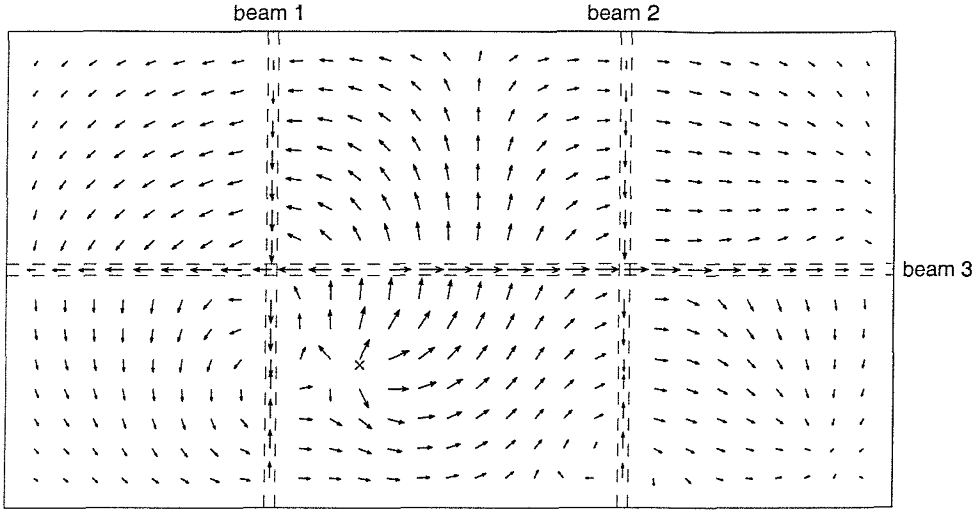

Figure 6.6. Time averaged power flow density vector in the beam-stiffened plate, *f*=253.3 Hz. "×" indicates the excitation position at the plate.

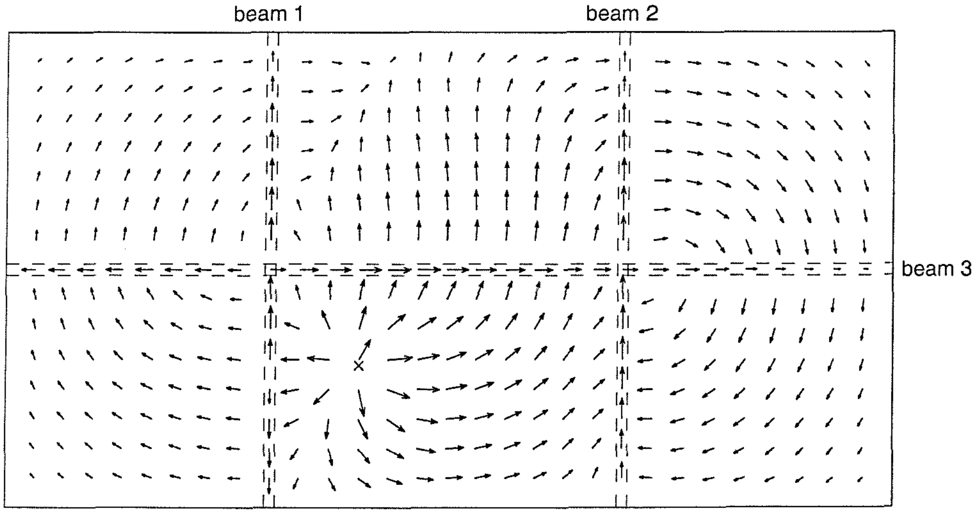

Figure 6.7. Time averaged power flow density vector in the beam-stiffened plate, *f*=330.3 Hz. "×" indicates the excitation position at the plate.

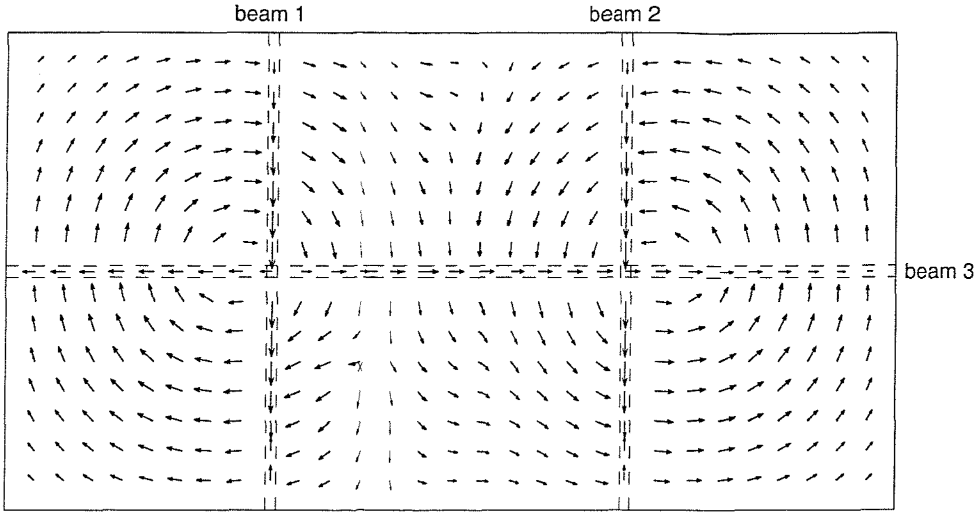

Figure 6.8. Time averaged power flow density vector in the beam-stiffened plate, f=392.8 Hz. "x" indicates the excitation position at the plate.

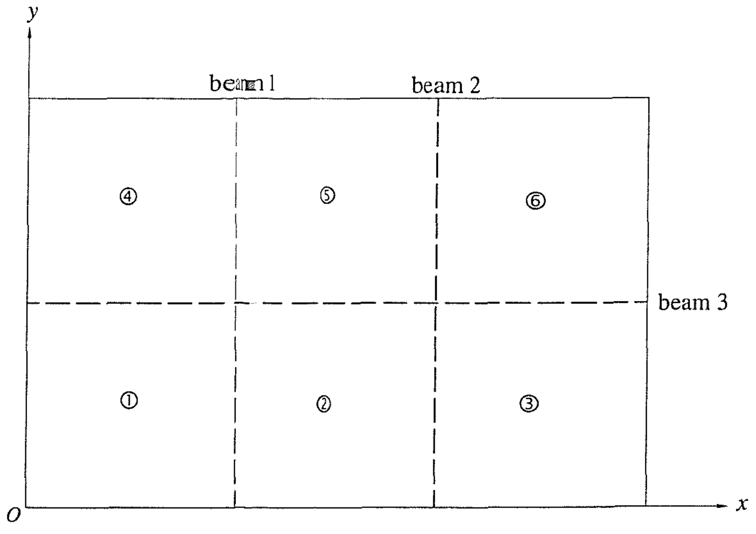

Figure 6.9. Schematic illustration of six regions of the beam-stiffened plate.

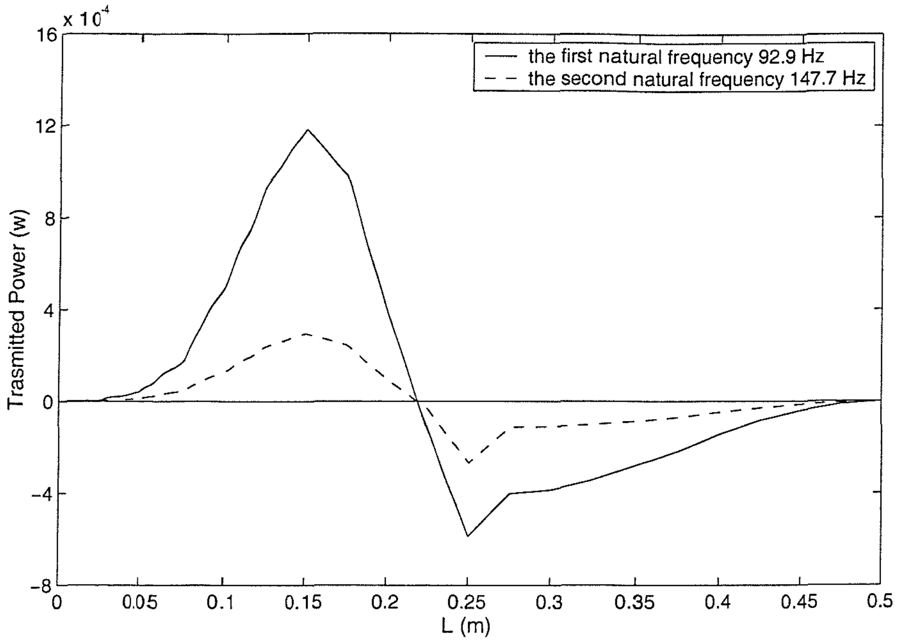

Figure 6.10. Time averaged power transmitted from the plate to beam 1, negative value means the power transmitted from beam 1 to the plate.

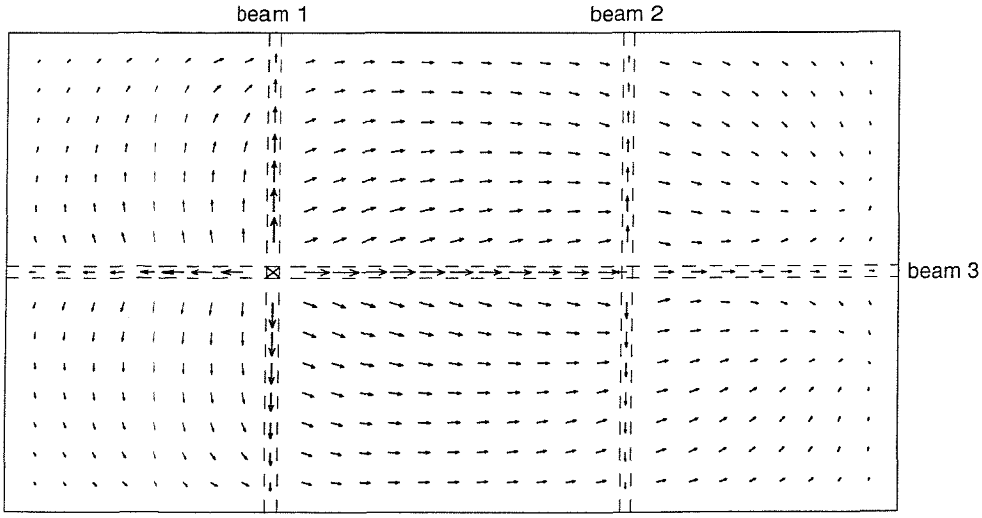

Figure 6.11. Time averaged power flow density vector in the beam-stiffened plate, *f*=92.9 Hz. "x" indicates the excitation position at the connection point *A* of beam *1* and beam *3*.

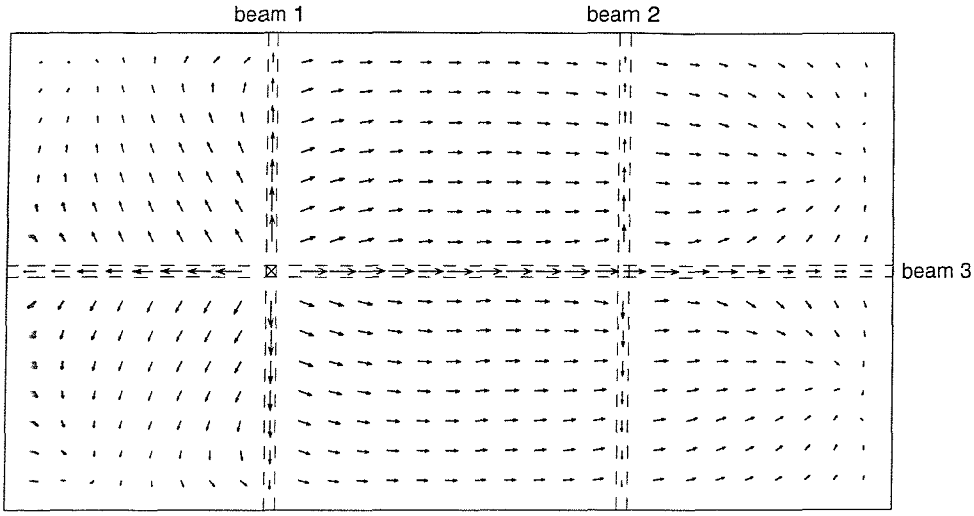

Figure 6.12. Time averaged power flow density vector in the beam-stiffened plate, *f*=147.7 Hz. '"x" indicates the excitation position at the connection point *A* of beam *1* and beam *3*.

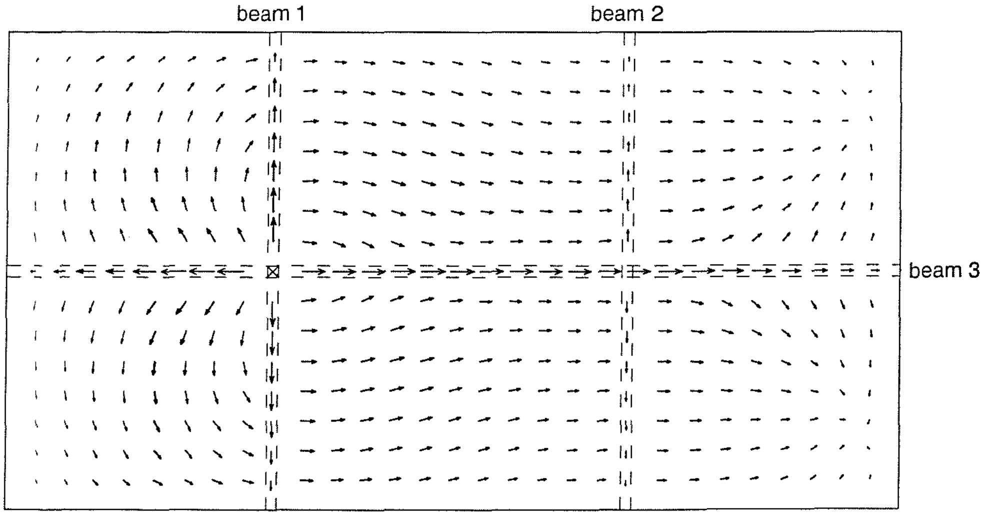

Figure 6.13. Time averaged power flow density vector in the beam-stiffened plate, *f*=253.3 Hz. "x" indicates the excitation position at the connection point *A* of beam*1* and beam *3*.

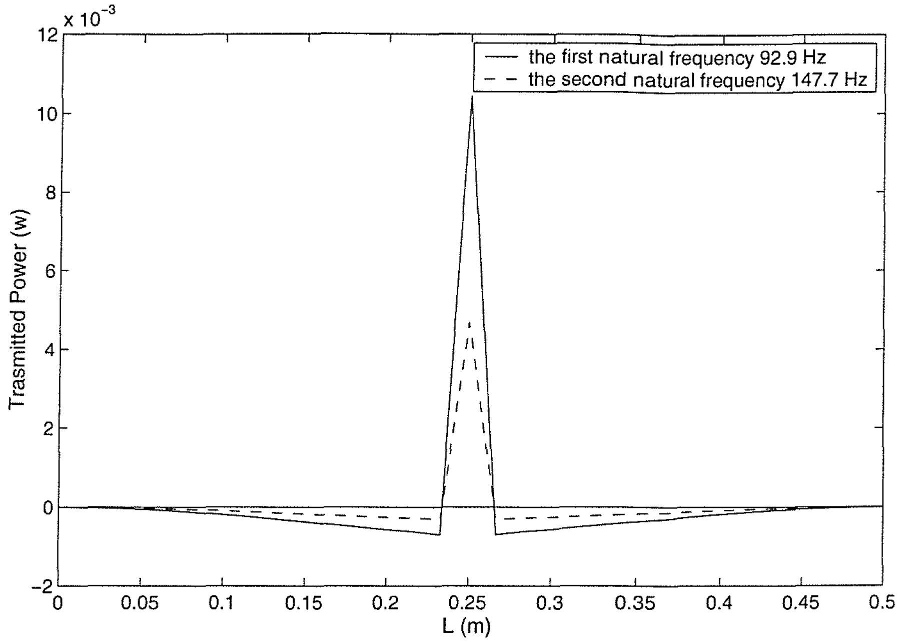

Figure 6.14. Time averaged transmitted power from plate to beam 1, negative value means the power transmitted from beam 1 to the plate.

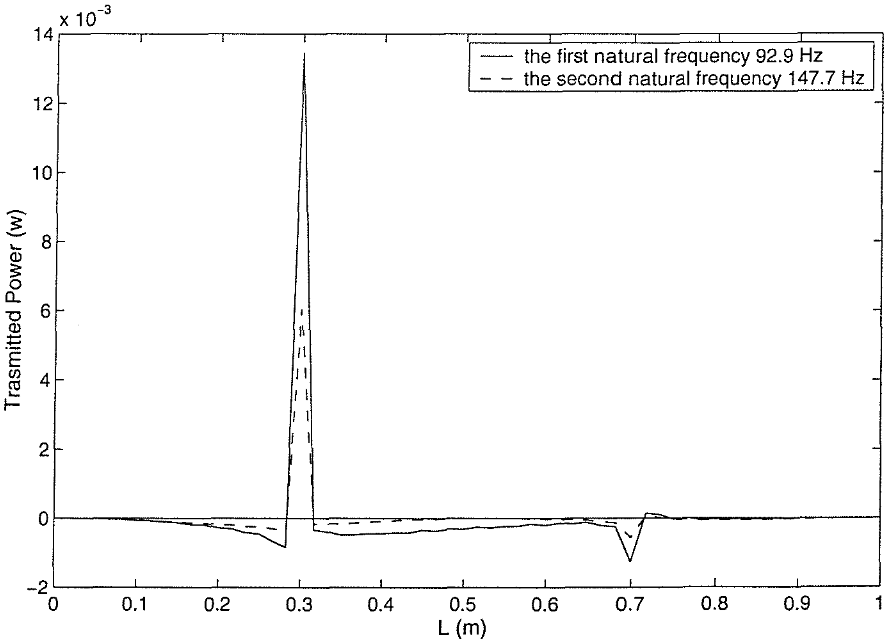

Figure 6.15. Time averaged transmitted power from plate to beam 3, negative value means the power transmitted from beam 3 to the plate.

7. POWER FLOW ANALYSIS OF A COUPLED PLATE-CYLINDRICAL SHELL SYSTEM

Many engineering structures (e.g. offshore platform, etc) are constructed by a combination of plates and cylindrical shells. They are joined together by welds, bolts or dashpots. The coupling between these components may be conservative or compliant and dissipative. This chapter continues investigation of the power flow characteristics in a more complex coupled plate-cylindrical shell system excited by an external force as shown in figure 7.1. Substructure techniques are again adopted in both conservative or compliant and dissipative coupling conditions. In a study of the dynamic characteristics of cylindrical shells, Franken (1960) derived the input impedance of a simply supported cylindrical shell but the analysis did not include the influence of bending stiffness of the shell and it has therefore limitations in the estimation of input power in practical applications. Heckl (1962) and Fuller (1983) derived analytical expressions to evaluate the input radial mobility of an infinite elastic cylindrical shell. Harari (1977) developed a general formula to evaluate the transmitted mobility based on the structural impedance of finite and semi-infinite cylindrical shells. Ming, Pan & Norton (1999) present the mobility function and power flow of a semi-infinite cylindrical shell and two coupled shells using Flugge (1973) and Leissa (1973) shell theories. In this chapter, an analysis based on thin cylindrical shell equations as given by Timosheko & Woinowsky-Krieger (1959), Leissa (1973) is presented to calculate the receptance function of simply supported cylindrical shells subject to different types of excitation. The power flow characteristics in the system and across the coupling junction of the cylindrical shell and plate are calculated.

7.1. Substructure Analysis of a Plate-Cylindrical Shell System

The plate-cylindrical shell system under investigation is illustrated in figure 7.1. It is assumed that simply supported boundary conditions apply to the ends of the plate and cylindrical shell. This total system can be separated into two subsystems. That is, a rectangular plate (see, figure 7.2) with simply supported boundary conditions applied to two opposite edges with the coupling edges ($y = \pm b/2$) assumed free and a cylindrical shell (see, figure 7.3) with simply supported boundary conditions applied to the two ends of the shell with the two coupling edges ($\theta = \theta_{b1}, \theta = \theta_{b2}$) assumed free.

7.1.1. The Conservative Coupling of Subsystems

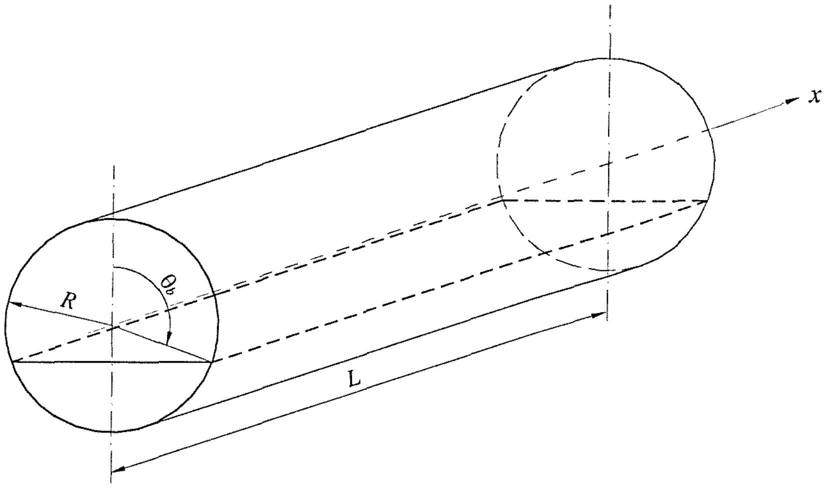

Figure 7.1. Schematic illustration of a plate-cylindrical shell system.

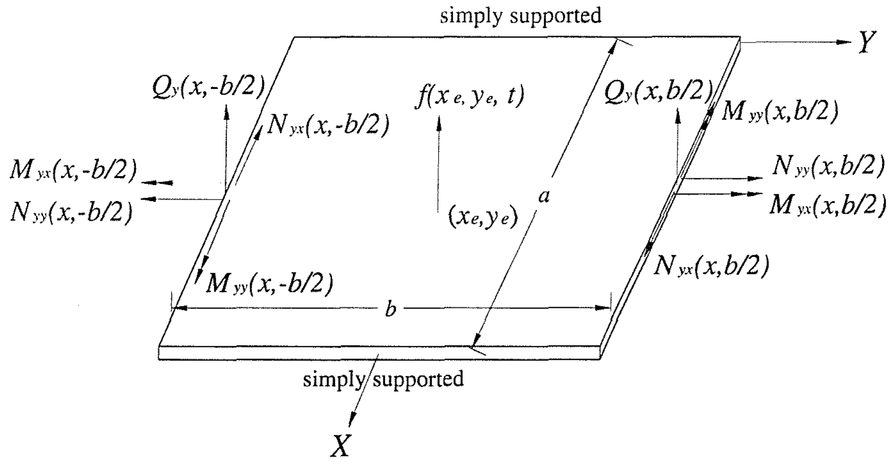

Figure 7.2. Schematic illustration of a plate in local co-ordinate system.

Two types of forces act on each substructure. One is the external excitation force whereas the other is the internal distributed coupling force acting at the coupling edge. The whole system is coupled by the distributed internal forces

$\{\tilde{f}_{cp}\}=[\tilde{N}_{yy},\tilde{Q}_{y},\tilde{M}_{yy}]^T$ (see, for example, figure 7.2) along the coupling edges of the plate and $\{\tilde{f}_{cs}\}=[\tilde{N}_{\theta},\tilde{Q}_{\theta},\tilde{M}_{\theta}]^T$ along the coupling edges of the shell.

When the coupling edges of the plate and cylindrical shell are rigidly connected, the coupling relation between the two substructures determined by their force balance and geometric compatibility conditions at the coupling edges in the global co-ordinate system can be expressed as follows

$$\begin{Bmatrix} T_p\tilde{f}_{cp}^{(1)} \\ T_p\tilde{f}_{cp}^{(2)} \end{Bmatrix} + \begin{Bmatrix} T_{s1}\tilde{f}_{cs}^{(1)} \\ T_{s2}\tilde{f}_{cs}^{(2)} \end{Bmatrix} = 0, \tag{7.1}$$

$$\begin{Bmatrix} T_p\tilde{u}_{cp}^{(1)} \\ T_p\tilde{u}_{cp}^{(2)} \end{Bmatrix} = \begin{Bmatrix} T_{s1}\tilde{u}_{cs}^{(1)} \\ T_{s2}\tilde{u}_{cs}^{(2)} \end{Bmatrix}. \tag{7.2}$$

Here T_p denotes the transmission matrix between the plate local and global co-ordinate systems, T_{s1}, T_{s2} the transmission matrices between the local cylindrical co-ordinate systems of two coupling edges and the global co-ordinate system, respectively; $\tilde{u}_{cp}^{(1)},\tilde{u}_{cp}^{(2)}$ ($\tilde{u}_{cp}=\left[\tilde{u}_y,\tilde{u}_z,\tilde{\theta}_x\right]^T$) the displacement vectors at the two coupling edges of the plate and $\tilde{u}_{cs}^{(1)},\tilde{u}_{cs}^{(2)}$ ($\tilde{u}_{cs}=\left[\tilde{u}_\theta,\tilde{u}_z,\tilde{\theta}_x\right]^T$) the displacement vectors at the two coupling edges of the cylindrical shell respectively.

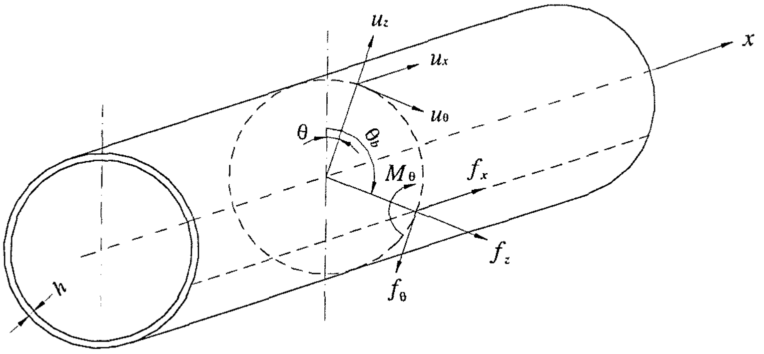

Figure 7.3. Schematic illustration of a cylindrical shell in local co-ordinate system.

The displacement vectors at the coupling edges can be further expressed in terms of components excited by an external excitation vector $\left\{\tilde{f}_e\right\}$ and an internal coupling force vector $\left\{\tilde{f}_c\right\}$ using the theorem due to Rayleigh (1896). That is,

$$\begin{Bmatrix} \tilde{u}_{cp}^{(1)} \\ \tilde{u}_{cp}^{(2)} \end{Bmatrix} = \begin{bmatrix} R_p^{11} & R_p^{12} \\ R_p^{21} & R_p^{22} \end{bmatrix} \begin{Bmatrix} \tilde{f}_{cp}^{(1)} \\ \tilde{f}_{cp}^{(2)} \end{Bmatrix} + \begin{Bmatrix} R_{ep}^1 \tilde{f}_{ep} \\ R_{ep}^2 \tilde{f}_{ep} \end{Bmatrix}, \tag{7.3}$$

$$\begin{Bmatrix} \tilde{u}_{cs}^{(1)} \\ \tilde{u}_{cs}^{(2)} \end{Bmatrix} = \begin{bmatrix} R_s^{11} & R_s^{12} \\ R_s^{21} & R_s^{22} \end{bmatrix} \begin{Bmatrix} \tilde{f}_{cs}^{(1)} \\ \tilde{f}_{cs}^{(2)} \end{Bmatrix} + \begin{Bmatrix} R_{es}^1 \tilde{f}_{es} \\ R_{es}^2 \tilde{f}_{es} \end{Bmatrix}. \tag{7.4}$$

In an alternative formulation, equation (7.1) can be rewritten as

$$\begin{Bmatrix} \tilde{f}_s^{(1)} \\ \tilde{f}_s^{(2)} \end{Bmatrix} = -\begin{Bmatrix} T_{s1}{}^{-1} T_p \tilde{f}_p^{(1)} \\ T_{s2}{}^{-1} T_p \tilde{f}_p^{(2)} \end{Bmatrix}. \tag{7.5}$$

The substitution of equations (7.3)-(7.5) into equation (7.2) allows the coupling relations to be expressed in the form

$$\left(\left[R_{pG}\right]+\left[R_{sG}\right]\right)\begin{Bmatrix} T_p \tilde{f}_p^{(1)} \\ T_p \tilde{f}_p^{(2)} \end{Bmatrix} = \begin{Bmatrix} T_{s1} R_{se}^1 \tilde{f}_{se} \\ T_{s2} R_{se}^2 \tilde{f}_{se} \end{Bmatrix} - \begin{Bmatrix} T_p R_{pe}^1 \tilde{f}_{pe} \\ T_p R_{pe}^2 \tilde{f}_{pe} \end{Bmatrix} \tag{7.6}$$

where

$$\left[R_{pG}\right] = \begin{bmatrix} T_p R_p^{11} T_p{}^{-1} & T_p R_p^{12} T_p{}^{-1} \\ T_p R_p^{21} T_p{}^{-1} & T_p R_p^{22} T_p{}^{-1} \end{bmatrix}, \tag{7.7}$$

$$\left[R_{sG}\right] = \begin{bmatrix} T_{s1} R_s^{11} T_{s1}{}^{-1} & T_{s1} R_s^{12} T_{s2}{}^{-1} \\ T_{s2} R_s^{21} T_{s1}{}^{-1} & T_{s2} R_s^{22} T_{s2}{}^{-1} \end{bmatrix}. \tag{7.8}$$

It therefore follows that the response of the whole system can be determined after solutions of the receptance functions of a single rectangular plate and a cylindrical shell.

7.1.2. Compliant and Dissipative Coupling

If two substructures are connected by spring dampers, the coupling is compliant and dissipative. These spring dampers can be generally treated as independent substructures similar to the plate or the shell. If the dampers are supposed massless, to simplify analysis, let us assume that the spring dampers in each displacement and rotational direction along the coupling edges are independent and have different constant complex stiffnesses at any position. This allows the complex stiffness matrix at any position x along the coupling edge to be written as

$$\left[K_D(x)\right]=\begin{Bmatrix} K_Y(x)(1+\mathrm{i}\eta_y) \\ K_Z(x)(1+\mathrm{i}\eta_z) \\ K_\theta(x)(1+\mathrm{i}\eta_\theta) \end{Bmatrix}. \tag{7.9}$$

The force balance conditions and responses of the substructures expressed in equations (7.1), (7.3) and (7.4) remain unchanged. The geometrical compatibility equations at two coupling edges in the global co-ordinate system can be rewritten as:

$$\begin{Bmatrix} T_p\tilde{f}_{cp}^{(1)} \\ T_p\tilde{f}_{cp}^{(2)} \end{Bmatrix}=\begin{Bmatrix} \left[K_D^{(1)}\right]\left(T_{s1}\tilde{u}_{cs}^{(1)}-T_p\tilde{u}_{cp}^{(1)}\right) \\ \left[K_D^{(2)}\right]\left(T_{s2}\tilde{u}_{cs}^{(2)}-T_p\tilde{u}_{cp}^{(2)}\right) \end{Bmatrix}=-\begin{Bmatrix} T_{s1}\tilde{f}_{cs}^{(1)} \\ T_{s2}\tilde{f}_{cs}^{(2)} \end{Bmatrix}. \tag{7.10}$$

Substituting equations (7.3), (7.4) into equation (7.10), we find the coupling relations become

$$\begin{aligned}\begin{Bmatrix} T_p\tilde{f}_{cp}^{(1)} \\ T_p\tilde{f}_{cp}^{(2)} \end{Bmatrix}&=\left\{\begin{matrix} \left[K_D^{(1)}\right](-T_{s1}R_s^{11}T_{s1}{}^{-1}T_p\tilde{f}_{cp}^{(1)}-T_{s1}R_s^{12}T_{s2}{}^{-1}T_p\tilde{f}_{cp}^{(2)}+T_{s1}R_{es}^{1}\tilde{f}_{es} \\ \left[K_D^{(2)}\right](-T_{s2}R_s^{21}T_{s1}{}^{-1}T_p\tilde{f}_{cp}^{(2)}-T_{s2}R_s^{22}T_{s2}{}^{-1}T_p\tilde{f}_{cp}^{(2)}+T_{s2}R_{es}^{2}\tilde{f}_{es} \end{matrix}\right. \\ &\qquad\left.\begin{matrix} -T_pR_p^{11}T_p{}^{-1}T_p\tilde{f}_{cp}^{(1)}-T_pR_p^{12}T_p{}^{-1}T_p\tilde{f}_{cp}^{(2)}-T_pR_{ep}^{1}\tilde{f}_{ep}) \\ -T_pR_p^{21}T_p{}^{-1}T_p\tilde{f}_{cp}^{(1)}-T_pR_p^{22}T_p{}^{-1}T_p\tilde{f}_{cp}^{(2)}-T_pR_{ep}^{2}\tilde{f}_{ep}) \end{matrix}\right\} \\ &=-\left[K_{DG}\right]\left(\left(\left[R_{sG}\right]+\left[R_{pG}\right]\right)\begin{Bmatrix} T_p\tilde{f}_{cp}^{(1)} \\ T_p\tilde{f}_{cp}^{(2)} \end{Bmatrix}+\begin{Bmatrix} T_{s1}R_{es}^{1}\tilde{f}_{es} \\ T_{s2}R_{es}^{2}\tilde{f}_{es} \end{Bmatrix}-\begin{Bmatrix} T_pR_{ep}^{1}\tilde{f}_{ep} \\ T_pR_{ep}^{2}\tilde{f}_{ep} \end{Bmatrix}\right)\end{aligned} \tag{7.11}$$

where

$$\left[K_{DG}\right]=\begin{bmatrix} K_D^{(1)} & 0 \\ 0 & K_D^{(2)} \end{bmatrix}. \tag{7.12}$$

Therefore, the coupling forces in the global co-ordinate system may be expressed as

$$\begin{Bmatrix} T_p\tilde{f}_{cp}^{(1)} \\ T_p\tilde{f}_{cp}^{(2)} \end{Bmatrix}=\left(\left[I\right]+\left[K_{DG}\right]\left[R_{pG}\right]+\left[K_{DG}\right]\left[R_{sG}\right]\right)^{-1}\left[K_{DG}\right]\left(\begin{Bmatrix} T_{s1}R_{es}^{1}\tilde{f}_{es} \\ T_{s2}f_{es}^{2}\tilde{f}_{es} \end{Bmatrix}-\begin{Bmatrix} T_pR_{ep}^{1}\tilde{f}_{ep} \\ T_pf_{ep}^{2}\tilde{f}_{ep} \end{Bmatrix}\right). \tag{7.13}$$

It therefore follows that the response of the dissipative coupling system can be determined after solutions of the receptance functions of all substructures.

7.1.3. Vibration of a Thin Cylindrical Shell

The whole system under investigation consists of two substructures. That is, a rectangular plate (see, figure 7.2) with simply supported boundary conditions applied to two opposite edges with the coupling edges ($y = \pm b/2$) assumed free and a cylindrical shell (see, figure 7.3) with simply supported boundary conditions applied to the two ends of the shell with the two coupling edges ($\theta = \theta_{b1}, \theta = \theta_{b2}$) assumed free. The bending and in-plane vibration of a thin rectangular plate have been described in chapter 5. Here, the vibration of a thin cylindrical shell is discussed. The basic assumptions of thin shell theory (see, for example, Leissa 1973) are:

1. The thickness of the shell is small compared with other dimensions.
2. Deflections are sufficiently small so that quantities of second and higher order magnitude in the strain-displacement relations may be neglected in comparison with the first order terms.
3. The transverse normal stress is small compared with the other normal stress components and may be neglected.
4. Any straight normal to the middle surface before deformation remains a straight line and normal during deformation and suffers no extension.

Under these assumptions of thin shell theory, the differential equations describing the dynamic behaviour of the cylindrical shell shown in figure 7.3 are expressed as

$$\begin{aligned}&\frac{\partial^2 \tilde{u}_x}{\partial x^2} + \frac{1-\mu}{2R^2}(1+\beta^2)\frac{\partial^2 \tilde{u}_x}{\partial \theta^2} + \frac{1+\mu}{2R}\frac{\partial^2 \tilde{u}_\theta}{\partial x \partial \theta} + \frac{\mu}{R}\frac{\partial \tilde{u}_z}{\partial x} - R\beta^2 \frac{\partial^3 \tilde{u}_z}{\partial x^3} \\ &+\beta^2 \frac{1-\mu}{2R}\frac{\partial^3 \tilde{u}_z}{\partial x \partial \theta^2} - \frac{\ddot{\tilde{u}}_x}{c_p^2} = -\tilde{f}_x \frac{1-\mu^2}{Eh_s},\end{aligned} \tag{7.14}$$

$$\begin{aligned}&\frac{1+\mu}{2R}\frac{\partial^2 \tilde{u}_x}{\partial x \partial \theta} + \frac{1-\mu}{2}(1+3\beta^2)\frac{\partial^2 \tilde{u}_\theta}{\partial x^2} + \frac{\partial^2 \tilde{u}_\theta}{\partial \theta^2} + \frac{1}{R^2}\frac{\partial \tilde{u}_z}{\partial \theta} - \frac{3-\mu}{2}\beta^2 \frac{\partial^3 \tilde{u}_z}{\partial x^2 \partial \theta} \\ &-\frac{\ddot{\tilde{u}}_\theta}{c_p^2} = -\tilde{f}_\theta \frac{1-\mu^2}{Eh_s},\end{aligned} \tag{7.15}$$

$$\frac{\mu}{R}\frac{\partial \tilde{u}_x}{\partial x} - R\beta^2 \frac{\partial^3 \tilde{u}_x}{\partial x^3} + \beta^2 \frac{1-\mu}{2R}\frac{\partial^3 \tilde{u}_x}{\partial x \partial \theta^2} + \frac{1}{R^2}\frac{\partial \tilde{u}_\theta}{\partial \theta} - \frac{3-\mu}{2}\beta^2 \frac{\partial^3 \tilde{u}_\theta}{\partial x^2 \partial \theta} + (1+\beta)\frac{\tilde{u}_z}{R^2}$$
$$+\beta^2\left(R^2 \frac{\partial^4 \tilde{u}_z}{\partial x^4} + 2\frac{\partial^4 \tilde{u}_z}{\partial x^2 \partial \theta^2} + \frac{1}{R^2}\frac{\partial^4 \tilde{u}_z}{\partial \theta^4}\right) + 2\beta^2 \frac{\partial^2 \tilde{u}_z}{R^2 \partial \theta^2} + \frac{\ddot{\tilde{u}}_z}{c_p^2} = \tilde{f}_z \frac{1-\mu^2}{Eh_s}, \tag{7.16}$$

with stress-displacement relations

$$\tilde{N}_x = \frac{Eh_s}{1-\mu^2}\left[\frac{\partial \tilde{u}_x}{\partial x} + \mu\left(\frac{1}{R}\frac{\partial \tilde{u}_\theta}{\partial \theta} + \frac{\tilde{u}_z}{R}\right)\right] - \frac{D}{R}\frac{\partial^2 \tilde{u}_z}{\partial x^2}, \tag{7.17}$$

$$\tilde{N}_\theta = \frac{Eh_s}{1-\mu^2}\left[\frac{1}{R}\frac{\partial \tilde{u}_\theta}{\partial \theta} + \frac{\tilde{u}_z}{R} + \mu\frac{\partial \tilde{u}_x}{\partial x}\right] + \frac{D}{R^3}\left(\frac{\partial^2 \tilde{u}_z}{\partial \theta^2} + \tilde{u}_z\right), \tag{7.18}$$

$$\tilde{N}_{x\theta} = \frac{Eh_s}{2(1+\mu)}\left[\frac{1}{R}\frac{\partial \tilde{u}_x}{\partial \theta} + \frac{\partial \tilde{u}_\theta}{\partial x} - \frac{h_s^2}{12R^2}\frac{\partial^2 \tilde{u}_z}{\partial x \partial \theta}\right], \tag{7.19}$$

$$\tilde{N}_{\theta x} = \frac{Eh_s}{2(1+\mu)}\left[\frac{1}{R}\frac{\partial \tilde{u}_x}{\partial \theta} + \frac{\partial \tilde{u}_\theta}{\partial x} + \frac{h_s^2}{12R^2}\frac{\partial^2 \tilde{u}_z}{\partial x \partial \theta}\right], \tag{7.20}$$

$$\tilde{M}_x == -D\left[\frac{\partial^2 \tilde{u}_z}{\partial x^2} + \frac{\mu}{R^2}\left(\frac{\partial^2 \tilde{u}_z}{\partial \theta^2} - \frac{\partial \tilde{u}_\theta}{\partial \theta}\right) - \frac{1}{R}\frac{\partial \tilde{u}_x}{\partial x}\right], \tag{7.21}$$

$$\tilde{M}_\theta = -D\left[\mu\frac{\partial^2 \tilde{u}_z}{\partial x^2} + \frac{1}{R^2}\left(\frac{\partial^2 \tilde{u}_z}{\partial \theta^2} + \tilde{u}_z\right)\right], \tag{7.22}$$

$$\tilde{M}_{x\theta} = -\frac{D(1-\mu)}{R}\left[\frac{\partial^2 \tilde{u}_z}{\partial x \partial \theta} - \frac{\partial \tilde{u}_\theta}{\partial x}\right], \tag{7.23}$$

$$\tilde{M}_{\theta x} = -\frac{D(1-\mu)}{R}\left[\left(\frac{\partial^2 \tilde{u}_z}{\partial x \partial \theta} - \frac{\partial \tilde{u}_\theta}{2\partial x}\right) + \frac{\partial \tilde{u}_x}{2R\partial \theta}\right], \tag{7.24}$$

$$\tilde{Q}_x = \frac{\partial \tilde{M}_x}{\partial x} + \frac{1}{R}\frac{\partial \tilde{M}_{\theta x}}{\partial \theta}, \tag{7.25}$$

$$\tilde{Q}_\theta = \frac{1}{R}\frac{\partial \tilde{M}_\theta}{\partial \theta} + \frac{\partial \tilde{M}_{x\theta}}{\partial x}, \tag{7.26}$$

where $c_p = \sqrt{E/\rho(1-\mu^2)}$ denotes the phase velocity of the compressional wave travelling in an elastic shell, $\beta^2 = h_s^2/12R^2$, $\tilde{f}_x, \tilde{f}_\theta, \tilde{f}_z$ denote the distributed forces along x, θ, z directions respectively and D denotes the flexural rigidity of the shell similar to equation (5.12).

The boundary conditions applied at the ends of the cylindrical shell are assumed simply supported, but the axial displacement is not zero. This is analogous to the axial movement allowed at an end of a simply supported beam (see, for example Warburton 1976). Under the influence of harmonic excitation it is assumed that

$$\tilde{u}_x = \sum_{i=1}^{n}\sum_{j=1}^{m} U_{ij} \cos j\theta \cos k_i x \cdot e^{i\omega t}, \tag{7.27}$$

$$\tilde{u}_\theta = \sum_{i=1}^{n}\sum_{j=1}^{m} V_{ij} \sin j\theta \sin k_i x \cdot e^{i\omega t}, \tag{7.28}$$

$$\tilde{u}_z = \sum_{i=1}^{n}\sum_{j=1}^{m} W_{ij} \cos j\theta \sin k_i x \cdot e^{i\omega t}, \tag{7.29}$$

where $k_i = {}^{i\pi}\!/_{l}$.

The substitution of equations (7.27)-(7.29) into the equations of motion (7.14)-(7.16) yields a homogeneous set of three linear algebraic equations for the displacement amplitudes U_{ij}, V_{ij}, W_{ij} given by

$$\begin{bmatrix} L_{11} & L_{12} & L_{13} \\ L_{21} & L_{22} & L_{23} \\ L_{31} & L_{32} & L_{33} \end{bmatrix} \begin{bmatrix} U_{ij} \\ V_{ij} \\ W_{ij} \end{bmatrix} = \begin{bmatrix} F_x \\ F_\theta \\ F_z \end{bmatrix}. \tag{7.30}$$

Here,

$$L_{11} = R^2 k_i^2 + \tfrac{1-\mu}{2}(1+\beta^2) j^2 - \lambda^2, \tag{7.31}$$

$$L_{12} = L_{21} = -\tfrac{1+\mu}{2} R j k_i, \tag{7.32}$$

$$L_{13} = L_{31} = -\mu R k_i - \frac{1-\mu}{2} R \beta^2 j^2 k_i + \beta^2 (k_i R)^3, \tag{7.33}$$

$$L_{22} = \tfrac{1-\mu}{2} R^2 (1+3\beta^2) k_i^2 + j^2 - \lambda^2, \tag{7.34}$$

$$L_{23} = L_{32} = \frac{3-\mu}{2}\beta^2 j(k_i R)^2 + j, \tag{7.35}$$

$$L_{33} = 1 + \beta^2\left(R^2 k_i^2 + j^2\right)^2 - \beta^2(2j^2 - 1) - \lambda^2, \tag{7.36}$$

where $\lambda = {}^{\omega R}\!/_{c_p}$ is a non-dimensional frequency, and

$$F_x = 2a^2 \frac{1-\mu^2}{Eh_s l\pi}\int_0^l \int_0^{2\pi} \tilde{f}_x \cos j\theta \cos k_i x dx d\theta, \tag{7.37}$$

$$F_\theta = 2a^2 \frac{1-\mu^2}{Eh_s l\pi}\int_0^l \int_0^{2\pi} \tilde{f}_\theta \sin j\theta \sin k_i x dx d\theta, \tag{7.38}$$

$$F_z = 2a^2 \frac{1-\mu^2}{Eh_s l\pi}\int_0^l \int_0^{2\pi} \tilde{f}_z \cos j\theta \sin k_i x dx d\theta. \tag{7.39}$$

If a moment $\tilde{M}_e$ is applied in the θ-direction at position (x_b, θ_b), equations (7.37)-(7.39) become

$$F_x = 0, \tag{7.40}$$

$$F_\theta = 2\frac{1-\mu^2}{Eh_s l\pi}\tilde{M}_e \sin j\theta_b \sin k_i x_b, \tag{7.41}$$

$$\begin{aligned} F_z &= 2a\frac{1-\mu^2}{Eh_s l\pi}\int_0^{2\pi}\int_0^l \frac{\partial}{a\partial\theta}\left[\tilde{M}_e \delta(\theta-\theta_b)\delta(x-x_b)\right]\cos j\theta \sin k_i x dx d\theta \\ &= -2\frac{1-\mu^2}{Eh_s l\pi}\int_0^{2\pi}\int_0^l \frac{\partial}{\partial\theta}\left[\cos j\theta \sin k_i x\right]\tilde{M}_e \delta(\theta-\theta_b)\delta(x-x_b) dx d\theta \\ &= 2j\frac{1-\mu^2}{Eh_s l\pi}\tilde{M}_e \sin j\theta_b \sin k_i x_b. \end{aligned} \tag{7.42}$$

It therefore follows that the response of the cylindrical shell can be determined under any kind of excitation.

7.2. Power Flow in a Thin Cylindrical Shell

Xing and Price (1999) and as discussed in chapter 2 expressed the basic definition of a power flow density vector in a continuum. Similar to the definition of a power flow density vector in a thin plate (see, equations 5.55-5.58), the instantaneous power flow density vector of a thin cylindrical shell in a local co-ordinate system is defined in the form

$$q_x(t) = -\mathrm{Re}\{\dot{\tilde{u}}_x\}\mathrm{Re}\{\tilde{N}_x\} - \mathrm{Re}\{\dot{\tilde{u}}_\theta\}\mathrm{Re}\{\tilde{N}_{x\theta}\} - \mathrm{Re}\{\dot{\tilde{u}}_z\}\mathrm{Re}\{\tilde{Q}_x\} + \mathrm{Re}\left\{\partial\dot{\tilde{u}}_z\big/\partial x\right\}\mathrm{Re}\{\tilde{M}_x\} + \mathrm{Re}\left\{\partial\dot{\tilde{u}}_z\big/R\partial\theta - \dot{\tilde{u}}_\theta\big/R\right\}\mathrm{Re}\{\tilde{M}_{x\theta}\}, \tag{7.43}$$

$$q_\theta(t) = -\mathrm{Re}\{\dot{\tilde{u}}_x\}\mathrm{Re}\{\tilde{N}_{\theta x}\} - \mathrm{Re}\{\dot{\tilde{u}}_\theta\}\mathrm{Re}\{\tilde{N}_\theta\} - \mathrm{Re}\{\dot{\tilde{u}}_z\}\mathrm{Re}\{\tilde{Q}_\theta\} + \mathrm{Re}\left\{\partial\dot{\tilde{u}}_z\big/R\partial\theta - \dot{\tilde{u}}_\theta\big/R\right\}\mathrm{Re}\{\tilde{M}_\theta\} + \mathrm{Re}\left\{\partial\dot{\tilde{u}}_z\big/\partial x\right\}\mathrm{Re}\{\tilde{M}_{\theta x}\}, \tag{7.44}$$

with a time averaged quantity

$$\langle q_x(t)\rangle = -\frac{1}{2}\mathrm{Re}\left\{\tilde{N}_x\dot{\tilde{u}}_x^* + \tilde{N}_{x\theta}\dot{\tilde{u}}_\theta^* + \tilde{Q}_x\dot{\tilde{u}}_z^* - \tilde{M}_x\left(\partial\dot{\tilde{u}}_z\big/\partial x\right)^* - \tilde{M}_{x\theta}\left(\partial\dot{\tilde{u}}_z\big/R\partial\theta - \dot{\tilde{u}}_\theta\big/R\right)^*\right\}, \tag{7.45}$$

$$\langle q_\theta(t)\rangle = -\frac{1}{2}\mathrm{Re}\left\{\tilde{N}_{\theta x}\dot{\tilde{u}}_x^* + \tilde{N}_\theta\dot{\tilde{u}}_\theta^* + \tilde{Q}_\theta\dot{\tilde{u}}_z^* - \tilde{M}_{\theta x}\left(\partial\dot{\tilde{u}}_z\big/\partial x\right)^* - \tilde{M}_\theta\left(\partial\dot{\tilde{u}}_z\big/R\partial\theta - \dot{\tilde{u}}_\theta\big/R\right)^*\right\}. \tag{7.46}$$

The time averaged power flow density vector in equations (7.45), (7.46) is equivalent to the structural intensity parameter described by Hambric (1990), Gavic & Pavic (1993) and has similarity to an acoustic intensity parameter in a fluid domain being the product of pressure and the in-phase component of fluid particle velocity (see, for example, Fahy 1989).

The instantaneous power flow density vector across a coupling edge is only in the y direction of the plate in the local plate co-ordinate system (see, figure 7.2) and can be expressed as

$$q_y^c = -\mathrm{Re}\{\dot{\tilde{u}}_x\}\mathrm{Re}\{\tilde{N}_{xy}\} - \mathrm{Re}\{\dot{\tilde{u}}_y\}\mathrm{Re}\{\tilde{N}_{yy}\} - \mathrm{Re}\{\dot{\tilde{u}}_z\}\mathrm{Re}\{\tilde{Q}_y\} + \mathrm{Re}\{\dot{\tilde{\theta}}_y\}\mathrm{Re}\{\tilde{M}_{xy}\} + \mathrm{Re}\{\dot{\tilde{\theta}}_x\}\mathrm{Re}\{M_{yy}\} \tag{7.47}$$

The total transmitted power at a coupling edge is given by the integral of the transmitted power flow density along the length of the coupling edge. That is,

$$q_{trans} = \int_0^a q_y^c dx, \tag{7.48}$$

with corresponding time averaged quantity

$$\langle q_{trans} \rangle = \int_0^a \langle q_y^c \rangle dx . \tag{7.49}$$

It is convenient to determine the power flow at the coupling edge using a substructure receptance approach because the solution of the coupling force in the coupling relationship equations (7.5), (7.6) or (7.13) and the receptance are simple and in the same local co-ordinate axis system.

7.3. Application to a Proposed System

For illustrative purposes, let us assume that the plate-cylindrical shell system shown in figure 7.1 is defined by the data set:

$\rho = 7750\, kg/m^3$, $E = 206\, GPa$, $\eta = 0.01$, $\mu = 0.3$;

$R = 0.177\, m$, $a = l = 1.284\, m$, $h_p = 0.003 m$, $h_s = 0.005 m$;

and the angles of two coupling edges in the cylindrical co-ordinate system are given by $\theta_{b1} = -\theta_{b2} = 60^\circ$.

Two coupling edge conditions were examined. The first assumes the plate and the cylindrical shell are rigidly connected at the two coupling edges. This means the coupling is conservative, all power output from the source substructure inputs to the receiver substructure. The other assumes that they are connected by uniform distributed stiffness dampers at the two coupling edges. Therefore, the coupling is compliant and dissipative and a portion of the power output from the source substructure stores and dissipates in the coupling.

7.3.1. Conservative Coupling Edge

Figures 7.5 and 7.6 illustrate the variation of the time averaged input power of external excitation and transmitted power flows from the plate to the shell with frequency to a unit amplitude loading applied at the centre of the plate. The results derived by a global FEA model describing the cylindrical shell and the plate are included to verify the substructure calculations.

The FEA model has the same structural characteristics as the original plate-cylindrical shell system and contains 1209 nodes (341 nodes to describe the plate and 930 nodes for the shell) and 1200 plate-shell elements. 150 natural frequencies and principal mode shapes of the system were extracted using FEA package ANSYS spanning the frequency range up to 2200 Hz. From the surface deflection data at each node, the spatial averaged surface squared velocity of each element was derived. Since the receiver shell is not connected to any other substructure except the source plate, the transmitted time averaged power determined by the FEA model and illustrated in figure 7.5 equals the rate of energy dissipation of the shell due to the internal loss factor. That is

$$\langle q_{trans} \rangle \approx 2\omega\eta\rho\pi R l h_s \overline{\left|v_s^2(f)\right|} \approx \langle q_{in} \rangle - \omega\eta\rho a b h_p \overline{\left|v_p^2(f)\right|}, \tag{7.50}$$

where $\overline{\left|v_s^2(f)\right|}$, $\overline{\left|v_p^2(f)\right|}$ denote spatial average squared velocities of the shell and plate respectively. The total energy dissipation of the system in a period is equal to the time averaged input power as shown in figure 7.5.

It is seen from figures 7.5 and 7.6 that only small differences exist between the theoretical substructure predictions and those evaluated by the FEA approach, thus providing a measure of confidence in the validity of the computations.

In the following presentation of spatial distributions of time averaged power flow density vectors, figures 7.7 and 7.8 relate to a unit amplitude exciting force applied at position $x_e=0.45m$, $y_e=-0.023m$ defined in the local co-ordinate axes of the plate and this position of excitation is indicated by the symbol "+" in these figures. For clarity of presentation, the modulus of time averaged power flow density vectors of the plate in figures 7.7 and 7.8 have the same definition as given in equation (5.65), whereas those in shell are defined as

$$\left|\langle q(x,\theta)\rangle\right|^{(d)} = \left|\langle q(x,\theta)\rangle\right|^{0.2} = \left(\left|q_x(x,\theta)\right|^2 + \left|q_\theta(x,\theta)\right|^2\right)^{0.1}. \tag{7.51}$$

Figure 7.7 illustrates the distribution of the time averaged power flow density vector at a frequency of 160.5 Hz. This corresponds to the first natural frequency of the system. Figure 7.8 shows the corresponding vector distribution at a frequency of 177 Hz. This coincides with the second natural frequency of the system.

The power flow density vector displaying the dynamic behaviour of a plate-cylindrical shell under a single force excitation is very complex and frequency dependent in character. The power flow characteristics in this system are similar to those observed in the L-shaped plate. For example, power flows from the excitation source and usually ends at a boundary but there exists the possibility that the time averaged power flow density is equal to zero at positions in the plate and a circulation or vortex type flow exists in the vicinity of this position. Such flows are illustrated in figures 7.7 and 7.8.

The highest eigenfrequency admitted in the present calculation for a suitable accuracy of convergence of solution in the analysis is at least 300 kHz.

7.3.2. Compliant and Dissipative Coupling Edge

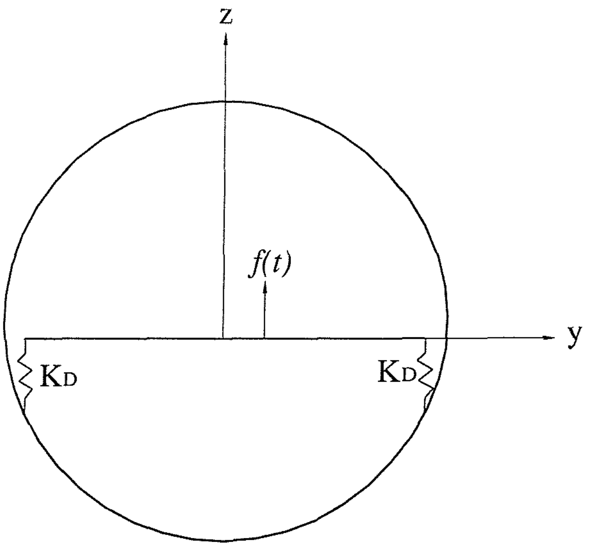

Figure 7.4. Schematic illustration of a section of a plate-cylindrical shell system with a compliant and dissipative coupling.

Figure 7.4 schematically illustrates a section of a plate-cylindrical shell system with a compliant and disspative coupling. The material and geometric properties of the plate and shell are the same as the original model but a uniform distributed damper connects both together. The complex stiffness per unit length of damper is only in the z direction and is defined by

$$K_D = 10^4(1 + i\eta_z)N / m^2 . \tag{7.52}$$

Figures 7.9-7.11 illustrate the variation of the time averaged power flows with frequency to different assumed coupling damping coefficient η_z. A unit force excitation is applied at the centre of the plate. Figure 7.9 shows the results of time averaged input power caused by the external excitation whereas figures 7.10 and 7.11 display the results of time averaged output power from the plate and input power to the shell, respectively.

These figures illustrate that for different coupling damping models, the principal dynamic characteristics of the system remain nearly the same as measured by the natural frequencies of the system, the input power caused by the external excitation and the power from the damping coupling into the receiver shell. But the differences seen in the time averaged power from the plate to the damping coupling are large. This implies that the coupling damping only absorbs and dissipates the energy stored originally in the source plate and there is no obvious influence of coupling damping to the dynamic behaviour of the receiver shell. The greater the coupling damping value, the larger the energy dissipation at the coupling edges.

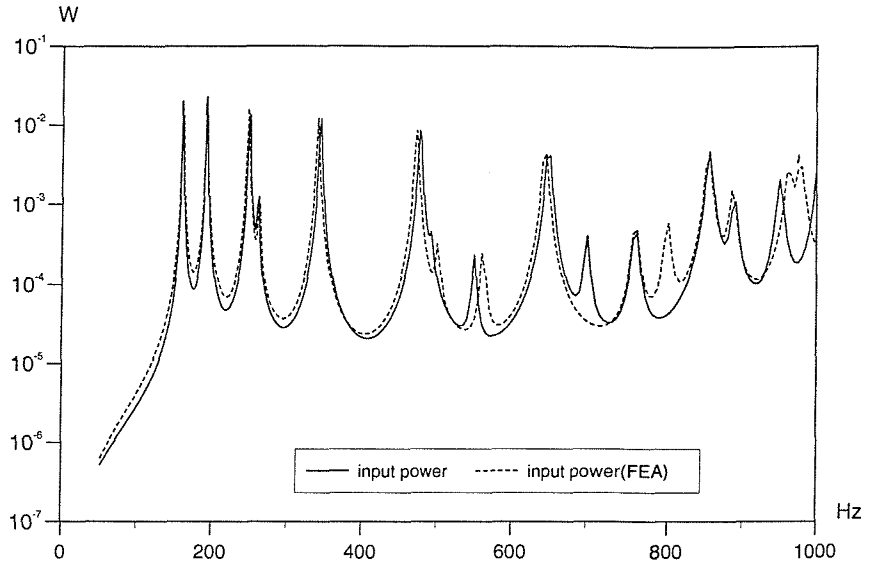

Figure 7.5. Results of time averaged external input power (excitation at the centre of the plate).

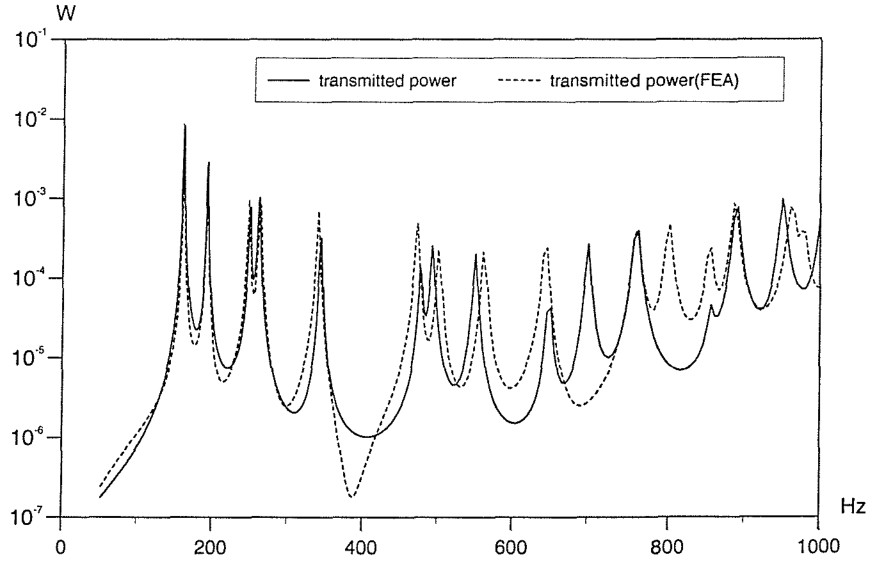

Figure 7.6.Results of time averaged transmitted power from the plate to the shell (excitation at the centre of the plate).

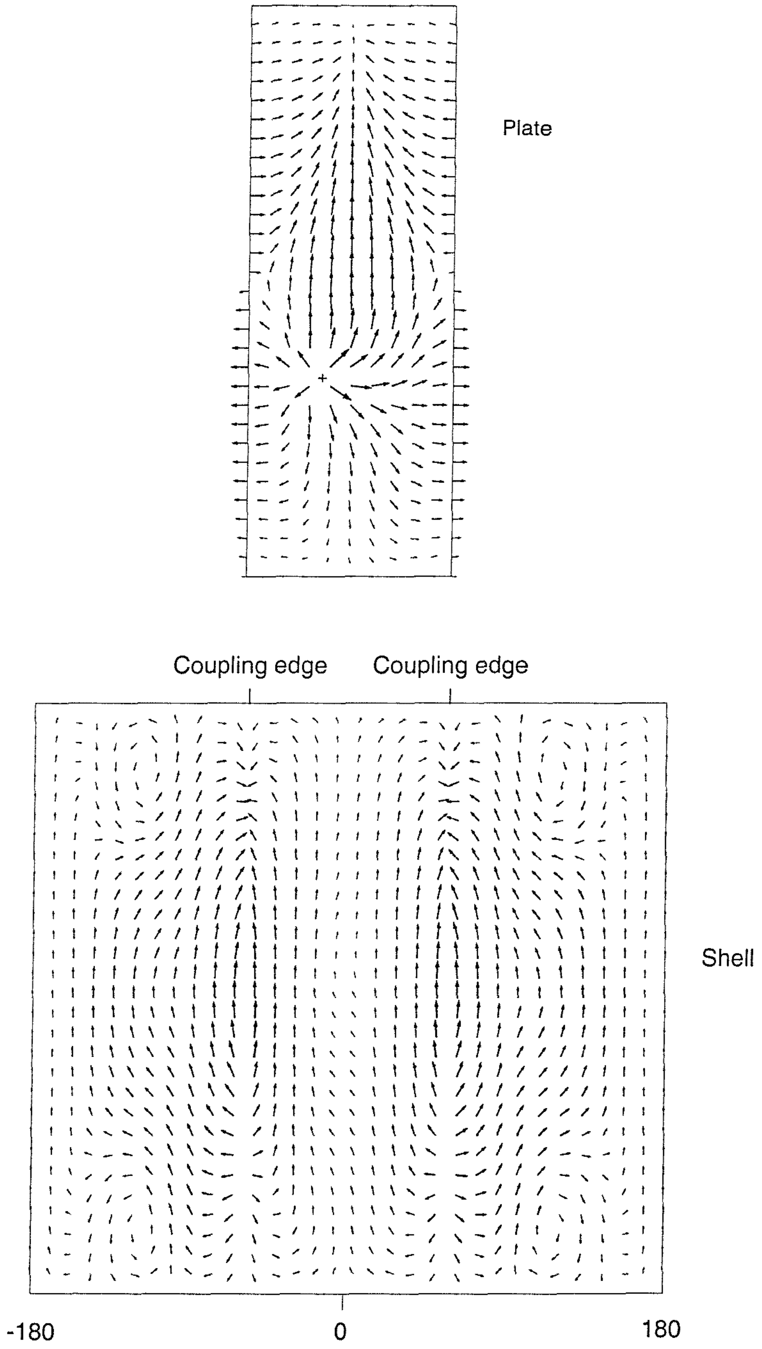

Figure 7.7. Time averaged power flow density vector in the system, f=160.5 Hz. "+" indicates the excitation position.

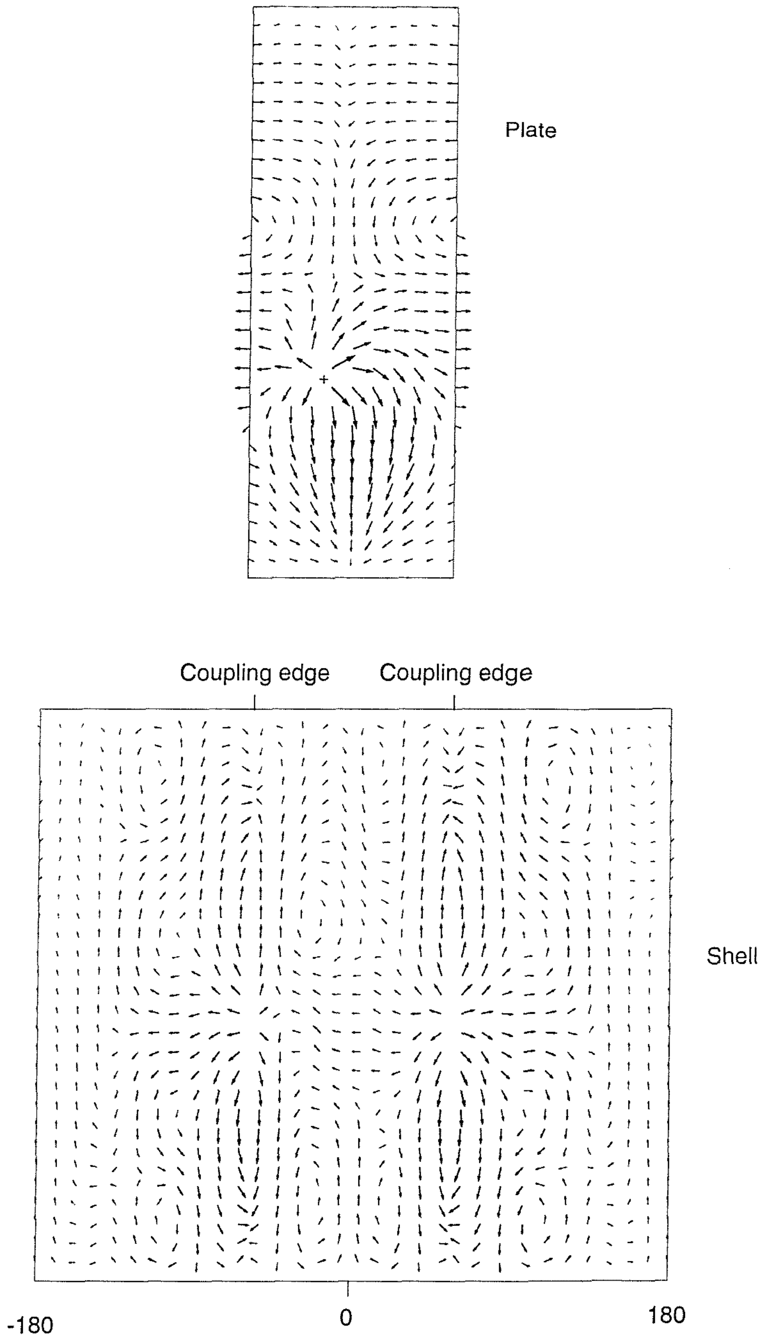

Figure 7.8. Time averaged power flow density vector in the system, *f*=177.0 Hz. "+" indicates the excitation position.

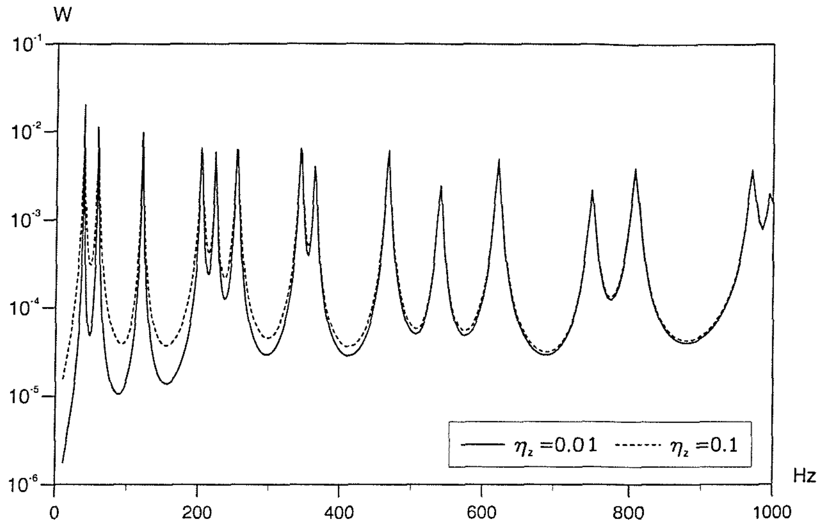

Figure 7.9. Results of time averaged external input power for the compliant and dissipative coupling.

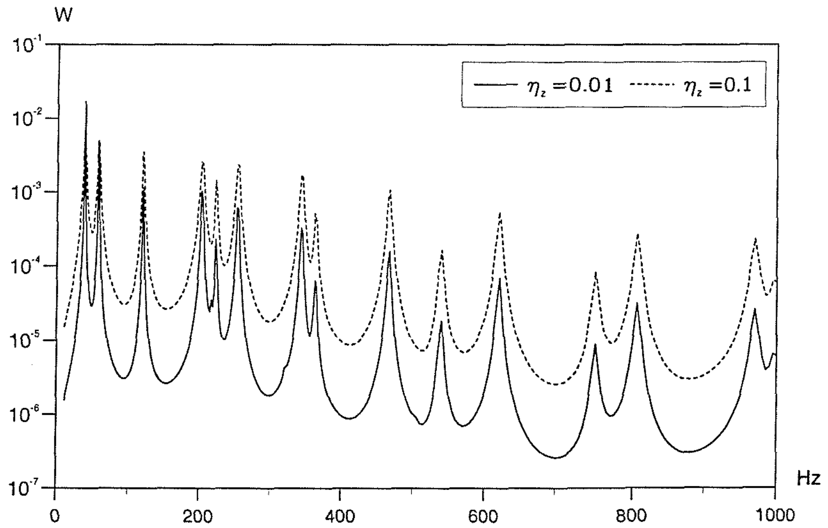

Figure 7.10. Results of time averaged transmitted power from the plate to the damper for the compliant and dissipative coupling.

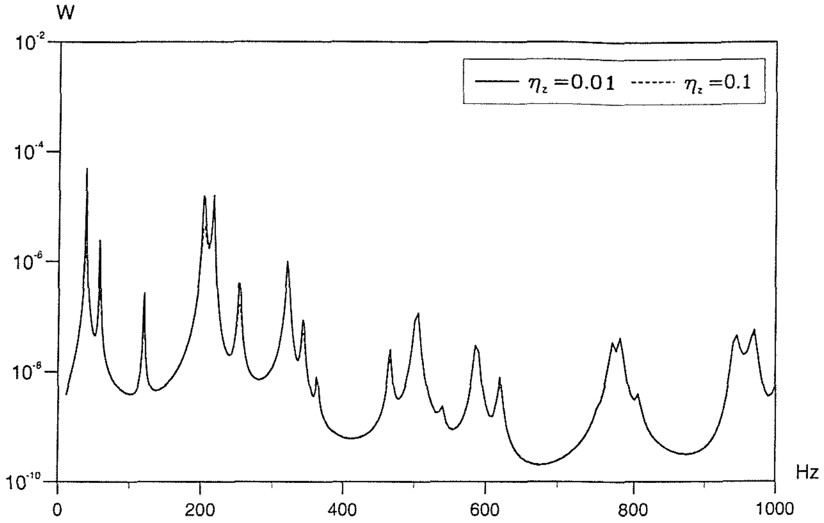

Figure 7.11. Results of time averaged transmitted power from the damper to the shell for the compliant and dissipative coupling.

8. CONCLUSIONS

8.1. Conclusions

This thesis develops and discusses a general substructure approach to investigate power flow characteristics of engineering structures. Each substructure is modelled analytically or numerically and its receptance function is formulated by modal analysis. The method may be classified as a form of sub-structuring using free-free interface conditions. The displacement contribution of the external excitation and internal interface coupling forces are deduced, permitting the power flow between the interface of substructures to be determined. A power flow density vector is defined and the corresponding power flow lines illustrate the flow of power in plates and shells. Engineering application examples of beam frames, a L-shaped plate system, a corner plate system, a beam-stiffened plate system and a coupled plate-cylindrical shell system demonstrate the applicability of the method and detailed configurations display the power flow characteristics associated with these systems. Some conclusions are obtained as follows.

Power flow characteristics in systems strongly relate to their dynamic responses and may be larger in magnitude than the input power of the excitation at any instant because of the influence of resonance. When only one excitation source exists, it was shown that the time averaged input power of excitation is always greater in value than the other time averaged quantities. But when several excitation sources are applied at the same time, the time averaged input power of an exciting source may be negative behaving as an active control source at some exciting frequencies. The input power depends on the excitation, geometrical and dynamical characteristics of the subsystems.

The resonance influences of beam frames in both instantaneous power and time-averaged quantity decrease as the frequency increases, with stable dynamic characteristics exhibited at higher frequencies (higher modal density).

On a coupling edge of the coupled plate system (chapter 5), energy does not always flow from source plate to receiver plate at some sections of the coupling edge. In fact, it was shown that energy flows from receiver to source plate. The direction of time averaged power flow is dependent on the phase angle between internal force and velocity response. At positions on the coupling edge where the phase angle between internal bending moment and angular velocity is less than 90°, the plate absorbs energy. Otherwise, the plate transmits energy when the phase angle is greater than 90°.

Power flow characteristics in L-shaped plates and in corner plates (chapter 5) differ from those observed in an infinite plate. The time averaged power flow density value at positions near the source is not necessarily larger than its value at positions far from the source. Time averaged power usually flows from the excitation source and ends at a boundary but there is every likelihood that the time averaged power flow density is equal to zero at positions on the plate and a circulation or vortex like power flow structure may exist around this zero density power flow position. The corner of three plates is defined as a boundary point by the basic boundary conditions, so its power density is zero and power flows around the corner of the three plates also creating in a vortex type flow. The instantaneous power flow describes the characteristics of energy exchange between kinetic and potential energy. The peak value position of the modal shape is similar to a power source when the system releases energy and a sink when the system absorbs energy.

When an external force is applied to a plate, the stiffened beam in the beam-stiffened plate system (chapter 6) can absorb energy from the plate at some sections. This absorbed energy can be separated into two parts. One is dissipated by damping of the beam and the other transmits along the beam and releases to other sections of the plate. When an external force is applied to the beam, the stiffened beam always absorbs energy from the excitation source and then releases the energy to other substructures. Therefore the beam becomes the main path of transmission of power flow in the whole system.

Power flow characteristics in coupled plate-cylindrical shell systems (chapter 7) are similar to those in coupled plate systems. For different coupling damping models, the principal dynamic characteristics of the system remain apparently similar to those measured by the natural frequencies of the system, the input power caused by the external excitation and the power from the damping coupling into the receiver shell. The main influence of coupling damping value at a compliant and dissipative coupling edge is observed in the source substructure plate. For example, for the same applied excitation, the greater the coupling damping value, the greater the energy dissipated at the coupling edge thus reducing the energy dissipated in the source plate.

8.2. Further Research Work

To develop a practised useable knowledge base requires further applications of power flow analysis to engineering structures. This would form the basis of development of a power flow calculating program package for general engineering structures. Another area of further research is to improve the SEA results in the middle frequency range. For example, to predict indirect power transfer coefficients and their experimental verification as well as to predict and measure power transfer coefficients under conditions of lower frequency modal overlap.

Another future research study is power flow analysis in the time domain. Transient excitations incorporated into power flow analysis of engineering structures is also an area of interest but currently unavailable. When examining the dynamic behaviour of complex structures involving many different substructures built from different materials (steel, composites), in which some material properties of substructures are non-linear, analysis in frequency domain is not valid and a time domain analysis is necessary.

REFERENCES

1. L. S. BEALE and M. L. ACCORSI 1995 *Journal of Sound and Vibration* **185**(4), 685-702. Power flow in two and three dimensional frame structures.
2. A. N. BERCIN and R. S. LANGEY 1996 *Computers and Structures* **59**, 869-875. Application of the dynamic stiffness technique to the in-plane vibrations of plate structures.
3. M. BESHARA and A. J. KEANE 1997 *Journal of Sound and Vibration* **203**(2), 321-339. Vibrational energy flows in beam networks with compliant and dissipative joints.
4. M. BESHARA and A. J. KEANE 1998 *Journal of Sound and Vibration* **213**(3), 511-535. Vibrational energy flows between plates with compliant and dissipative couplings.
5. R. E. D. BISHOP, G. M. L. GLADWELL and S. MICHAELSON 1965 *The matrix analysis of vibration.* Cambridge University Press.
6. R. E. D. BISHOP and D. C. JOHNSON 1979 *The mechanics of vibration.* Cambridge University Press.
7. Y. I. BOBROVNITSKII 1999 *Some energy relations for mechanical systems.* IUTAM Symposium on SEA. (F. J. FAHY and W. G. PRICE Eds.), 37-46, Kluwer Academic Publishers.
8. C. CABOS 1999 *Short communication on SEA applied to ship structures.* IUTAM Symposium on SEA. (F. J. FAHY and W. G. PRICE Eds.), 351-352, Kluwer Academic Publishers.
9. R. R. Jr. CRAIG and M. C. C. BAMPTON 1968 *AIAA Journal* **6**, 1313-1319. Coupling of substructures for dynamic analysis.
10. R. R. Jr. CRAIG and C. J. CHANG 1976 *AIAA Journal* **14**, 1633-1635. Free-interface methods of substructure coupling for dynamic analysis.
11. L. CREMER, M. HECKL and E. E. UNGAR 1988 *Structure-borne sound.* Springer-Verlag, Berlin.

12. J. C. CROMER and M. LALANNE 1976 *Shock and Vibration Bull.* **46**(5), 177-185. Dynamic behaviour of complex structures using part experiment, part theory.

13. J. M. CUSCHIERI 1990(a) *Journal of Sound and Vibration* **143** 65-74. Vibration transmission through periodic structures using a mobility power flow approach.

14. J. M. CUSCHIERI 1990(b) *Journal of the Acoustics Society of America* **87**, 1159-1165. Structural power-flow analysis using a mobility approach of a L-shape plate.

15. E. K. DIMITRIADIS and A. D. PIERCE 1988 *Journal of Sound and Vibration* **123** 497-512. Analytical solution for the power exchange between strongly coupled plates under random excitations: a test of a statistical energy analysis concepts.

16. F. J. FAHY 1989 *Sound intensity.* Elsevier Science Publishers, London.

17. F. J. FAHY 1994 *Philosophical of Transactions of Royal Society, London* A **346**, 431-447. Statistical energy analysis: a critical overview.

18. F. J. FAHY and W. G. PRICE (Eds.) 1999 *IUTAM Symposium on statistical energy Analysis.* Kluwer Academic Publishers.

19. H. FARAG and J. PAN 1998 *Journal of the Acoustics Society of America* **104**(1), 204-216. On the free and forced vibration of single and coupled rectangular plates.

20. W. FLUGGE 1973 *Stresses in shell.* Springer-Verlag, New York.

21. P. A. FRANKEN 1960 *Journal of the Acoustics Society of America* **32**, 473-477. Input impedances of simple cylindrical structures.

22. C. R. FREDÖ 1997 *Journal of Sound and Vibration* **199**, 645-666. SEA-like approach for the derivation of energy flow coefficients with a finite element model.

23. C. R. FULLER 1983 *Journal of Sound and Vibration* **87**(3), 409-427. The input mobility of an infinite circular elastic shell with fluid.

24. Y. C. FUNG 1965 *Foundation of solid mechanics.* Englewood Cliffs, NJ: Prentice.

25. L. GARDONIO, S. J. ELLIOT and R. J. PINNINGTON 1997(a) *Journal of Vibration and Acoustics* **207** 61-93. Active isolation of structural vibration on a multiple-degree-freedom system, Part I: the dynamics of the system.

26. L. GARDONIO, S. J. ELLIOT and R. J. PINNINGTON 1997(b) *Journal of Vibration and Acoustics* **207** 95-121. Active isolation of structural vibration on a multiple-degree-freedom system, Part II: effectiveness of active control strategies.

27. L. GAVRIC and G. PAVIC 1993 *Journal of Vibration and Acoustics* **164** 29-43. A finite element method for computation of structural intensity by the normal mode approach.

28. B. M. GIBBS and C. L. S. GILFORD 1976 *Journal of Sound and Vibration* **49**, 267-286. The use of power flow methods for the assessment of sound transmission in building structure.

29. D. J. GORMAN 1982 *Free vibration analysis of rectangular plates.* Elsevier, New York.

30. H. G. D. GOYDER and R. G. WHITE 1980(a) *Journal of Sound and Vibration* **68**(1), 59-75. Vibrational power flow from machines into build-up structures. I. Introduction and approximate analysis of beam and plate-like foundations.

31. H. G. D. GOYDER and R. G. WHITE 1980(b) *Journal of Sound and Vibration* **68**(1), 77-95. Vibrational power flow from machines into build-up structures. II. Wave propagation and power flow in beam-stiffened plates.

32. H. G. D. GOYDER and R. G. WHITE 1980(c) *Journal of Sound and Vibration* **68**(1), 97-117. Vibrational power flow from machines into build-up structures. III. Power flow through isolation system.

33. R. M. GRICE and R. J. PINNINGTON 2000 *Journal of Sound and Vibration* **232**(2), 449-471. Vibration analysis of a thin-plate box using a finite element which accommodates only in-plane motion.

34. L. HALE and L. MEIROVITCH 1982 *AIAA Journal* **20**, 1128-1136. A procedure for improving discrete substructure representation in dynamic synthesis.

35. S. A. HAMBRIC 1990 *Journal of Vibration and Acoustics* **112** 542-549. Power flow and mechanical intensity calculations in structural finite element analysis.

36. A. HARARI 1977 *Journal of the Acoustics Society of America* **62**, 1196-1205. Wave propagation in cylindrical shells with finite regions of structural discontinuity.

37. M. HECKLE 1962 *Journal of the Acoustics Society of America* **34**, 1553-1557. Vibrations of point-driven cylindrical shell.

38. K. H. HERON 1999 *IUTAM Symposium on statistical energy Analysis* 107-118. Predictive SEA using line wave impedances.

39. J. L. HORNER and R. G. WHITE 1991 *Journal of Sound and Vibration* **147**(1), 87-103. Prediction of vibration power transmission through bends and joints in beam-like structures.

40. S. N. HOU 1969 *Shock and Vibration Bulletin* **40**, 25-30. Review of modal synthesis techniques and a new approach.

41. W. C. HURTY 1965 *AIAA Journal* **3**, 678-685. Dynamic analysis of structural systems using component modes.

42. A. J. KEANE 1988 *Statistical energy analysis of engineering structures*. Ph. D. Thesis, Brunel University.

43. A. J. KEANE and W. G. PRICE (Eds.) 1997 *Statistical energy analysis, an overview, with application in structure dynamics*. Cambridge University Press.

44. M. S. KOMPELLA and B. J. BERNHARD 1993 *Proc. SAE Noise and Vibration Conference*. Warrendale, USA: Society of Automotive Engineers. Measurement of the statistical variation of structural-acoustic characteristics of automotive vehicles.

45. R. S. LANGLEY 1989 *Journal of Sound and Vibration* **135**, 319-331. Application of the dynamic stiffness method to the free and force vibrations of aircraft panels.

46. R. S. LANGLEY 1990 *Journal of Sound and Vibration* **159**, 483-502. A derivation of the loss factors used in statistical energy analysis.

47. R. S. LANGLEY and K. H. HERON 1990 *Journal of Sound and Vibration* **143**, 241-253. Elastic wave transmission through plate/beam junctions.

48. R. S. LANGLEY 1992 *Journal of Sound and Vibration* **159**, 483-502. A wave intensity technique for the analysis of high frequency vibration.

49. A. LEISSA 1973 *Vibration of shells*. NASA SP-288, Washington.

50. A. LEISSA 1993 *Vibration of plates*. Acoustical Society of American, Woodbury, New York.

51. T. Y. LI and P. LAVRICH 1999 *Journal of Sound and Vibration* **224**, 757-774. Prediction of power flows through machine vibration isolators.

52. E. LUZZATO and E. ORTOLA 1988 *Journal of Sound and Vibration* **123**, 189-197. The characteristics of energy flow Paths in the study of dynamic systems using SEA theory.

53. R. H. LYON and G. MAIDANIK 1962 *Journal of the Acoustics Society of America* **34**(5), 623-639. Power flow between linearly coupled oscillators.

54. R. H. LYON, 1975 *Statistical energy analysis of dynamic systems, theory and applications*. Cambridge, Massachusetts. MIT Press.

55. A. R. MACE and P. J. SHORTER 2000 *Journal of Sound and Vibration* **233**(3), 369-389. Energy flow models from finite element analysis.

56. J. E. MANNING 1994 *Philosophical of Transactions of Royal Society, London* A **346**, 477-488. Formulation of SEA parameters using mobility functions.

57. C. S. MANOHAR and A. J. KEANE 1994 *Philosophical of Transactions of Royal Society, London* A **346**. Statistics of energy flows in spring-coupled one-dimensional subsystems.

58. L. MEIROVITCH 1967 *Analytical methods in vibration*. New York: Macmillan.

59. A. W. MILLER and A. VON FLOTOW 1989 *Journal of Sound and Vibration* **128**(1), 145-162. A travelling wave approach to power flow in structure networks.

60. R. S. MING, J. PAN and M. P. NORTON 1999 *Journal of the Acoustics Society of America* **105**, 1702-1713. The mobility functions and their application in calculating power flow in coupled cylindrical shells.

61. B. J. NEFSKE and S. H. SUNG 1987 *Statistical energy analysis, ASME, NCA-3*, 47-54. Power flow element analysis of dynamic system: Basic theory and application to beam.

62. J. PAN and C. H. HANSEN 1991 *Journal of the Acoustics Society of America* **89**, 200-209. Active control of total vibratory power flow in a beam. I: Physical system analysis.

63. J. PAN, J. Q. PAN and C. H. HANSEN 1992 *Journal of the Acoustics Society of America* **92**, 895-907. Total power flow from a vibrating rigid body to a thin panel through multiple elastic mounts.

64. M. PETYT 1990 *Introduction to finite element vibration analysis.* Cambridge University Press.

65. R. J. PINNINGTON and R. G. WHITE 1981 *Journal of Sound and Vibration* **75**, 179-197. Power flow through machine isolator to resonant and non-resonant beam.

66. R. J. PINNINGTON 1987 *Journal of Sound and Vibration* **166**, 515-530. Vibrational power flow transmission to a seating of a vibration isolated motor.

67. R. J. RANDALL 1990 *Fluid-structure interaction of submerged shells.* Ph. D. Thesis, Brunel University.

68. LORD RAYLEIGH 1894 *Theory of sound.* Macmillan, London.

69. H. REISMANN and P. S. PAWLIK 1980 *Elasticity theory and application.* New York: Quantum.

70. K. F. RILEY, M. P. HOBSON and S. J. BENCE 1998 *Mathematical methods for physics and engineering*. Cambridge university press.

71. K. SHANKAR and A. J. KEANE 1995 *Journal of Sound and Vibration* **185**, 867-890. Energy flow prediction in a structure of rigidly joined beams using receptance theory.

72. K. SHANKAR and A. J. KEANE 1997 *Journal of Sound and Vibration* **201**, 491-513. Vibrational energy flow analysis using a substructure approach: the application of receptance theory to FEA and SEA.

73. A. SIMMONS 1991 *Journal of Sound and Vibration* **144**, 215-227. Structure-borne sound transmission through plate junctions and estimates of SEA coupling loss factors using the FE method.

74. A. K. SINGH 1978 *Journal of Power Division P02, Proc. ASCE*, 131-140. Dynamic analysis using modal synthesis.

75. J. A. STEEL and R. J. M. CRAIK 1993 *Journal of Sound and Vibration* **178**, 553-561. Statistical energy analysis of structure-borne sound transmission by finite element methods.

76. G. STIMPSON and N. LALOR 1992 *Internoise* **92**, 557-560. SEA extension of a F. E. model to predict total engine noise.

77. S. P. TIMOSHENKO and S. WOINOWSKY-KRIEGER 1959 *Theory of plates and shells.* 2nd Ed., McGraw-Hill, New York.

78. S. P. TIMOSHENKO, and J. N. GOODIER 1970 *Theory of elasticity.* 3rd Edition, McGraw-hill, New York.

79. S. P. TIMOSHENKO, D. H. YOUNG and W. JR. WEAVER 1974 *Vibration problems in engineering.* 4th Edition, Wiley, New York.

80. Z. H. WANG, J. T. XING and W. G. PRICE 2002(a) *Journal of Sound and Vibration* **249** 3-22. Power flow analysis of rod/beam systems using substructure method.

81. Z. H. WANG, J. T. XING and W. G. PRICE 2002(b) *Journal of Sound and Vibration* **250** 627-648. An investigation of power flow characteristics of L-shaped plates adopting a substructure approach.

82. G . B. WARBURTON 1954 *Proceedings of the Institution of Mechanical Engineer 168, 371-16382.* The vibration of rectangular plates.

83. G. B. WARBURTON 1976 *The dynamic behaviour of structures.* Pergamon Press.

84. J. C. WOHLEVER and R. J. BERNHARD 1988 *Report* 0353-12 *HL* 88-24, Ray W Herrick Laboratories, Purdue University, Indiana, USA. Vibrational power flow of rods and beams. Mechanical energy flow models of rods and beams.

85. J. C. WOHLEVER and R. J. BERNHARD 1992 *Journal of Sound and Vibration* **153**, 1-19. Mechanical energy flow models of rods and beams.

86. J. T. XING 1984 *Some theoretical and computational aspects of finite element method*

and substructure-subdomain technique for dynamic analysis of the coupled fluid-solid interaction problems. Ph. D. Thesis, Tsing Hua University, China.

87. J. T. XING and W. G. PRICE 1999 *Proceeding of the Royal Society* A **455**, 401-436. A power-flow analysis based on continuum dynamics.

88. J. T. XING, W. G. PRICE and Z. H. WANG 2002 *Proceeding of the 5th international conference on vibration engineering, Nanjing, China,* 33-40. A study of power flow characteristics using vector field analysis approach.

89. Y. P. XIONG, J. T. XING, W. G. PRICE and X. P. WANG 2000 *Shock and vibration* **7**, 139-148. Hybrid active and passive control of vibratory power flow in flexible isolation system.

90. Y. P. XIONG, J. T. XING and W. G. PRICE 2001 *Journal of Sound and Vibration* **239**(2), 275-295. Power flow analysis of complex coupled systems by progressive approaches.

91. O. C. ZIENKIEWICZ 1971 *The finite element method.* McGraw Hill.

APPENDIX A: THE ORTHOGONALITY OF PRINCIPAL MODE SHAPES

Let us consider the natural vibration $(\eta = 0)$ of an elastic structure occupying domain Ω with a fixed boundary S_u and a free boundary S_T, where υ represents the unit normal vector pointing outwards, as shown in figure 2.1. The governing equations describing the dynamics of the elastic body are as follows.

Dynamic equation

$$\sigma_{ij,j} = \rho \ddot{u}, \qquad x \in \Omega , \tag{A.1}$$

Constitutive equation

$$\sigma_{ij} = C_{ijkl} e_{kl}, \qquad x \in \Omega , \tag{A.2}$$

Geometric relation

$$e_{kl} = \frac{1}{2}(u_{k,l} + u_{l,k}), \qquad x \in \Omega, \tag{A.3}$$

Boundary conditions

$$\begin{cases} \sigma_{ij}\upsilon_j = 0, & x \in S_T, \\ u_i = 0, & x \in S_u. \end{cases} \tag{A.4}$$

The substitution of equations (A.2) and (A.3) into equations (A.1) and (A.4) gives

$$\begin{cases} C_{ijkl} u_{k,lj} = \rho \ddot{u}_i, & x \in \Omega, \\ C_{ijkl} u_{k,l} \upsilon_j = 0, & x \in S_T, \\ u_i = 0, & x \in S_u. \end{cases} \tag{A.5}$$

The natural vibration of the elastic structure is given by $u_i = U_i e^{i\omega t}$ from which it follows that

$$\begin{cases} C_{ijkl} U_{k,lj} = -\omega^2 U_i \rho, \\ C_{ijkl} U_{k,l} \upsilon_j = 0, \\ U_i = 0. \end{cases} \tag{A.6}$$

It is assumed that $U_i^{(r)}$ and $U_i^{(s)}$ are two arbitrary natural vibration modes with their corresponding natural frequencies ω_r and ω_s ($\omega_r \neq \omega_s$), respectively, satisfying equation (A.6), i.e.,

$$\begin{cases} C_{ijkl}U_{k,lj}^{(r)} = -\omega_r^2 \rho U_i^{(r)}, \\ C_{ijkl}U_{k,l}^{(r)}\nu_j = 0, \\ U_i^{(r)} = 0, \end{cases} \tag{A.7}$$

and

$$\begin{cases} C_{ijkl}U_{k,lj}^{(s)} = -\omega_s^2 \rho U_i^{(s)}, \\ C_{ijkl}U_{k,l}^{(s)}\nu_j = 0, \\ U_i^{(s)} = 0, \end{cases} \tag{A.8}$$

Multiplying equation (A.7) by $U_i^{(s)}$ and integrating over the domain Ω yields

$$\int_\Omega U_i^{(s)} C_{ijkl} U_{k,lj}^{(r)} d\Omega = -\omega_r^2 \int_\Omega \rho U_i^{(r)} U_i^{(s)} d\Omega. \tag{A.9}$$

By using Green theorem and the boundary conditions at (A.7), we obtain the result

$$\begin{aligned} \int_\Omega U_i^{(s)} C_{ijkl} U_{k,lj}^{(r)} d\Omega &= \int_\Omega \{[U_i^{(s)} C_{ijkl} U_{k,l}^{(r)}]_{,j} - U_{i,j}^{(s)} C_{ijkl} U_{k,l}^{(r)}\} d\Omega \\ &= \int_S U_i^{(s)} C_{ijkl} U_{k,l}^{(r)} \nu_j dS - \int_\Omega U_{i,j}^{(s)} C_{ijkl} U_{k,l}^{(r)} d\Omega \\ &= -\int_\Omega U_{i,j}^{(s)} C_{ijkl} U_{k,l}^{(r)} d\Omega, \end{aligned} \tag{A.10}$$

and therefore,

$$\int_\Omega U_{i,j}^{(s)} C_{ijkl} U_{k,l}^{(r)} d\Omega = \omega_r^2 \int_\Omega \rho U_i^{(s)} U_i^{(r)} d\Omega. \tag{A.11}$$

Similarly,

$$\int_\Omega U_{i,j}^{(r)} C_{ijkl} U_{k,l}^{(s)} d\Omega = \omega_s^2 \int_\Omega \rho U_i^{(r)} U_i^{(s)} d\Omega. \tag{A.12}$$

Applications of the relation $C_{ijkl} = C_{klij}$ (see, for example, Reismann & Pawlik 1980) and the summation convention for tensors gives

$$\int_\Omega U_{i,j}^{(s)} C_{ijkl} U_{k,l}^{(r)} d\Omega = \int_\Omega U_{i,j}^{(r)} C_{ijkl} U_{k,l}^{(s)} d\Omega. \tag{A.13}$$

Subtracting equations (A.12) from (A.13) and using the previous result gives

$$\{\omega_r^2 - \omega_s^2\}\int_\Omega \rho U_i^{(r)} U_i^{(s)} d\Omega = 0. \tag{A.14}$$

Because $\omega_r \neq \omega_s$, it thus follows that

$$\int_\Omega \rho U_i^{(r)} U_i^{(s)} d\Omega = 0, \tag{A.15}$$

and

$$\int_\Omega U_{i,j}^{(r)} C_{ijkl} U_{k,l}^{(s)} d\Omega = 0, \tag{A.16}$$

from equation (A.11) or (A.12).

Finally, the orthogonality of the natural modes of the three-dimensional elastic structure can be represented as

$$\int_\Omega \rho U_i^{(r)} U_i^{(s)} d\Omega = \delta_{rs} m_r = \begin{cases} m_r & r = s \\ 0 & r \neq s \end{cases}, \tag{A.17}$$

$$\int_\Omega U_{i,j}^{(r)} C_{ijkl} U_{k,l}^{(s)} d\Omega = \delta_{rs} K_r = \begin{cases} K_r & r = s \\ 0 & r \neq s \end{cases}, \tag{A.18}$$

where δ_{rs} is the *Kronecker* delta. The generalized mass m_r and generalized stiffness K_r take the forms

$$m_r = \int_\Omega \rho U_i^{(r)} U_i^{(r)} d\Omega, \tag{A.19}$$

$$K_r = \int_\Omega U_{i,j}^{(r)} C_{ijkl} U_{k,l}^{(r)} d\Omega = \omega_r^2 m_r. \tag{A.20}$$